# Development of indium-free thin films as contacts for silicon heterojunction solar cells

vorgelegt von
M. Sc. Daniel Meza Arredondo

an der Fakultät IV - Elektrotechnik und Informatik
der Technischen Universität Berlin
zur Erlangung des akademischen Grades

Doktor der Ingenieurwissenschaften
-Dr.-Ing.-

genehmigte Dissertation

Promotionsausschuss:
Vorsitzender: Prof. Dr. Bernd Rech
Gutachter: Prof. Dr. Bernd Stannowski
Gutachter: Prof. Dr. Arno H.M. Smets
Tag der wissenschaftlichen Aussprache: 29. September 2021

Berlin 2022

# Zusammenfassung

Silizium-basierte Solarzellen haben den größten Marktanteil im Bereich der Photovoltaik. Insbesondere Silizium Heteroübergang-Solarzellen (SHJ, engl. silicon heterojunction) wurden aufgrund ihrer potentiell hohen Wirkungsgrade stark weiterentwickelt.

Um die Produktion von SHJ Solarzellen zu verbessern, müssen zahlreiche Faktoren wie Effizienz, Materialkosten oder ökologische Auswirkungen der genutzten Materialien untersucht werden.

Diese Doktorarbeit befasst sich mit der Entwicklung von Indium-freien Kontaktschichten für SHJ Solarzellen. Schichten des transparenten leitfähigen Oxids (TCO, engl. transparent conductive oxide) Aluminium dotiertes Zinkoxid (ZnO:Al) wurden als potentieller Ersatz für Indium-Zinnoxid (ITO) als Vorderseitenkontakt in SHJ Solarzellen in Rückseiten-Emitter-Konfiguration untersucht. Mit der Nutzung von ZnO:Al am Vorderseitenkontakt konnte eine Effizienz der SHJ Solarzelle von 22,6% erreicht werden, welche nur geringfügig unter der, der ITO Referenzzelle von 22,8% lag. Als Hauptgrund für diese etwas niedrigere Effizienz wurde ein höherer Kontaktwiderstand zwischen TCO und dem Silbergitter an der Vorderseite gefunden. Eine Indium-freie Solarzelle, bei der ITO auch auf der Rückseite durch ZnO:Al ersetzt wurde, erreichte eine Effizienz von 22.5%

In einer zweiten Materialstudie wurden per Elekronenstrahl-Verdampfung aufgebrachte Nickeloxid (NiOx) Schichten als mögliche TCO und selektive Kontakte für die photogenerierte Löcher in SHJ Solarzellen untersucht. Nachdem die Funktionsfähigkeit des Prozesses untersucht und bestätigt wurde, wurde der Sauerstoffdruck während der Deposition zwischen $2 \times 10^{-7}$ mbar und $1 \times 10^{-4}$ mbar variiert, um die Materialeigenschaften in einer Bandbreite von metallischem Nickel zu transparentem Nickeloxid zu variieren. Die resultierenden Probe wurden anschließend hauptsächlich mit Röntgenphotoelektronenspektroskopie (XPS, engl. X-ray photolectron spectroscopy) und Energiedispersiver Röntgenspektroskopie (EDX, engl. Energy dispersive X-ray spectroscopy) untersucht.

Als Referenz für zukünftige Experimente wurde eine Materialstudie an den NiOx Schichten durchgeführt. Hierzu wurden UV-VIS Spektroskopie, Röntgendiffraktometrie (XRD, engl. X-ray diffraction) und Hall Mobilitätsmessungen angewandt.

Es stellte sich heraus, dass die Deposition von NiOx auf passivierte Siliziumwafer zu einer starken Reduktion der Minoritätsladungsträgerlebensdauer in der resultierenden Probe führt, weshalb diese nicht für die Anwendung in einer Solarzelle geeignet ist. Um den Grund für die reduzierte Minoritätladungsträgerlebensdauer zu finden, wurde die NiOx Elektronenstrahl Deposition näher untersucht.

Hierbei konnten sowohl ein schädlicher Effekt der während des Prozesses entstehenden Röntgenstrahlung, als auch eine Oxidation der Passivierungsschichten durch die Sauerstoffatmosphäre während der Aufbringung anhand von Photolumineszenz Messungen als Ursachen für die Degradation ausgeschlossen werden.

Weiterhin wurde die Diffusion von Ni-Atomen zur Grenzfläche zwischen amorphem und kristallinem Silizium als Ursache ausgeschlossen. Im abschließenden Teil dieser Arbeit wurden die XPS Spektren von NiO Schichten verschiedener Dicken analysiert. Diese Spektren deuten auf die Präsenz eines Nickelsilizides hin, welches als Rekombinationszentrum für Ladungsträger dienen kann und daher die wahrscheinliche Ursache für die negativen Auswirkungen der Elektronenstrahl Deposition von NiOx auf passivierte Siliziumwafer ist. Einerseits wird das Si von der a-Si Schicht konsumiert um das NiSi zu bilden, wodurch die passivierungseigenschaften vom a-Si verloren gehen und andererseits ist das NiSi ein rekombinationsaktives Material. Ähnliche Ergebnisse wurden in der Literatur gefunden für Nickel Abscheidungen auf a-Si, jedoch nicht in einem reaktiven Prozess unter einer Sauerstoff Atmosphäre.

# Abstract

Silicon solar cells are the technology with the highest market share in the photovoltaic industry. In particular, Silicon Heterojunction (SHJ) solar cells have been strongly developed in the last years due to the high power conversion efficiency that can be achieved with them.

In order to improve the production of SHJ solar cells, many factors such as efficiency, materials cost, ecological impact of the materials extraction should be researched. This thesis contains experimental work related to the development of indium-free materials for the contact layers of SHJ solar cells.

Transparent Conductive Oxide (TCO) layers of Aluminium doped Zinc Oxide (ZnO:Al) were investigated as a potential replacement of Indium Tin Oxide (ITO) for the front contact in SHJ solar cells in the rear emitter configuration. It was found that ZnO:Al can be tuned to yield cell performance almost at the same level as ITO with a power conversion efficiency of 22.6% and 22.8%, for ZnO:Al and ITO, respectively. The main reason for the slight underperformance of ZnO:Al compared to ITO was found to be a higher contact resistivity between this material and the silver grid on the front side. An entirely indium-free SHJ solar cell, replacing the ITO on the rear side by ZnO:Al as well, reached a power conversion efficiency of 22.5%.

Nickel oxide (NiOx) was also investigated as an ITO replacement material. NiOx layers deposited by e-beam evaporation in a reactive process with oxygen were investigated as a possible charge selective contact for holes in SHJ solar cells. As a first step, the viability of depositing NiOx using this process was confirmed. A variation of the oxygen flux during the deposition was performed in order to obtain a variation of the material properties, ranging from metallic nickel layers to transparent nickel oxide layers, when the oxygen deposition pressure varies from $2 \times 10^{-7}$ mbar to $1 \times 10^{-4}$ mbar. These samples were characterized mainly by X-ray Photoelectron Spectroscopy (XPS) and Energy Dispersive X-ray difraction (EDX) measurements.

For future reference and other possible applications of the NiOx, a material study was performed, in which the optical and electronical properties of the layers were characterized. The characterization techniques include ultraviolet and visible (UV-VIS) spectroscopy, X-ray Diffraction (XRD) and Hall mobility measurements.

It was found, that the deposition of NiOx on silicon wafers passivated with a-Si:H leads to a strong decrease in the minority charge carrier lifetime in the samples, making them unsuitable for fabricating photovoltaic devices. The NiOx e-beam deposition on silicon was analyzed in detail in order to find the reason for the decrease in charge carrier lifetime. Although it was not possible to find the root cause for the degradation with certainty, a number of factors could be ruled out as possible causes for the lifetime decrease.

A detrimental effect of X-ray radiation (present in every e-beam process due to the deflection of the electrons) on the wafer, as well as an oxidation of the passivation layers due to the oxygen atmosphere during the deposition, were ruled out using photoluminescence measurements.

Diffusion of nickel atoms through the passivation layers and up to the interface between a-Si and c-Si which would lead to increased recombination at these metal atoms was considered as a possible reason, and also discarded after designing an experiment to measure the diffusion coefficient of nickel atoms in silicon, which showed that no significant diffusion is taking place.

In the final part of this work, the XPS spectra of nickel oxide layers with different thicknesses were compared. One of them is thin enough to allow the measurement of the a-Si/NiOx interface, in which an XPS signal related to nickel silicide was detected. This nickel silicide interlayer is identified as the probable reason for the detrimental effect of the e-beam deposition of nickel oxide on passivated silicon wafers, due to the fact that it acts as a recombination site for the charge carriers, and also that the formation of NiSi consumes a-Si which leads to a thinner passivation layer. Similar results were found in the literature for nickel depositions on a-Si, however not for depositions under an oxygen atmosphere.

A mis padres

# Table of Contents

# List of Figures

# List of Tables

# Abbreviations

**AM1.5G** Air Mass 1.5 Global irradiation.

**BF** Bifacial.

**CCD** Charged Coupled Device.

**EDX** Energy Dispersive X-ray difraction.

**EMIL** Energy Materials In-situ Laboratory.

**EQE** External Quantum Efficiency.

**FF** Fill Factor.

**FTO** Fluorine doped Tin Oxide.

**GDOES** Glow Discharge Optical Emission Spectrometry.

**IOH** Hydrogen doped Indium Oxide.

**IQE** Internal Quantum Efficiency.

**ITO** Indium Tin Oxide.

**MF** Monofacial.

**mpp** maximum power point.

**NIR** near infrared.

**PCE** Power Conversion Efficiency.

**PECVD** Plasma-Enhanced Chemical Vapor Deposition.

**SHJ** Silicon Heterojunction.

**SRH** Shockley-Read-Hall.

**TCO** Transparent Conductive Oxide.

**TLM** Transmission Line Measurements.

**UV** ultraviolet.

**VIS** visible.

**XPS** X-ray Photoelectron Spectroscopy.

**XRD** X-ray Diffraction.

# Symbols

a-Si Amorphous silicon.

a-Si:H Hydrogenated amorphous silicon.

(i)a-Si:H Hydrogenated intrinsic amorphous silicon.

c-Si Crystalline silicon.

$D_{\mathrm{Ni}}$ Diffusion coefficient of nickel.

$\eta$ Power conversion efficiency.

$I$ Current.

$I_0$ Diode saturation current density.

$I_{\mathrm{SC}}^{\mathrm{max}}$ Maximum short circuit current.

$I_{\mathrm{SC}}$ Short circuit current.

$j_{\mathrm{loss}}$ Photocurrent density.

$j_{\mathrm{sc}}$ Short circuit current density.

$\lambda$ Wavelenght.

$\lambda_p$ Plasma frequency.

## Symbols

$\mu$ Hall mobility.

$\mu_n$ Charge carrier mobility.

$n_0$ Charge carrier concentration.

$N_e$ Charge carrier concentration.

NiOx Nickel oxide.

$P$ Output power.

$q$ Electronic charge.

$R$ Resistance.

$R_s^c$ Contact resistance.

$R_{sh}$ Sheet resistance.

$R_s^{TCO}$ TCO resistance.

$\rho_c$ Contact resistivity.

$V$ Voltage.

$V_{OC}$ Open circuit voltage.

ZnO:Al Aluminum doped zinc oxide.

# 1

# Introduction

Energy production and distribution is one of the main challenges that the humanity faces today for the development of the world. Besides this challenge, but maybe even more important we are also facing climate change. It has been calculated, that our actual global carbon emissions have to be reduced in order to reach the global warming goal set by the Paris Agreement [1], which means stopping the warming of our planet at 1.5 °C.

The only way of facing these two challenges in a consequent way, is increasing the amount of renewable energies that we use, trying to locate the energy production sites near the groups of people that need them as well as reducing our energy consumption.

Solar energy is readily available in the regions of the world located between the tropics, and the specific case of photovoltaic power plants can be easy to implement in this regions.

A great amount of research is being done in the area of photovoltaics in order to improve the properties of solar cells. Some of these properties can be, just to name a couple: durability, efficiency, amount of energy invested in their production, production cost, ecological impact of the extraction of raw materials used for their production, recyclability.

Photovoltaic cells are solid-state devices consisting of layers made out of different materials. The different layers of these devices are optimized for performing a task. A simplified diagram of a solar cell is shown in Figure 1.1.

After many years of research photovoltaic devices have been improved, and new layers have been added to the simple structure shown below, a modern solar cell structure, known as the silicon heterojunction (SHJ) solar cell can be seen in Figure 1.2.

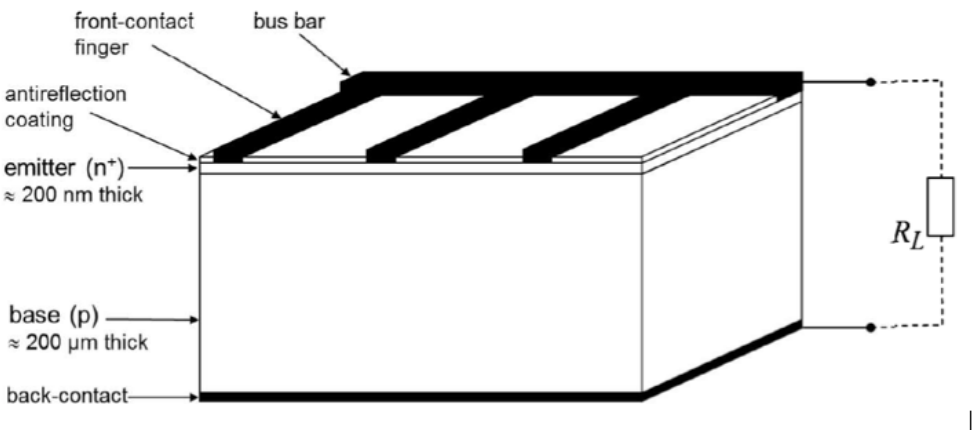


**Figure 1.1:** A simplified diagram of a silicon solar cell, taken from Dittrich [2].

This dissertation focuses in the development of layers consisting of materials known as TCOs which are normally located next to the metal contacts, and can perform mainly two different tasks. Depending on the trade-off between electrical and optical properties of the TCO material its thickness can be adjusted in order to be a charge selective contact and a conductive layer with antireflective properties.

Charge selective contacts are normally achieved through thin layers (5 to 10 nm) that act as a semipermeable membrane for charge carriers, allowing only one type of charge carriers to move through them. This effect is caused by the difference in the position of the conduction band, Fermi level and valence band of the two materials put in contact. The deposition of a semiconductor material onto another leads to a specific line-up of these energies at the interface of the materials in what is known as a semiconductor heterojunction [3].

If a TCO layer with better electronic conduction than that of the absorber is deposited with a thickness between 80 to 100 nm (depending on the refraction index of the TCO and the material below it, in specific n≈2 for a material deposited on silicon) it performs as a charge-carrier conducting material while at the same time forming an antireflective coating, with the downside of a higher optical absorption compared to a thin layer of the same material. On the other side it is possible to deposit a TCO with a smaller thickness so that a modification of the electronic bands at the interfaces of the layered system takes place while maintaining the optical absorption at a minimum.

The most important physical properties of the TCO layers when used as contacts for solar cells are, the amount of light transmitted by them and their electrical conductivity. These physical properties of the layers are not independent of each other, since the physical

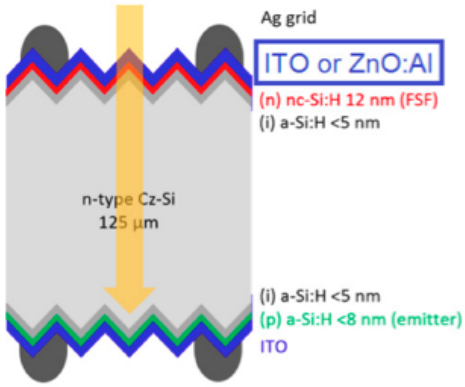


**Figure 1.2:** Cross section of a bifacial SHJ solar cell with the emitter on the rear side, charge selective contacts, texturized surface and a TCO layer that works also as an antireflection coating, taken from Meza et al. [4].

phenomena that improve one of the parameters can affect the other in a negative way. It is for this reason that a trade-off between these properties has to be found.

## 1.1 SHJ solar cells

The history of photovoltaics has developed over the 20$^{\text{th}}$ century parallel to the development of quantum mechanics and solid state physics.

In 1954, Chapin et al. [5] produced the first silicon junction capable of transforming light into electricity at Bell labs. This was the first solar cell ever produced and it had a small power conversion efficiency of only 6%.

Some of the main improvements made to this simple device in order to improve its efficiency are the following:

- Covering the backside of the solar cell with a reflective material, to increase the optical path travelled by light inside of the device, which in turn increases the absorption and the charge carrier density of the device under illumination [6].
- Texturizing the front side of the device, which deviates the direction of the incoming lightbeams, increasing their optical path inside of the device [7].
- Silver grid on the front side of the solar cell, which allows collection of the charge carriers produced by the photovoltaic device with reduced Ohmic losses[8].
- Electrical passivation of the front surface. In a crystal, such as silicon, every atom is electronically bonded to its neighbors, and for this reason the amount of electronically

active recombination sites in form of a hole is very low. This property does not apply for the surface electrons which are missing a neighboring atom in one direction, producing what is known as dangling bonds. The electronical passivation of these dangling bonds, normally achieved through the deposition of a thin hydrogenated amorphous silicon layer, increases the lifetime of the free charge carriers by reducing the surface recombination velocity of the silicon wafer [9], and therefore reducing the probability that a free charge carrier recombines on the surface of the wafer.

- Charge selective contacts on the top and bottom surfaces, which act as a semipermeable membrane for charge carriers and make it possible to collect only one type of charge carriers on one side of the device while blocking the other type of charge carriers of reaching it. These structures reduce the recombination of charge carriers in the region near the contacts of the solar cell [10].

- Transparent Conductive Oxides, which help in the lateral transport of the free charge carriers to the fingers of the silver grid while allowing a great amount of light to be transmitted into the device [11].

One of the most efficient solar-cell concepts known to date is the so called SHJ solar cell, which consists of a silicon wafer electronically passivated on both sides with intrinsic thin layers of hydrogenated amorphous silicon )(i)a-Si:H). On top of these layers, n and p doped layers of amorphous silicon are deposited to form charge selective contacts, as well as the emitter of the photovoltaic device. In order to improve the transport of photogenerated charge carriers in the lateral direction, TCO layers are deposited on top of the amorphous silicon layers. If deposited with the right thickness, the TCO layer can also work as an antireflection coating. A silver grid makes it possible to extract the photogenerated charge carriers while maintaining the series resistance of the system at a minimum. This is normally deposited using screen printing, since it is a process carried out at low temperature, and therefore compatible with the SHJ technology.

When the p-n junction of the device is placed on the side opposed to the incoming light, this is termed a rear emitter silicon heterojunction solar cell. In particular, SHJ solar cells can achieve high power conversion efficiencies, such as, for example 26.7% [12].

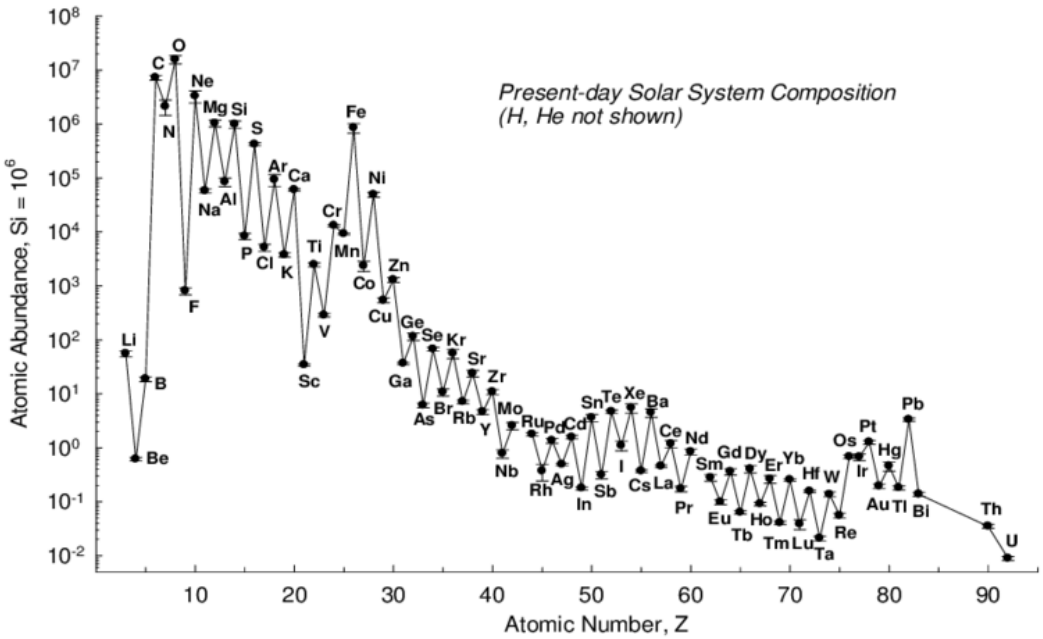


**Figure 1.3:** Availability of the elements of the periodic table in the Earth as a function of atomic number. Availability of Al, Zn and Ni is 5 to 6 orders of magnitude higher than that of In and Sn. Taken from Lodders [13].

## 1.2 Advantages and disadvantages of indium containing contacts

In this dissertation, two materials were analyzed as possible TCOs for replacing the industry standard TCO, namely, tin doped indium oxide also known as ITO. The two materials analysed in this dissertation are ZnO:Al and $NiO_x$.

The material that we are trying to replace, ITO, is a well-known material. It has become the standard material used as a transparent conductive layer in the semiconductor and photovoltaic industry.

The main reason for its wide use in photovoltaics and optoelectronic devices is, that some of its optoelectronic properties, such as optical transmittance, charge carrier mobility, charge carrier concentration and sheet resistance, are better than those of the other known TCO materials. Some other examples of TCO materials include for example, Hydrogen doped Indium Oxide (IOH), Fluorine doped Tin Oxide (FTO) and ZnO:Al.

The specific case of NiOx as a TCO is interesting due to the intrinsic doping type of this material. The materials previously named are n-type doped semiconductors and their doping can be modified in order to engineer optoelectronic devices such as a charge selective contact

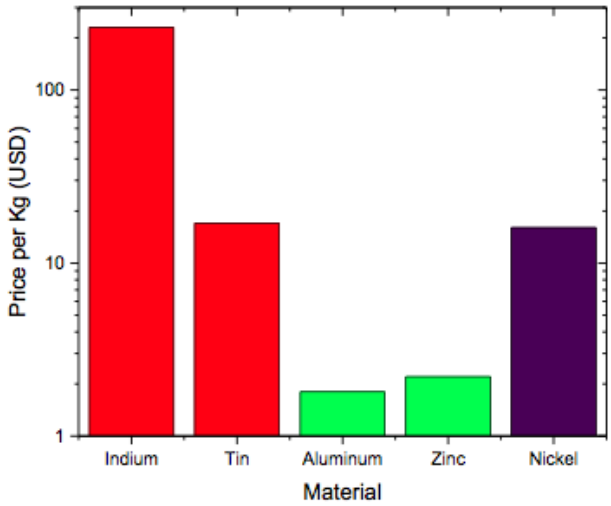


**Figure 1.4:** Comparison in price per Kg of main materials used for producing TCOs: industry standard tin doped indium oxide (red), aluminum doped zinc oxide (green) and nickel oxide (purple). Data taken in June 2020 from [17] and [18].

for electrons on the n side of a p-n junction. NiOx on the other hand is a p-type doped semiconductor [14], which could be used as a charge selective contact for holes on the p side of a solar cell [15]. It has already been implemented by Islam et al. [16] for this purpose in a proof of concept device, where the NiOx was deposited using sputtering.

The main disadvantage of TCO layers that contain the element Indium is, that the availability of this element in the earth is many orders of magnitude smaller than the availability of for example Aluminum or Zinc, as it can be shown in Figure 1.3 taken from Lodders [13].

This fact has the direct consequence, that the price of these metals as raw materials also show a variation of many orders of magnitude. Figure 1.4 shows values for the prices [17, 18] of the raw metals used to prepare the TCO layers that were investigated in these dissertation.

It should be noted, nevertheless, that the price of Indium is somewhat unstable and in the last years it has shown high variations in its price.

## 1.3 Aluminium doped zinc oxide as a TCO

Transparent Conductive Oxides are materials widely used in photovoltaic devices in order to maximize the amount of photons reaching the absorber of the device while minimizing the resistance losses due to electronic transport of the charge carriers from the absorber to the silver grid.

The electronic transport carried out by the TCO layers is done in the lateral direction along the surface of the device. Using a TCO layer represents an advantage in comparison to a pure silicon solar cell due to the difference in resistivity values of these two materials [19].

For example, n-type crystalline silicon, c-Si, has a resistivity of approximately $0.5\,\Omega\,\mathrm{cm}$ for a doping of $10^{16}$ $\mathrm{cm}^{-3}$ donor atoms [20], which is almost the upper limit of doping for an n-type Si wafer before Auger recombination starts to be a factor limiting the lifetime of free charge carriers. On the other hand, common TCOs have resistivities of the order of $10^{-3}$ $\Omega\,\mathrm{cm}$ [19], which is approximately 2 to 3 orders of magnitude lower than that of silicon.

Charge carriers generated in the absorber of a photovoltaic device are required to reach the silver contacts on the top of the solar cell, and the movement of these charge carriers can be decomposed in a vertical movement to the surface of the cell and a lateral movement to the silver finger. Since the thickness of a c-Si substrate is approximately 20 times smaller than the distance between fingers (which is directly related to the proportion between the vertical and the horizontal movement of the charge carriers), it can be easily understood why the use of a TCO layer is advantageous, since it minimizes the resistance losses due to charge carrier transport.

The work presented in this thesis is based on theoretical calculations made by Bivour et al. [21] in which they propose, that placing the emitter of a SHJ solar cell on the rear side, reduces the series resistance for the charge carriers collected on the front electrode. This would, in turn reduce the optoelectronical exigencies of a TCO layer for the front side. In other words, an indium-based TCO could be replaced by other material with worse optoelectronical properties than those of ITO, without leading to a substantial loss in efficiency.

### Anti-reflection property of TCOs

Another reason for the use of TCOs as a front contact on a photovoltaic device is the possibility of forming an anti-reflection coating on the front side of it. If two parameters, namely the thickness and the refraction index of the TCO layer are fine tuned to the properties of the layer below, an optimal optical performance of this layer can be achieved and the overall reflection of the incoming light can be minimized.

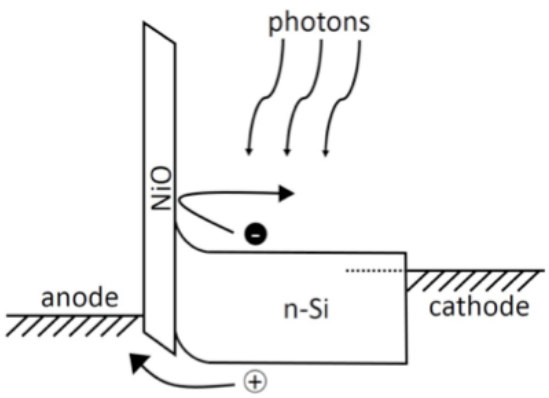


**Figure 1.5:** Energetic band diagram of a charge selective contact formed by depositing nickel oxide on top of a n-doped crystalline silicon wafer. The large bandgap and p-type nature of this material makes it suitable as an electron blocking layer. Taken from Islam et al. [16].

## 1.4 NiOx as a charge selective contact for SHJ solar cells

As stated before, NiOx is an intrinsic p-type semiconductor [14], therefore it could be used as a charge selective contact for holes in a photovoltaic device if deposited on top of n-type crystalline silicon. Figure 1.5 shows conceptually the energetic structure of this heterojunction [16].

NiOx has also been tested for the fabrication of a portable ultraviolet detector [22], as a tunneling layer for dye sensitized solar cells [23], as an electron blocking contact for organic solar cells [15] and together with n-type doped ZnO:Al for the formation of a photovoltaic device [24].

In Chapter 2 of this dissertation the physics fundamentals of solar cells and TCOs are presented, as well as a diffusion model for nickel in silicon which is one of the possible mechanisms for the decrease in charge carrier lifetime discussed in the results chapter.

Chapter 3 presents and explains the used deposition and characterization techniques.

In Chapter 4 the details of the experimental methods are presented in two subsections, separated for the ZnO:Al layers and NiOx layers.

The results and discussion about the ZnO:Al layers as a TCO for SHJ are presented in Chapter 5. The information in this section is based on a published paper by the author [4]. This chapter is divided into the characterization of ZnO:Al layers on glass, solar cell results and TLM measurements of the system ZnO:Al/Ag. The goal of this study was to test experimentally the hypothesis proposed by Bivour et al. [21], that using the rear-emitter

configuration on an SHJ solar cell, places fewer restrictions to the optoelectronical properties of the front TCO.

Chapter 6 contains the experimental results and discussion of NiOx layers as a charge selective contact for SHJ solar cells. The chapter is divided into a material study for thin layers of e-beam evaporated NiOx obtained with a reactive process, a discussion of the problems encountered when depositing this material on wafers passivated with (i)a-Si:H and an investigation about the reason why this problems are found, which is the formation of nickel silicide at the interface between NiOx and a-Si.

In Chapter 7 the conclusions and an outlook of this work are presented.

# 2

# Theory

## 2.1 Photovoltaics basics

Photovoltaics is the branch of physics that studies the conversion of light into electrical energy. Most photovoltaic devices are optimized by using the sun as a light source. The sun is a star placed in the center of our planetary system that radiates electromagnetic energy. The radiation spectrum of the sun can be approximated by the radiation spectrum of a black body at approximately 5800 °C. The black body radiation spectrum expresses the amount of energy with frequency $\nu$ irradiated by a non-reflecting, totally absorbing body at a temperature $T$, which is at thermal equilibrium with its surroundings.

The radiation spectrum of a black body at a temperature $T$ can be derived from Planck's law,

$$B_\nu = \frac{2h\nu^3}{c^2}\frac{1}{\mathrm{e}^{h\nu/kT} - 1} \tag{2.1}$$

and it is clear that the black body radiation spectrum only depends on the temperature of the black body, since $c$, $h$ and $k$ are all constant values (speed of light, Planck's constant and Boltzmann's constant respectively).

Even more, it is important to see, that the radiation spectrum of a black body is a continuous function of the frequency $\nu$, always positive, that tends to zero for very small and very large values of $\nu$. This fact, together with the photoelectric effect explained below, and some basic mathematical knowledge will be enough for gaining some insight about the limits of energy conversion efficiency of photovoltaic cells.

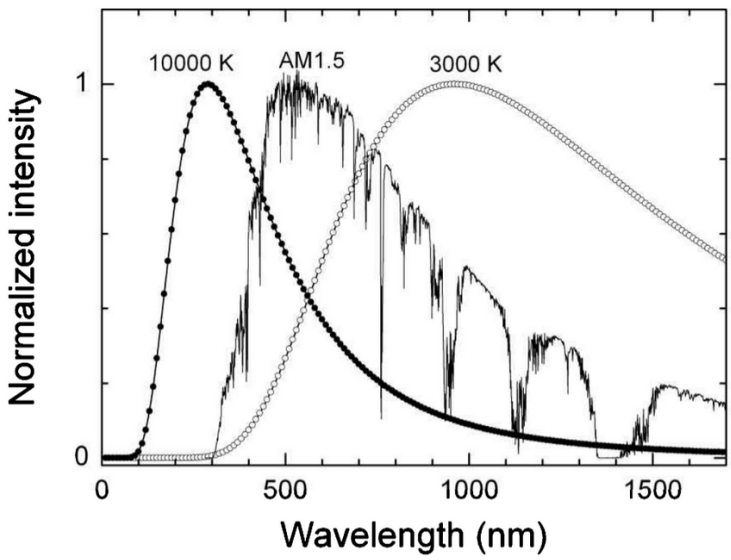


**Figure 2.1:** Normalized blackbody radiation spectra and the Air Mass 1.5 Global irradiation (AM1.5G) solar spectrum. The radiation maximum shifts to shorter wavelengths for higher temperatures. It can be seen that the AM1.5G spectrum can be approximated by a blackbody radiation spectrum. Taken from Dittrich [2].

### Planck's relation

In his paper from 1897, Max Planck stated that light consists of small energy packets called quanta, which have an energy proportional to their frequency.

$$E \propto \nu \tag{2.2}$$

A proportionality constant denoted by $h$ (and later named Planck's constant), allows us to calculate the exact energy value of a photon with frequency $\nu$

$$E = h\nu \tag{2.3}$$

Having this relation between the frequency and the energy of a photon it is possible to transform the units of the vertical axis of the black body radiation spectrum to photon flux measured in photons/second.

### The photoelectric effect

Using Plancks hypothesis, Albert Einstein proposed in 1905 in his paper *"On a Heuristic Viewpoint Concerning the Production and Transformation of Light"*, an explanation of the photoelectric effect. He proposed it is a quantum process, where electrons can be set free

from a metal only by photons with an energy value higher than a certain threshold value called the work function of the material. In semiconductors, which have a different energy band structure than metals, electrons can be excited from the valence band to the conduction band by a photon in a similar process, if the photon possess enough energy. The smallest energy such a photon should have is the difference between the upper edge of the valence band and the lower edge of the conduction band. This energy difference is known as the bandgap of a semiconductor material. The bandgap is an inherent characteristic of a semiconductor material.

## 2.2 Photogenerated current

It should be clear from the previous Section, that semiconductor materials with different bandgaps show different behaviours when placed under sun irradiation. The electrons of a semiconductor material with a small bandgap have a higher probability of being excited to the conduction band since the amount of photons per unit time reaching it with energy equal or greater than the bandgap is bigger than that of a material with a large bandgap.

The amount of photons per second arriving at the semiconductor with an energy equal or greater than the bandgap is then a continuous and decreasing function of the bandgap. Assuming that every photon entering a photovoltaic device with an energy equal or greater than the bandgap would set an electron free, and that all these electrons can be collected and extracted, a new quantity can be defined: the maximum short circuit current density, $I_{\mathrm{SC}}^{\mathrm{max}}$, of a photovoltaic device (see Figure 2.2).

In every photovoltaic device it is important to maximize the amount of photons reaching the part of the device in which the photogeneration of electrons takes place which is called absorber. For this reason, any layer of a different material placed between the absorber and the sun should have larger electronic bandgap than the absorber so it absorbs as few photons as possible, in order to achieve a high power conversion efficiency. As it has been mentioned before, some layers that are used on the front side of photovoltaic devices are, for example, passivation layers and TCOs.

## 2.3 Characteristics of a solar cell

The following section is based on Chapter 1, of Dittrich's book on "Materials concepts for solar cells" (2014).

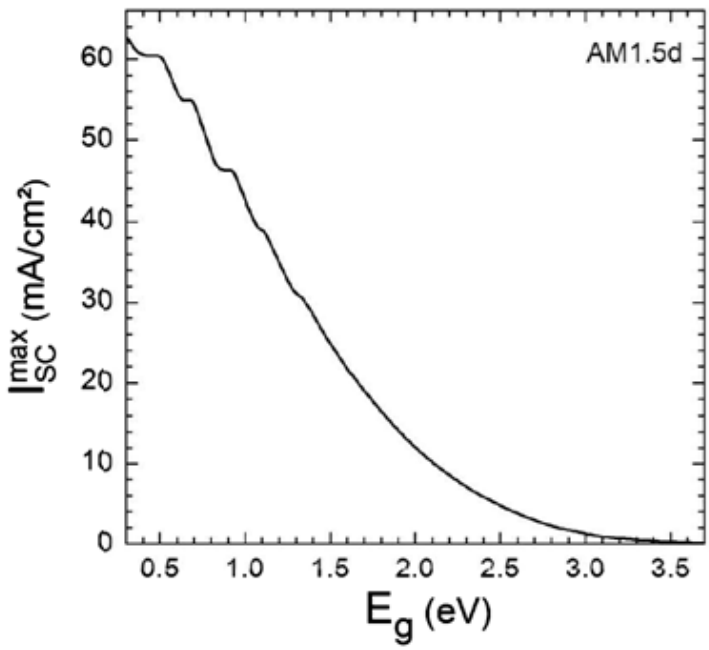


**Figure 2.2:** Maximum short circuit current density, $I_{\mathrm{SC}}^{\mathrm{max}}$, of a semiconductor material as a function of its bandgap, $E_{\mathrm{g}}$. Taken from Dittrich [2].

The energy output of a solar cell under constant illumination consists of a photovoltage and a photogenerated current. If the contacts of such a solar cell would be connected to a load resistance, a working point of the solar cell would be determined. If the value of this resistance would be varied from zero (short circuit condition) to a very high value (so big, that the system can be studied as an open circuit) all the possible working points of a solar cell would be obtained. The set of working points is called the IV-curve of a solar cell.

It is clear, that the amount of current passing through the load resistance would decrease from the maximum photogenerated current, called short circuit current ($I_{\mathrm{SC}}$), to zero in a continuous decreasing function. The voltage, $V$, across the resistance, $R$, would increase with the current, $I$, according to Ohm's law, $V = R * I$, from zero to a maximum value, called open circuit voltage, $V_{\mathrm{OC}}$, in a continuous increasing function.

Since each value of the load resistance connected to a solar cell defines a working point of the solar cell composed by a current and a voltage, another relation can be formulated as follows: the output power, $P$, of such a photovoltaic device under illumination is defined as $P = V * I$, where $V$ and $I$ are the voltage across the load resistance and the current passing through it respectively, an output power can be assigned to each value of the load resistance.

Besides that we know, that the product of two continuous functions is also a continuous function, and in this case also the product of $I$ and $V$ is zero for both an infinitely big resistance as well as for an infinitely small resistance, fulfilling the conditions of Rolle's Theorem, which

states that at least one of the points of the function is either a maximum or a minimum. In our case, since both $I$ and $V$ are positive values, there should be at least a point which is a maximum of the function, since all the working points can be found on the positive half of the IV 2-dimensional space.

That point is called the maximum power point (mpp) and it is useful for characterizing the photovoltaic device with the Power Conversion Efficiency (PCE), defined as:

$$\mathrm{PCE} = \frac{\text{power output in the mpp}}{\text{power input}} \tag{2.4}$$

The Fill Factor ($FF$) gives us information about the quality of the solar cell can be also established as the ratio between the power obtained by multiplying $I_{\mathrm{SC}}$ and $V_{\mathrm{OC}}$ and the output power in the mpp:

$$FF = \frac{P(\mathrm{mpp})}{I_{\mathrm{SC}} \cdot V_{\mathrm{OC}}} \tag{2.5}$$

If a monochromatic light with wavelength $\lambda$ strikes on a photovoltaic device, the External Quantum Efficiency (EQE) can be defined as the ratio between the current produced by the photovoltaic device and the number of incident photons:

$$\mathrm{EQE}(\lambda) = \frac{N_{\mathrm{e}}(\lambda)}{N_{\mathrm{ph}}(\lambda)} \tag{2.6}$$

If the internal performance of a photovoltaic device wants to be analyzed, the amount of reflected photons can be taken into account, and the Internal Quantum Efficiency (IQE) can also be defined as the ratio between the EQE and the of non-reflected fraction of incident photons

$$\mathrm{IQE}(\lambda) = \frac{\mathrm{EQE}(\lambda)}{1 - R(\lambda)} \tag{2.7}$$

where $R$ is the fraction of incident light with a wavelength $\lambda$ reflected by the device front surface.

A typical EQE (Figure 2.3) spectrum gives information about physical processes happening inside a solar cell. It can be seen for example that EQE is low for wavelengths larger than 1200 nm and shorter than 200 nm, which represent photons with energy lower than the bandgap and high energetic photons which could be transmitted by the solar cell. Besides that there is a central region in which the losses can be accounted as mainly reflection losses , and both an

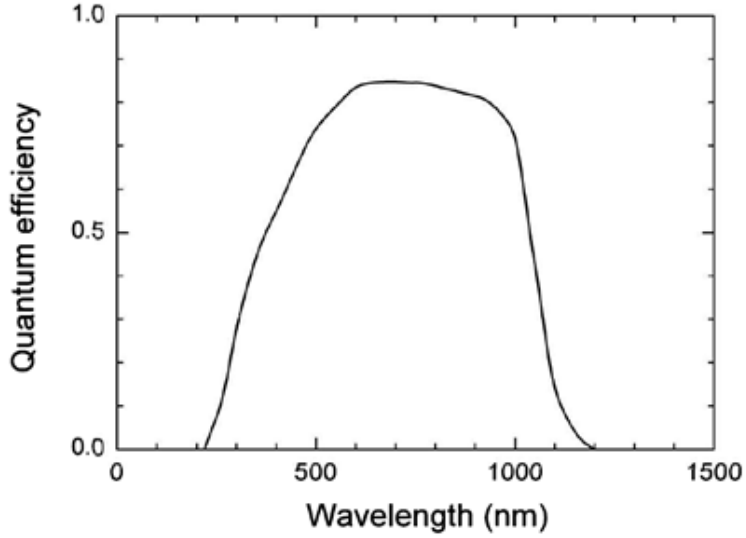


**Figure 2.3:** Typical EQE spectrum of a solar cell. Losses due to reflection recombination and transmission can be identified from this kind of measurement (see details in text) Taken from Dittrich [2].

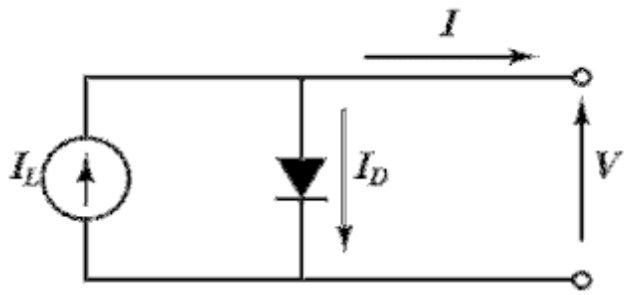


**Figure 2.4:** Equivalent circuit of a solar cell.

ascending and a descending slope on the sides of the curve, this gradual change in the EQE is due mainly to recombination of blue photons on the front surface and red photons on the rear surface.

## 2.4 Diode equation

An ideal photovoltaic device can be represented by an equivalent circuit composed by a diode and a photocurrent generator, as shown in Figure 2.4. These two elements are a representation of the main physical phenomena taking place inside of a solar cell. The photocurrent generator is a source of electric current when it is placed under illumination and the diode acts as a charge separator. For this reason, the performance of a solar cell can be described with the diode equation:

$$I_D = I_0 \cdot \left[\exp\left(\frac{q\,U}{k_B\,T}\right) - 1\right] \tag{2.8}$$

where $I_0$ is the diode saturation current density, $q$ the electronic charge, $k_B$ the Boltzmann constant and $T$ the temperature of the system. $I_0$ is a characteristic of a solar cell which depends in the type of material used and the geometry of the absorber, and can be estimated if the $V_{\mathrm{OC}}$ of a solar cell is measured as a function of $I_{\mathrm{SC}}$, while varying $I_{\mathrm{SC}}$ over many orders of magnitude and . For increasing positive values of the voltage applied to a diode (forward bias), the current through it increases exponentially. If negative voltages are placed across the diode (reverse bias), the current across the diode is very small and of the order of magnitude of the diode saturation current density. If no potential difference is placed across the diode, no electronic transport should take place, therefore a 1 is substracted from the exponential term, resulting in

$$I_D(0) = 0\,\mathrm{A} \tag{2.9}$$

Under illumination, and with a load resistance connected to the photovoltaic device, the photocurrent generated by the photocurrent generator flows through the load resistance reducing the current across the diode in a quantity equal to the photogenerated current $I_{\mathrm{ph}}$, resulting in the following equation for the IV-characteristics of a solar cell under illumination

$$I = I_0 \cdot \left[\exp\left(\frac{q\,U}{k_B\,T}\right) - 1\right] - I_{\mathrm{ph}} \tag{2.10}$$

From Eq. 2.10, the $V_{\mathrm{OC}}$ of a solar cell can be calculated by setting $I_{\mathrm{ph}} = I_{\mathrm{SC}}$ and $I_D = 0$, obtaining:

$$V_{\mathrm{OC}} = \frac{k_B\,T}{q} \cdot \ln\left(\frac{I\mathrm{sc}}{I_0} + 1\right) \tag{2.11}$$

As it can be seen, the $V_{\mathrm{OC}}$ of a solar cell increases with $I_{\mathrm{SC}}$, and the value $I_0$ limits the achievable value of $V_{\mathrm{OC}}$. Minimizing $I_0$ is important for achieving high power conversion efficiencies.

For a real solar cell the effect of internal series resistance of the device and internal shunt resistance has to be taken into account. Examples of internal series resistance are, for example, the resistance of the materials used for building the different components of a solar cell as well as the contact resistance between them, and an example for shunt resistance could be a region on the edges of a solar cell in which charge carriers can flow back to the region in which they were before they were charge separation took place. The equivalent circuit of a

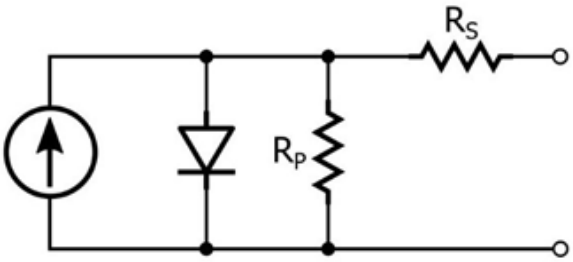


**Figure 2.5:** Equivalent circuit of a solar cell with series and shunt resistance.

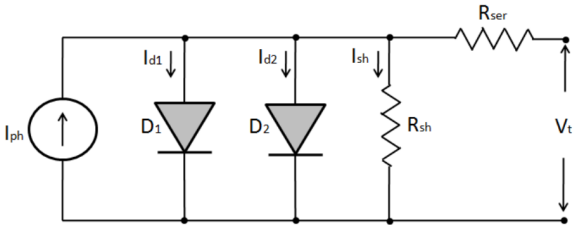


**Figure 2.6:** Equivalent circuit of a solar cell with two diodes

solar cell including series and parallel resistance is shown in Figure 2.5. The diode equation that represents this equivalent circuit is:

$$I = I_0 \left[ \exp\left( \frac{q(U - I \cdot R_s)}{k_B T} \right) - 1 \right] + \frac{U - I \cdot R_s}{R_p} - I_{\mathrm{SC}} \tag{2.12}$$

### The two-diode model of a pn junction under illumination

The recombination of photogenerated charge carriers takes place in two regions inside a solar cell. A fraction of the photogenerated charge carriers recombines in the n-type and p-type neutral regions, while the other fraction recombines in the defect states in the pn-junction. If both recombination processes are taken into account, the equivalent circuit of a solar cell has to be modified to include two diodes connected in parallel which have different ideality factors.

The equation that describes the behaviour of this system is:

$$\begin{aligned} I = {} & I_0 \left[ \exp\left( \frac{q(U - I \cdot R_s)}{k_B T} \right) - 1 \right] \\ & + I_{0,SRH} \left[ \exp\left( \frac{q(U - I \cdot R_s)}{2 k_B T} \right) - 1 \right] \\ & + \frac{U - I \cdot R_s}{R_p} - I_{\mathrm{SC}} \end{aligned} \tag{2.13}$$

## 2.5 Charge carrier recombination

Charge carrier recombination is a physical process in which a free electron and a free hole annihilate each other and release the energy they possessed to the system in some way. Since recombination is conceptually the reverse process of photogeneration, it limits the amount of free charge carriers present in a semiconductor material and therefore the efficiency of a photovoltaic device constructed with such material.

There are four main processes by which an electron and hole can recombine, radiative recombination, Auger recombination, Shockley-Read-Hall (SRH) recombination and surface recombination. Radiative and Auger recombination are processes related to the intrinsic properties of the semiconductor and for this reason can't be avoided or reduced. SRH and surface recombination are related to the amount of defects in the bandgap or on the surface of a semiconductor respectively. For this reason they can be minimized if the photovoltaic devices are manufactured in the right way, reducing the impurities of the materials and reducing the amount of defects in them.

Radiative recombination consists on the annihilation of a free electron and a free hole by emitting a photon [25]. Radiative recombination can not be avoided in semiconductors and is proportional to the densities of free electrons and holes. The characterization technique called photoluminescence, which consists of injecting electrons to a solar cell and observing if light comes out of it, shows if radiative recombination is taking place in such a solar cell.

Auger recombination is the annihilation of a free electron and a free hole by transferring the energy to a third free charge carrier and exciting it deeper into the conduction or valence band if the third carrier is an electron or a hole respectively [26]. This recombination process can not be avoided in semiconductors and is proportional to the product of the square of the density of free electrons and the density of free holes, or the square of the density of free holes and the density of free electrons.

SRH recombination takes place when an energy state inside of the electronic bandgap acts as a trap state for charge carriers. Trap states can be caused for example, by impurities inside the semiconductor. In this process, a free charge carrier gets stucked in the trap state, and after some time, another charge carrier with opposite sign annihilates the first one by falling into the same trap state. There is a possibility, that a charge carrier trapped in a defect state is set free again either by a photon or thanks to a thermal excitation. The probability of this happening is related to the energetic distance between the trap state and the conduction band.

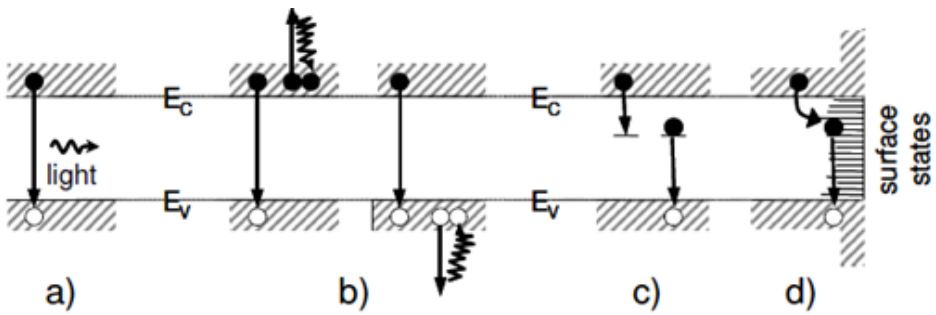


**Figure 2.7:** Schematic representation of the recombination types, a)radiative recombination, b)Auger recombination, c)Schockley-Read-Hall recombination and d)surface recombination. Taken from Tous [27].

For this reason the trap defect states can be classified in shallow (near the conduction band) and deep trap states (near to the middle of the forbidden bandgap).

Surface recombination is the annihilation of an electron and a hole by means of reaching the surface of a semiconductor and falling into an energetic surface trap state. Surfaces of crystalline semiconductors are normally regions with a large density of electronic states inside the bandgap of the material due to the abrupt change in the continuity of the crystal structure. The density of electronic states in the surface of a semiconductor is in the same order of magnitude than the amount of atoms on it. Differently to the trap states which cause SRH recombination, surface trap states have a broad energetic distribution due to large distribution of physical properties of the free bonds (such as angle and length). Figure 2.7 shows an schematic representation of the different recombination processes.

## 2.6 Charge carrier lifetime

Due to the phenomenon of recombination, the charge carrier density inside a semiconductor under illumination reaches equilibrium when the photogeneration rate and the recombination rate are equal. It is also true that the charge carrier density inside of a semiconductor decreases over time, after a semiconductor stops being illuminated. The recombination rate is the reciprocal of the free charge carrier lifetime.

Each recombination type is a different physical phenomenon and for this reason the total lifetime of free charge carriers depends on which of the recombination mechanisms acts on them, for example, Auger recombination is a process that requires three particles to happen. For this reason, at high injection levels the Auger recombination lifetime is shorter than at low injection levels since the probability of three particles interacting is higher, for a higher charge carrier density.

If the recombination lifetimes are denoted by $\tau_{rad}$, $\tau_{Auger}$, $\tau_{SRH}$ and $\tau_{surface}$, then the total lifetime of free charge carriers in a semiconductor is

$$\frac{1}{\tau_{total}} = \frac{1}{\tau_{rad}} + \frac{1}{\tau_{Auger}} + \frac{1}{\tau_{SRH}} + \frac{1}{\tau_{surface}} \tag{2.14}$$

From this equation it follows that the lowest lifetime will limit the overall charge carrier lifetime of the material. Radiative recombination lifetime and Auger recombination lifetime have a dependency on the doping of the wafer, since the doping determines the concentration of free charge carriers, and this two processes require the physical proximity and interaction of two and three charge carriers respectively.

The doping of the wafers is a quantity that wants to be maximized, since the $V_{\mathrm{OC}}$ of a solar cell will be limited by the diffusion potential of a pn junction which in turn is limited by the energetic difference between the fermi levels of the p-type and the n-type regions of the pn junction.

Since the SRH and surface recombination types do not depend on doping, but on the amount of defects on the bulk and surface of the wafer respectively as well as on the on the capture cross section of the defects and the thermal velocity of the charge carriers, the amount of doping of the wafers can be adjusted up to a level in which the Auger and radiative recombination lifetimes are of the same order of magnitude than the SRH and surface recombination lifetimes.

Figure 2.8 shows an overview of the recombination lifetimes as a function of doping for GaAs and silicon, it can be seen that the doping of silicon wafers is limited by auger recombination, since the dependance of the lifetime on the doping is stronger for this recombination process than for radiative recombination. The opposite is true for GaAs

## 2.7 Transparent Conductive Oxides and Drude Model

### 2.7.1 Transparent Conductive Oxides

Transparent conductive materials are very useful for the extraction of charge carriers from a photovoltaic device, and specifically for the lateral transport once these charge carriers reached the surface of the device. High optical transmittance derived from a large bandgap is a requirement if high power conversion efficiencies want to be achieved. The electrical conductivity of TCOs is nevertheless a function of many parameters such as the charge carrier concentration and the mobility of the charge carriers.

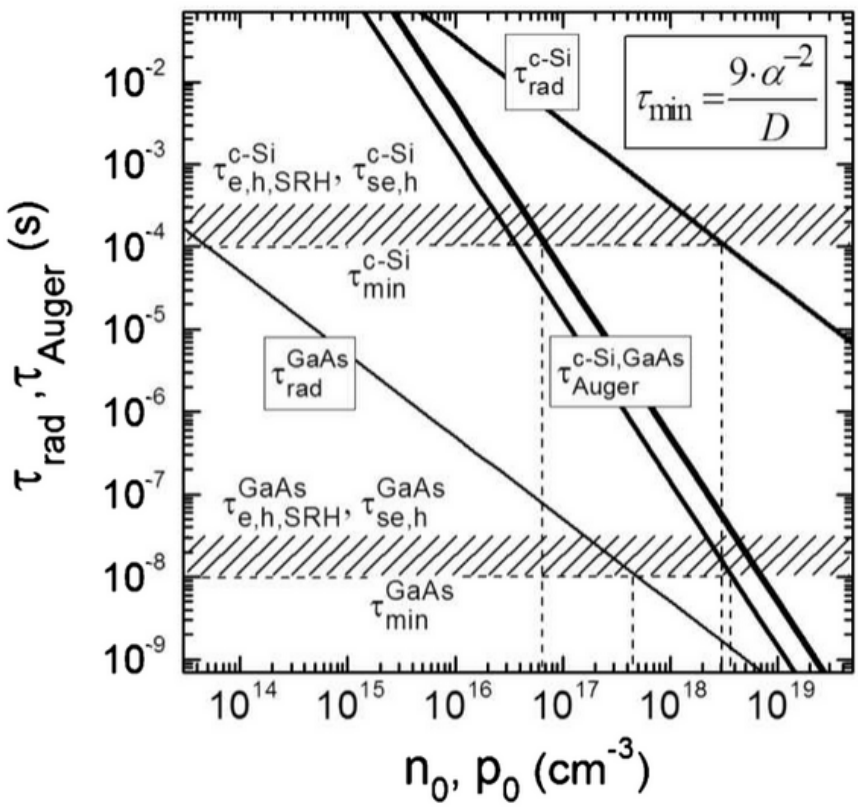


**Figure 2.8:** Auger and radiative recombination lifetimes as a function of wafer doping for silicon and GaAs. SRH and surface recombination lifetimes appear as a horizontal band due to the fact that they don't depend on doping but on the defect concentration. Taken from Dittrich [2].

In general, the resistivity of an electronic conducting material is given by:

$$P = \frac{1}{q\, n_0\, \mu_n} \tag{2.15}$$

where $q$ is the elementary charge, $n_0$ the charge carrier concentration and $\mu_n$ the charge carrier mobility of the material.

In order to calculate the resistance of a TCO layer, the geometry of the layer has to be taken into account. The resistance of a geometric conducting body is inversely proportional to the width and height of it and proportional to its length.

$$R_{\text{sh}} = \frac{1}{q\, n_0\, \mu_n} \left( \frac{L}{W \cdot H} \right) \tag{2.16}$$

Where $W$ and $H$ are width and height respectively, and $L$ the length of the conducting body.

Since TCOs are normally deposited as thin films on top of solar cells, another quantity, called sheet resistance is used to characterize them. The sheet resistance of a TCO is defined

as:

$$R_{\mathrm{sh}} = \frac{1}{q\, n_0\, \mu_n} \left(\frac{1}{d}\right) \tag{2.17}$$

where $d$ is the thickness of the TCO layer.

Now, if the conductivity of these type of materials is to be increased, either the concentration of charge carriers, the mobility or the thickness of the layer has to be increased. Each of these parameters can be adjusted in order to find an optimum value for the conductivity of the TCO layer, as discussed next.

### Charge carrier concentration

The electrical conductivity of transparent metal oxides can be increased by means of increasing the amount of free charge carriers in the material. This can be achieved by intrinsic or extrinsic doping, the first one can be achieved, for example, by changes in the stoichiometry of the layer as shown by Kim et al. [28]. Extrinsic doping can be achieved by the replacement of a host metal atom of the metal oxide lattice by an atom with a different amount of valence electrons, i.e. in a different oxidation state. An example of this would be the introduction of aluminum atoms into the zinc oxide lattice. Each aluminium atom contributes with an extra charge carrier in the conduction band of zinc oxide.

The extra charge carriers in the conduction band of the TCO layer are considered free charge carriers and therefore can absorb a photon with any energy. This process, called free carrier absorption is different to the absorption process in which at the beginning, the charge carrier is in the valence band, and has to absorb a photon with energy equal or greater than the bandgap in order to be excited into the conduction band of the semiconductor material (see Figure 2.9).

Due to free carrier absorption, the amount of light transmitted by the TCO layer decreases with increasing charge carrier concentration. It can be said that a trade-off between transmittance and conductivity exists for the charge carrier concentration of a TCO layer.

### Charge carrier mobility

The term charge carrier mobility refers to the velocity of the charge carriers in a material when they are under the influence of an electric field. In a polycrystalline material, as many sputtered thin films are, the charge carrier mobility increases if the average grain size increases,

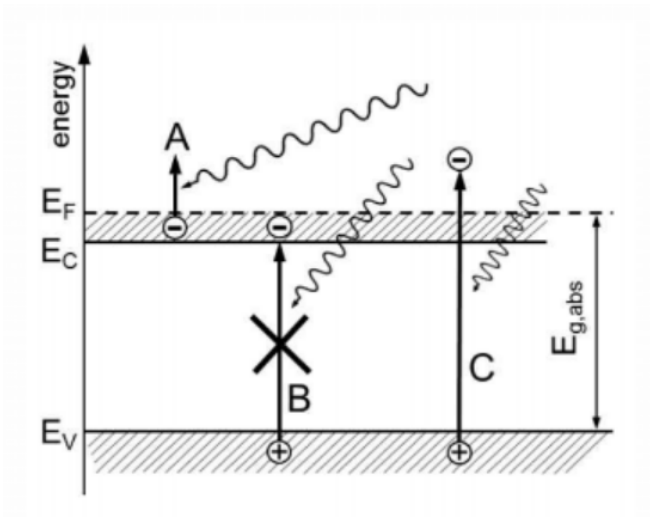


**Figure 2.9:** Diagram of absorption processes, **A** free carrier absorption, **B** a forbidden process, the excitation of a charge carrier to occupied states in the conduction band of a semiconductor and **C** fundamental absorption. For a degenretaed semiconductor some energetic levels inside the bandgap so the real bandgap $E_{g,abs}$ is larger than that of the non-degenerated semiconductor.

since the grain boundaries of neighbouring grains can represent an electrostatic potential barrier for the free charge carriers.

The charge carrier mobility of a highly doped semiconductor material is also a function of the amount of ionized impurities in it. For a highly doped material under illumination, a great number of impurities is ionized and each of them acts as a scattering point, which obstructs the way of the free charge carriers.

#### Thickness

The thickness of a TCO layer also plays a role in its optoelectronical properties. Depending on the refraction index of the material of which the TCO layer is made and the refraction index of the material placed below, an antireflection coating can be made that minimizes the reflection coefficient of the system by tuning the thickness of the TCO layer. On the other side, TCO layers containing a large free charge carrier density, absorb an amount of light proportional to their thickness, due to the fact, that this electrons can absorb a photon with any energy.

### 2.7.2 Reflection losses and anti-reflection coatings

This section follows from Chapter 2 in Dittrich [2].

The reflection coefficient of a material, which is a function of the wavelength, is defined as the ratio between the reflected photons and the incoming photons with a certain wavelength.

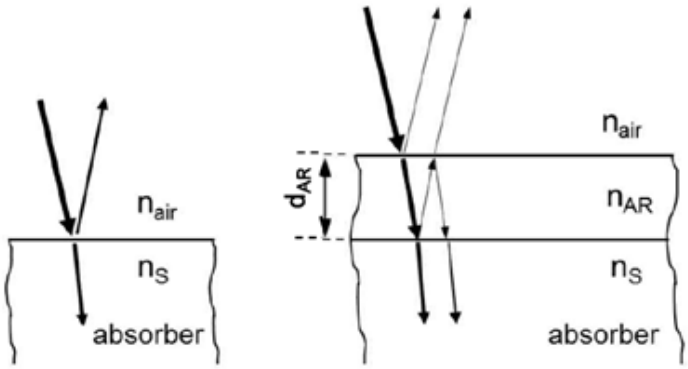


**Figure 2.10:** Reflection from air incoming into a material and antireflection coating placed on that material.

It can be calculated if the refractive indices of the material, $n_s$ and the ambience (in the case of solar cells, air has a refractive index of 1) are known.

For normal incidence of the incoming light, the reflection coefficient is:

$$R(\lambda) = \left(\frac{n_{\text{air}} - n_s(\lambda)}{n_{\text{air}} + n_s(\lambda)}\right)^2 \tag{2.18}$$

An antireflection coating is a layer of a material with a certain refractive index and thickness, that, when placed over another material, reduces the amount of reflected light incoming with a certain wavelength to zero due to destructive interference(see Figure 2.10). If the refractive index of the material is $n_{\text{AR}}$ and the thickness $d_{\text{AR}}$, the reflection is suppressed for a wavelength

$$\lambda = 4\, n_{\text{AR}}\, d_{\text{AR}} \tag{2.19}$$

Using the last condition for destructive interference, a reflection minimum can be calculated

$$R_{\text{min}} = \left(\frac{n_{\text{AR}}^2 - n_{\text{air}} n_s}{n_{\text{AR}}^2 + n_{\text{air}} n_s}\right)^2 \tag{2.20}$$

which can be reduced to zero if $n_{AR} = (n_{\text{air}}\, n_s)^{1/2}$.

Highly doped TCOs, with a charge carrier concentration higher than $10^{19}$ cm$^{-3}$, are said to be degenerated semiconductors since some of the charge carriers occupy energy levels in the conduction band. This kind of materials can be described with the Drude model of electrical conduction.

### 2.7.3 Drude Model

The Drude Model [29] is a semi-classical model for the movement of electrons in a conducting solid that can be used very successfully for calculating macroscopic properties of the solid, even though the assumptions taken to develop the model are very simple.

The Drude Model states that a solid conducting body, for example a metal, consists of a regular array of atoms forming a lattice and each atom donates a certain amount of electrons that can move freely into the lattice. This electrons are known as the valence electrons of the metal and they form what is sometimes called a "sea" of electrons, leaving behind ionized atoms in a regular array.

In the absence of an electric field the movement of these electrons is random and therefore the net current flowing through the conductor is 0. Under an electric field (for example if a voltage is applied to the sides of the conductor), the free electrons start to move and accelerate in a direction opposed to the direction of the electric field.

The assumptions made by Drude in his model are:

1. The electrons have a probability of scattering against one of the ionized atoms higher than 0, so collisions between a free electron and an ionized atom occur.

2. After a collision with one of the ionized atoms, the momentum of the electron is 0, and the kinetic energy that the electron possessed until that moment is transferred to the lattice in form of thermal energy.

The time between collisions for an electron is different every time depending on which path is followed by it after the collision, but an average time between scattering events can be calculated. The average time between collisions is represented by $\tau$.

The final velocity that an electron has immediately before a collision event can be different for each collision, depending on how much time the electron was allowed to accelerate under the electric field, nevertheless an average velocity can be calculated, this velocity is called drift velocity and represented by $v_d$.

From this model more information can be extracted, for example, if we consider that the electrons in the metal are subject to an acceleration proportional to the electric field and to their electric charge (Coulombs Force) but inversely proportional to their mass, $a = qE/m$, then we can write:

$$v_d = \frac{qE}{m}\,\tau \tag{2.21}$$

which represents a relation between the drift velocity, $v_d$, and the average time between colisions $\tau$.

If we substitute this result into the microscopic current: $I = n\ q\ v_d\ A$, where $A$ is the cross section area of the conductor, $q$ the elementary electric charge and n the charge carrier concentration, we have:

$$I = n\ \frac{q^2 E}{m}\ \tau\ A \tag{2.22}$$

Dividing by the cross section area on both sides of the equation we have the current density on the left side, and on the right side the electric field multiplied by a factor that only depends on constants and intrinsic properties of the material analysed:

$$J = \frac{n\, q^2\, \tau}{m} E \tag{2.23}$$

The current density moving through a solid conductor is proportional to the electric field applied to it, which is basically Ohm's law, and the proportionality factor is the macroscopic quantity known as conductivity.

So the Drude model gives us a microscopic expression for the conductivity of a material, by using just a couple of very simple assumptions.

## 2.8 Optical properties of TCO layers

As it has been seen in Section 2.7, TCO layers can absorb and reflect light due to different physical phenomena happening inside them. A measurement of the optical properties using for example UV-VIS spectrometry can give us information about this processes.

Figure 2.11 can be analysed in 3 regions, for short wavelengths, it can be seen that the absorption of the film is high and decreases rapidly to a low value, while the transmission does the opposite, this is due to the fact, that photons inciding with this wavelength have enough energy to excite a charge carrier from the valence into the conduction band. This is therefore the region in which fundamental absorption can be seen. The edge of this region is a good estimate of the optical bandgap of the semiconductor material.

At around 500 nm, a region can be seen in which the absorption of the film is very low, this region is called the optical window of the TCO layer. Photons in this region have a smaller energy than the bandgap of the semiconductor, and are therefore mainly transmitted.

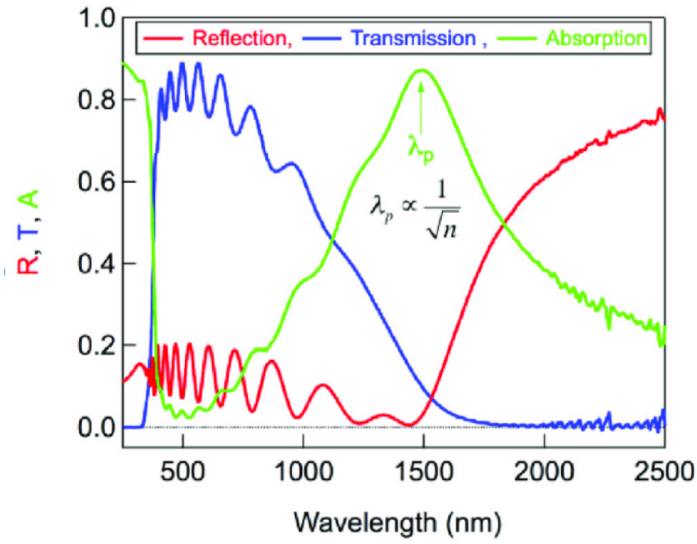


**Figure 2.11:** Reflection transmission absorption spectra of an ZnO:Al film. The absorption of this film starts at a value close to 1 and decreases rapidly showing the range in which fundamental absorption is taking place, for longer wavelengths increases again due to free carrier absorption. (See details in text) Taken from Alberi and Gregoire [30].

At around 750 nm and up to 1500 nm an increase in the absorption of the film can be seen. This phenomenon happens due to the absorption of a photon by an electron which is already inside the conduction band, and it is called the free carrier absorption region. A point in the absorption curve can be seen at around 1500 nm, called plasma frequency, $\lambda_p$. The free charge carrier absorption is a process which gets promoted by groups of charge carriers oscillating called plasmons. The plasma frequency is the frequency for which free carrier absorption is maximum.

For degenerated semiconductors, an increase in the bandgap as a function of charge carrier concentration, known as the Burstein-Moss shift can be observed due to the fact that energy states inside of the bandgap are occupied and fundamental absorption can not take place from a state in the valence band to an occupied state in the conduction band (Figure 2.12).

## 2.9 Formation of a semiconductor heterojunction

A semiconductor heterojunction is understood as the interface between two semiconductor materials with different electronic bandgaps. There are mainly three types of semiconductor heterojunctions, namely straddling gap, staggered gap and broken gap shown in Figure 2.13.

According to the Anderson model for the formation of heterojunctions [31] when different materials are put in contact, a modification of the energy bands takes place in a small spatial region around the interface. This modification, if correctly engineered and designed in a

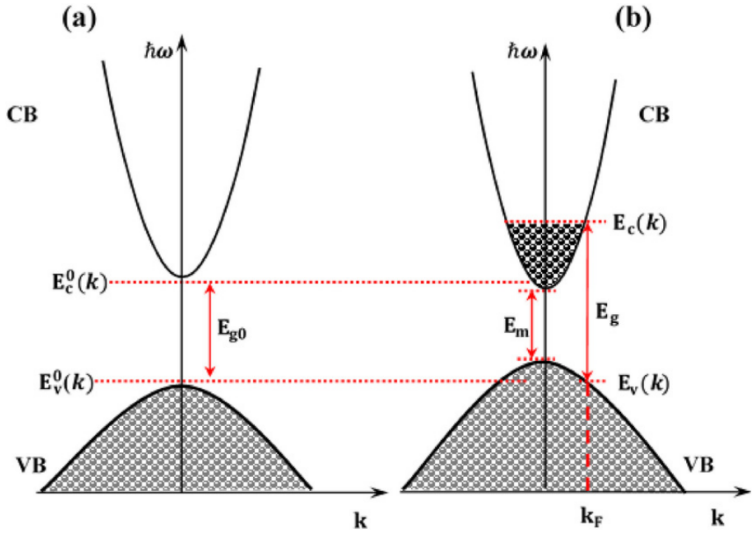


**Figure 2.12:** Representation of the Burstein Moss shift for a non-degenerated (a) and a degenerated (b) semiconductor. In case (a) the bandgap of the material is equal to the distance between the valence and conduction band edges. In case (b) the effective bandgap is increased due to the presence of charge carriers in energy levels inside the conduction band

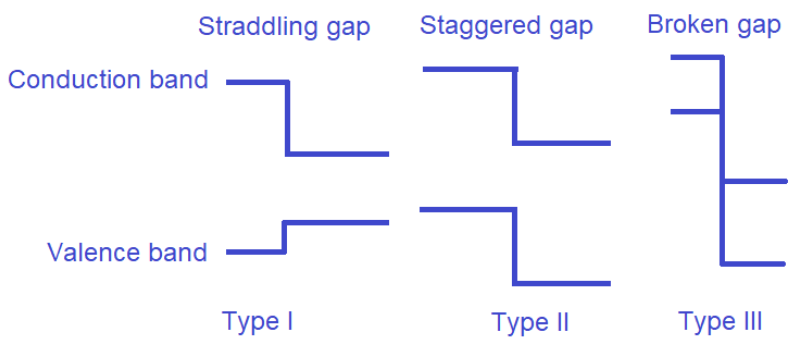


**Figure 2.13:** The three possible heterojunction types are shown for different combinations of conduction and valence band position. Type I or straddling gap, type II or staggered gap and type III or broken gap

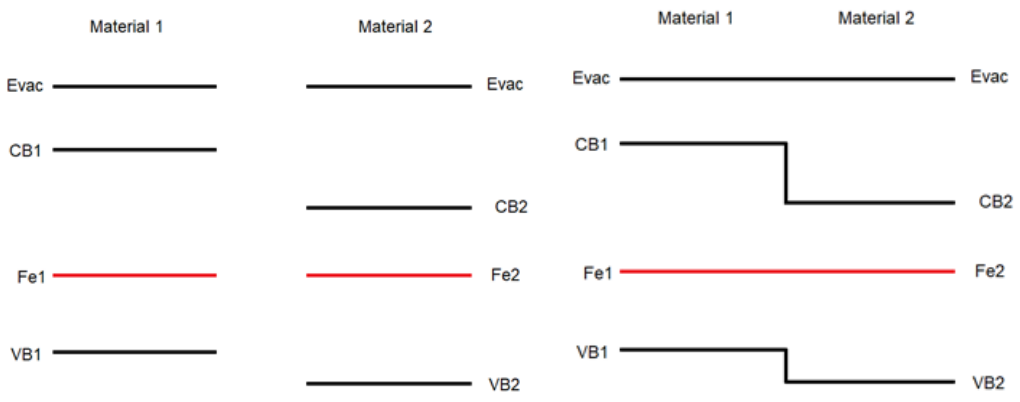


**Figure 2.14:** (*Left*) Energetic band diagrams of two semiconductor materials before setting them in contact for forming a semiconductor heterojunction. (*Right*) Simple semiconductor heterojunction showing the formation of an electronic structure that blocks electrons from moving from material 2 into material 1, and holes from moving from material 1 into material 2.

specific way can produce different electronic structures which can be useful for the production of better photovoltaic devices, such as the ones shown in the next section.

## 2.10 Charge selective contacts

One of the possible electronic structures that can be achieved by means of forming a heterojunction is a structure known as a charge selective contact, which is one of the main topics of this thesis and the main reason for the high efficiency reached by the SHJ silicon solar cells.

In the more general case, in order to form a charge selective contact, two semiconductors with different bandgaps are put in contact, and following the Anderson model the band offsets between the conduction band and the valence band of both materials can be determined [31]. When these materials are set in contact, in order to reach an equilibrium of the Fermi energy in the whole system, their electronic bands will bend up or downwards in a certain way that depends on the relative position of the Fermi levels of these material .

It is possible, nevertheless, to analyze an oversimplified case of a heterojunction and still get to understand the working principle of a charge selective contact. This simple case would be represented by a system in which both materials have their Fermi level at the same energetic level, which would not produce a bending of the energetic bands. If one assumes, that one of the materials (for example material 1) has both its conduction and valence band nearer to the vacuum level than those of the other material (material 2), the energetic levels, before setting the materials in contact would look like those in Figure 2.14 *left*.

After setting the materials in contact, since the Fermi energies are at the same level and no band bending occurs, the electronic structure of the heterojunction would look like that shown in Figure 2.14 *right*. It is evident, that if an electron-hole pair is produced inside of material 1, the hole can only move inside of the material 1, because in order to move into material 2 it would have to overcome a potential barrier, while the electron is able to move inside of material 1 but also to move into material 2 since no potential barrier confines it only to material 1. A similar reasoning can be made for an electron-hole pair produced inside material 2, in order to find out that material one works as a semi-permeable membrane for only one type of charge carriers, in this case, holes.

In a more general case, the Fermi levels of the two materials are not at the same level before they are set in contact, and a band bending occurs. In order to visualize the band bending of the heterojunction it is important to take into account, that the Fermi level of both materials should be at the same level through the whole system. For this reason, the electronic bands of one of the materials have to be shifted in such a way that the Fermi levels are at the same energy.

First, the energy band offsets can be calculated using the Anderson model if the ionization potentials ($I_1$ and $I_2$) and electron affinities ($\chi_1$ and $\chi_2$) of the semiconductors are known. The ionization potential is defined as the energetic difference between the vacuum energy and the upper edge of the valence band, and the electron affinity is the energetic difference between lower edge of the conduction band and the vacuum energy level.

With this data, the offset of the conduction $\Delta E_C$ and offset of the valence band $\Delta E_V$ of the heterojunction 2.13 can be calculated as

$$\Delta E_C = -(\chi_2 - \chi_1)$$
$$\Delta E_V = (E_{g2} - E_{g1}) - \Delta E_C$$

After calculating the offsets, the Fermi levels are set in equilibrium and the conduction and valence band of one material are connected to the conduction and valence band of the other material taking into account the offsets at the contact point between materials.

Figure 2.15 shows three examples of heterojunctions that can be formed by joining two semiconductors with different doping in each example [32]. In each of the cases the relative position of the Fermi level of these materials makes it possible to form different structures that can be useful for the production of a photovoltaic device. A difference in doping in the

semiconductor materials leads to a different kind of band bending. In case b, this heterojunction allows electrons to move from the p-type material to the n-type, while blocking the holes. In case c, electrons are blocked to move from the n-type material to the p-type material while holes would be able to move in that direction if they tunnel through the potential barrier. Note that the band offsets for all three heterojunctions are the same independently of the doping of the materials, because the two semiconductors used are the same for the three examples.

## 2.11 SHJ Solar cells

For the production of a silicon heterojunction solar cell a material with a bandgap larger than silicon is placed on one of the surfaces of the wafer immediately before the metallic contact. The material used in this case can be for example, silicon dioxide [33], with a very large bandgap of 9.3 eV [34] or amorphous silicon, a-Si, with a bandgap of approx. 1.7 eV [35, 36], the main difference between these two materials being, that the a-Si layers can be deposited at low temperatures of approx. 200 °C, while $SiO_2$ is produced by thermal oxidation of c-Si at around 1000 °C.

In the case of amorphous silicon, this material performs two tasks in the photovoltaic device. Due to the higher bandgap of this material, it can be used for forming charge selective contacts on both sides of the device, and, if during the deposition of this material hydrogen atoms are present in the reacting gas during deposition, for example, by using silane gas $SiH_4$ as a precursor, the dangling bonds found on the surface of the c-Si can be passivated. The passivation of the dangling bonds reduces the surface recombination velocity of the charge carriers [37], leading to a potentially more efficient device. Other materials used for surface passivation of c-Si wafers are for example, $SiN_x$:H [38], $Al_2O_3$ [39, 40].

By using TCOs on the top of these solar cells specifically tuned to achieve both a high lateral conductivity of the charge carriers and antireflection properties for the incoming light, it has been possible to achieve high power conversion efficiencies with this kind of devices.

The electronic band structure of an SHJ solar cell can be seen in Figure 2.16. The electronic band offset of the heterojunction for the conduction and valence bands between the n-type c-Si and the a-Si:H(i) can be appreciated. The band structure leading to charge selective contacts of electrons and holes can be seen on the left and right sides of the diagram respectively. The energetic barrier that a free electron needs to overcome in order to move from the n-cSi through the intrinsic and p-type a-Si:H is very large in comparison to the energy barrier that

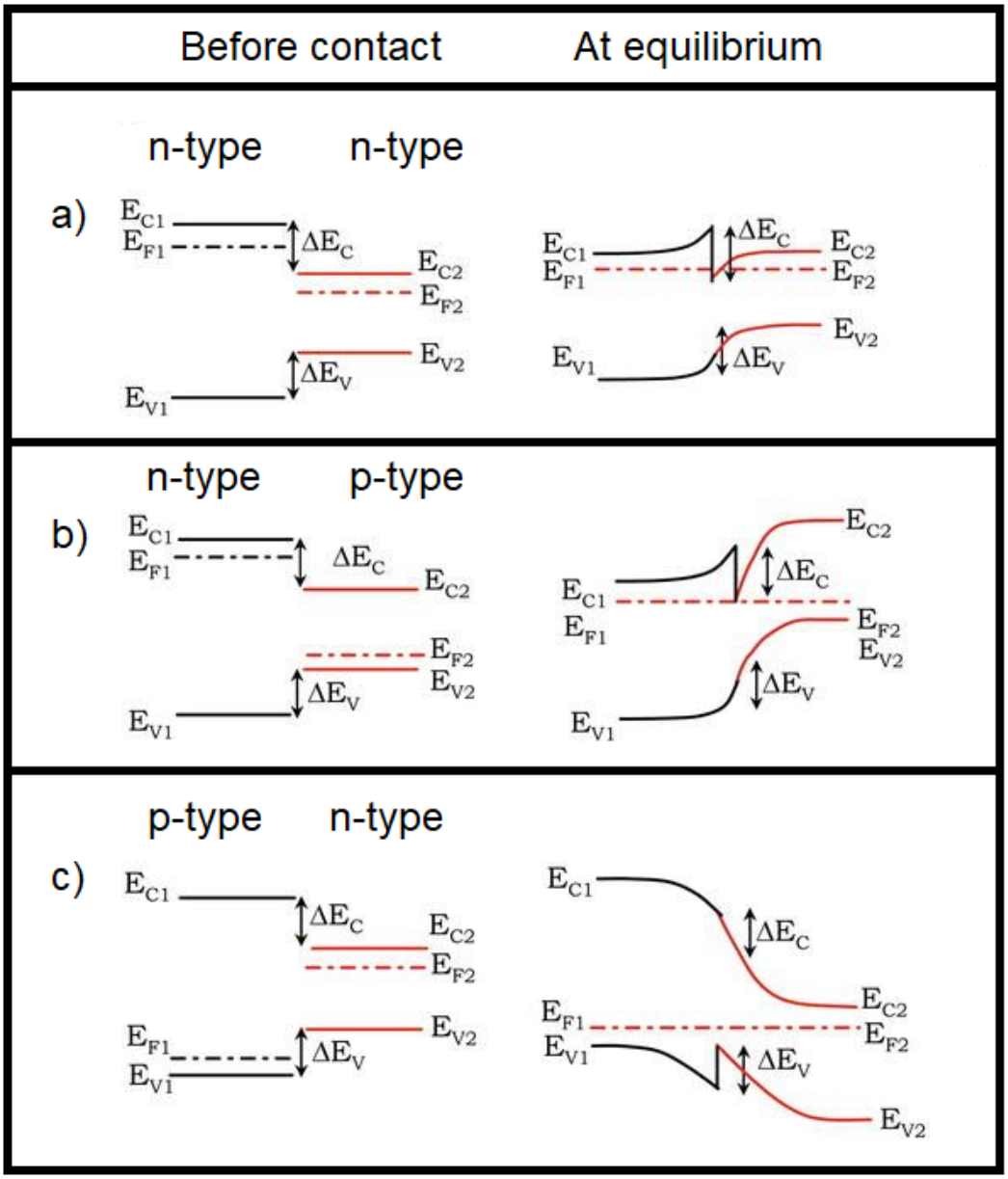


**Figure 2.15:** Different heterojunction structures formed by setting in contact two semiconductors with different doping types. The structures shown in a) and b) show charge selective contacts for electrons and the one shown in c) a charge selective contact for holes. Based on an image from Chakrapani [32].

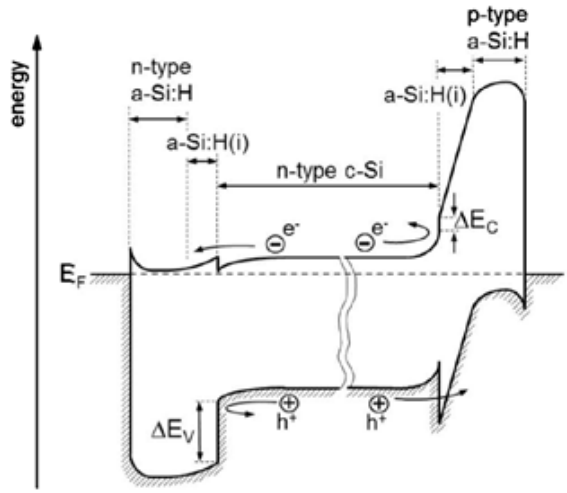


**Figure 2.16:** Band diagram of a silicon heterojunction with intrinsic thin layer solar cell. The effect of the intrinsic layer as a charge selective contact, due to its large bandgap in comparison to that of the c-Si, on both the top and the bottom of the device can be seen. Taken from Dittrich [2].

it has to overcome in order to move through the intrinsic and n-type a-Si:H. The energetic barrier that a free hole needs to overcome in order to move from the n-cSi to through the intrinsic and n-type a-Si:H is very large in comparison to the energy barrier that it has to overcome in order to move through the intrinsic and p-type a-Si:H.

A good overview of the characteristics of SHJ solar cells can be found in De Wolf et al. [41].

## 2.12 Nickel Oxide: An overview

Nickel oxide is a semiconductor material with a wide bandgap (approx. 3.8 eV) and an intrinsically p-type behavior [14]. The p-type doping of nickel oxide is regulated by Ni vacancies and oxygen interstitials [42]. NiOx crystallizes in the rock salt structure and it has been prepared by many methods such as sol-gel [43], spray pyrolysis [44], sputtering [16] and aerosol assisted chemical vapor deposition [45], among others.

In Jlassi et al. [44], nickel oxide thin films were deposited using spray pyrolysis from a hydrated nickel chloride solution onto glass substrates. Their optical and electrical characteristics were measured and it was found, that the optical bandgap decreases from 3.7 eV to 3.55 eV due to the formation of non-stoichiometric films with an excess of oxygen. The electrical resistivity of the films was in the range of 10 to 200 $\Omega$ cm.

Islam et al. [16] made a proof-of-concept device using nickel oxide as an electron blocking layer in a silicon solar cell. They propose using the stoichiometry of nickel oxide as the optimization parameter in NiOx silicon contacts due to tha fact that the p-type behavior of

nickel oxide is defined by its stoichiometry. The p-doping nature of nickel oxide The NiOx was deposited using magnetron sputtering from a NiOx target, i.e. in a non-reactive process.

The p-type doping nature of nickel oxide is produced mainly by the intrinsic point defect nickel vacancy, which, as it has been shown by Karsthof et al. [46] can be introduced into nickel oxide films by using high oxygen partial pressures during growth.

Visible-light transparent solar cells were prepared by Kawade et al. [24] by forming a heterostructure composed of NiO and Zn. They could show that a small photovoltaic effect can be seen.

Predanocy et al. [47] prepared nickel oxide thin films by means of DC reactive magnetron sputtering on which they investigated the effect off annealing at 500 °C. They concluded that the crystallite size increases with annealing, and that the transparency of the films increases. Their films have an optical bandgap of 3.7 eV, resistivities between $3 \times 10^{-4}\ \Omega\,\mathrm{cm}$ and $8 \times 10^{-4}\ \Omega\,\mathrm{cm}$, and a carrier density of approximately $10^{-13}\ \mathrm{cm}^{-3}$. Reddy et al. [48] found an optical bandgap of 3.8 eV and a transmittance of 60% at a wavelength of 650nm using DC reactive magnetron sputtering for the production of thin films.

Menchini et al. [49] produced a device based on a crystalline silicon wafer with an emitter fabricated using RF sputtering in a reactive process. Due to the low conductivities of the films, they were used only as electron blocking layers. A transparency of 63.9% at a wavelength of 550 nm is reported as well as a sheet resistance of $120\,\mathrm{k}\Omega/\mathrm{sq}$ which corresponds to $0.24\,\Omega\,\mathrm{cm}$ for a film with 20 nm thickness. The devices produced present an s-shaped IV curve, probably due to a high concentration of defects at the interface between nickel oxide and silicon.

Another method used for the synthesis of nickel oxide thin films is sol-gel spin coating as it can be found in a characterization study by Raut et al. [43]. It has been found that their optical bandgap changes from 3.86 eV to 3.47 eV when the films are annealed at 700 °C.

Nickel oxide films prepared by ebeam evaporation from a sintered nickel oxide target have been used for electrochromic devices [50].

In the field of organic solar cells, a 5 nm thin film of nickel oxide was used as an effective electron blocking layer [15]. The film was produced using sputtering from a nickel oxide target. A solar cell which uses nickel oxide as an electron blocking layer shows a slightly better performance, and a slower degradation process than a cell that uses PEDOT:PSS.

Nickel oxide nanoparticles were used in combination with P3HT as a hole transport material for a $Sb_2S_3$ solar cell showing a substantial improvement of the power conversion efficiency compared to solar cells using pristine P3HT [51].

In Helmholtz Zentrum Berlin, nickel oxide has been investigated for different projects in the field of perovskite solar cells. A monolithic tandem cell composed of perovskite and $Cu(In,Ga)Se_2$ reached a stabilized PCE of 21.6%, by using a bilayer of PTAA and NiOx as a hole transport layer [52].

Di Girolamo et al. [53] improved the nickel oxide layer with a thin NaCl layer, which increases the work function of NiOx by 0.3 eV, making it possible to achieve 18% PCE and an increased $V_{OC}$ due to the suppression of surface recombination. In a later work [54], they showed that the hysteresis behaviour of a perovskite solar cell can be drastically reduced if a hybrid magnesium organic interlayer is used between the nickel oxide hole transport layer and the perovskite in comparison to the same system using a PMMA interlayer.

A nickel oxide layer used as a hole selective layer was also implemented in a perovskite device in which the difference between flat and wrinkled morphology was studied. It was found that for a flat morphology layer a higher charge carrier recombination at the NiOx/perovskite interface takes place, which leads to a decrease in Voc for the flat samples in comparison to the wrinkled ones. A PCE of 17% was achieved for the best cell. [55]

## 2.13 Nickel silicide as a contact for solar cells

Nickel silicide has been studied as a material for metallization of solar cells, specifically as a replacement for the more expensive silver metallization.

In Chaudhari and Solanki [56], nickel was deposited on c-Si solar cells and annealed at temperatures of 400 to 430 °C in order to form nickel silicide, which lowers the contact resistivity between nickel and silicon. the nickel silicide layer is further covered with copper to reduce metal grid line resistance. A reduction of 50% in the series resistance of these cells compared to commercial silver screen printing is achieved.

In Tous et al. [57] a contact consisting of Ni/Cu/Ag layers is used to fabricate a p-type CZ-Si PERC cell with 19.5% PCE. Tous et al. [58] analysed the bilayer system Ni/Cu as a replacement for silver, but in a process in which the annealing of the sample to form NiSi is avoided. Since the annealing of nickel can damage the industrially produced shallow emitter, large area excimer laser annealing is used. This process makes it possible to form a NiSi layer without inflicting greater damage to the wafer or to the anti-reflection coating.

Many other studies have shown that NiSi is a good contact material for solar cells [59, 60, 61, 62, 63]. Marshall et al. [64] is of particular interest to the present dissertation due to the

similar approach as that shown in Section 6.7. In Marshall et al. [64] a NiSi/PolySi/$SiO_2$/c-Si system is investigated as a passivated contact for silicon solar cells. It was found, that if an amorphous silicon layer is integrated between the NiSi and the PolySi layers, the passivation is improved and the recombination decreased.

Olowolafe et al. [65] studied the formation of nickel silicides, depositing nickel thin films on different silicon substrates (crystalline, polycrystalline and amorphous), and found that a reaction between nickel and amorphous silicon takes place even at a low temperature (200° C) forming nickel silicide.

## 2.14 Diffusion of nickel atoms in silicon

One of the possible reasons considered in this thesis for the free charge carrier lifetime decrease of the passivated silicon wafers after a nickel oxide deposition is the diffusion of nickel atoms through in the amorphous and crystalline silicon.

If this phenomenon does take place, the nickel atoms diffusing through the a-Si should at some point reach the a-Si/c-Si interface. It is known that this interface passivates the dangling bonds of the crystalline silicon wafer. The main task of the passivation layer is to increase the lifetime of the charge carriers by lowering the probability of a free charge carrier to recombine with an electronic active dangling bond and therefore decrease the surface recombination at the a-Si/c-Si interface.

### 2.14.1 Calculations of nickel diffusion in silicon

The diffusion of one material in another can happen in different ways. It has been shown that nickel diffuses in a crystalline silicon matrix mostly interstitially [66], and that, in amorphous silicon, the diffusion of nickel happens through trap retarded interstitial migration, produced by intrinsic traps in the amorphous phase with a binding enthalpy of 0.8 eV [67].

The physical quantities that define how a material diffuses into another are the temperature of the system, the time of diffusion, and the ease with which the atoms of one material can move between the atoms of the hosting material. This latter physical quantity is known as the diffusion coefficient $D$, and is measured in $cm^2/s$.

The phenomenon of diffusion also depends on the amount of diffusing material available at $t = 0$. If the amount of diffusing material is large enough that the concentration at the interface does not change during diffusion, it can be considered an inexhaustible source. In this

case, and for a constant $D$ the diffusion profile, as a function of the distance to the interface, has the form of the error function. If the amount of diffusing material is small, so that the movement of atoms inside of the host material changes the concentration of the layer at the interface, the process is known as diffusion from an exhaustible source. The diffusion profile of an exhaustible source for fixed $D$ has the shape of an exponential decay.

Since in a diffusion process the diffusing particles move from the spatial region where their concentration is higher to that where the concentration is lower, it can be said that the amount of atoms diffused to a depth $x$ inside of the host material is an increasing function of the temperature of the system and the diffusion time, and a decreasing function of the distance $x$.

The equation obtained from Fick's diffusion model [68] for an exhaustible source is:

$$N(x,t) = N_s(t) \exp\left(\frac{-x^2}{4D_{\mathrm{Ni}}\, t}\right) \tag{2.24}$$

Where $x$ is the distance into the host matrix measured from the interface, $D_{\mathrm{Ni}}$, the diffusion coefficient of nickel in silicon and t the time since the diffusion process starts. $N_s(t)$ represents the concentration of nickel atoms at the interface between nickel and amorphous silicon, and is a decreasing function of time, since, if nickel atoms diffuse into silicon, and no new atoms are added to the original layer, the concentration at the interface has to decrease in order for the law of conservation of matter to hold true.

$N_s$ as a function of time is expressed by the following relationship:

$$N_s(t) = \frac{Q}{\sqrt{\pi D_{\mathrm{Ni}} t}} \tag{2.25}$$

Where $Q$ is the surface density of nickel at the interface between nickel and amorphous silicon, measured in $\mathrm{cm}^{-2}$. This value can be calculated if the molar volume of a material is known. For nickel and other metals it is approximately $10^{22}$ to $10^{23}$ atoms per $\mathrm{cm}^3$, which means that a nickel layer places approximately $10^{15}$ atoms on an interface with area equal to 1 $\mathrm{cm}^2$.

The mechanism that drives interstitial diffusion is activated by the thermal vibrations of the materials in contact. If the temperature of the system is high enough, and the thermal vibrations reach a certain threshold value, one of the materials starts to diffuse into the other (or both of them diffuse into the other which is known as interdiffusion). Since temperature has a direct effect on the velocity with which the diffusing atoms move inside the host matrix,

the diffusion coefficient is also a function of the temperature. For nickel diffusing in crystalline silicon, the long accepted diffusion coefficient [69] is:

$$D_{\mathrm{Ni-cSi}}(T) = 2.3 \times 10^{-3} \exp\left(\frac{-0.47\ \mathrm{eV}}{k_B T}\right) \mathrm{cm}^2/\mathrm{s} \tag{2.26}$$

Some more recent investigations by Lindroos et al. [66] have concluded that an even higher coefficient could be more accurate. The value found by this investigations is:

$$D_{\mathrm{Ni-cSi}}(T) = 1.69 \times 10^{-4} \exp\left(\frac{-0.15\ \mathrm{eV}}{k_B T}\right) \mathrm{cm}^2/\mathrm{s} \tag{2.27}$$

According to Kuznetsov and Svensson [67] in a study using amorphous silicon layers, the diffusion coefficient of nickel in this material is many orders of magnitude smaller, being:

$$D_{\mathrm{Ni-aSi}}(T) = 3 \times 10^{-3} \exp\left(\frac{-1.3\ \mathrm{eV}}{k_B T}\right) \mathrm{cm}^2/\mathrm{s} \tag{2.28}$$

A calculation of these three diffusion coefficients as a function of the temperature is shown in Figure 2.17. It can be observed that the diffusion coefficient of nickel in silicon proposed by Bakhadyrkhanov et al. [69] increases from $10^{-11}$ to $10^{-7}$ $\mathrm{cm}^2/\mathrm{s}$ when the temperature increases from 0 to 350 °C. The coefficient proposed by Lindroos et al. [66] is several orders of magnitude higher and the diffusion coefficient of nickel in amorphous silicon 7 to 15 orders of magnitude lower for the same range.

From this calculation it can be seen, that the diffusion of Ni in a-Si happens at a very slow rate compared to diffusion in c-Si. For our investigations we need to analyse the probability of nickel atoms reaching the a-Si/c-Si interface, after assuming, that the thin a-Si layer (5 nm) could be damaged by the e-beam NiOx deposition.

In the case that nickel atoms reach the a-Si/c-Si interface, a calculation shows, that even at room temperature the diffusion of nickel atoms in c-Si happens at a fast pace, reaching high concentrations at large depths into the silicon matrix in a short time. This would be detrimental to the electronic properties of the silicon wafer as it has been shown by Yoon et al. [70] and Savin et al. [71].

Using the lower diffusion coefficient for Ni in c-Si from [69], the nickel surface concentration $N_s$ as a function of time for a 1 nm thick layer at room temperature can be calculated and is shown in Figure 2.18.

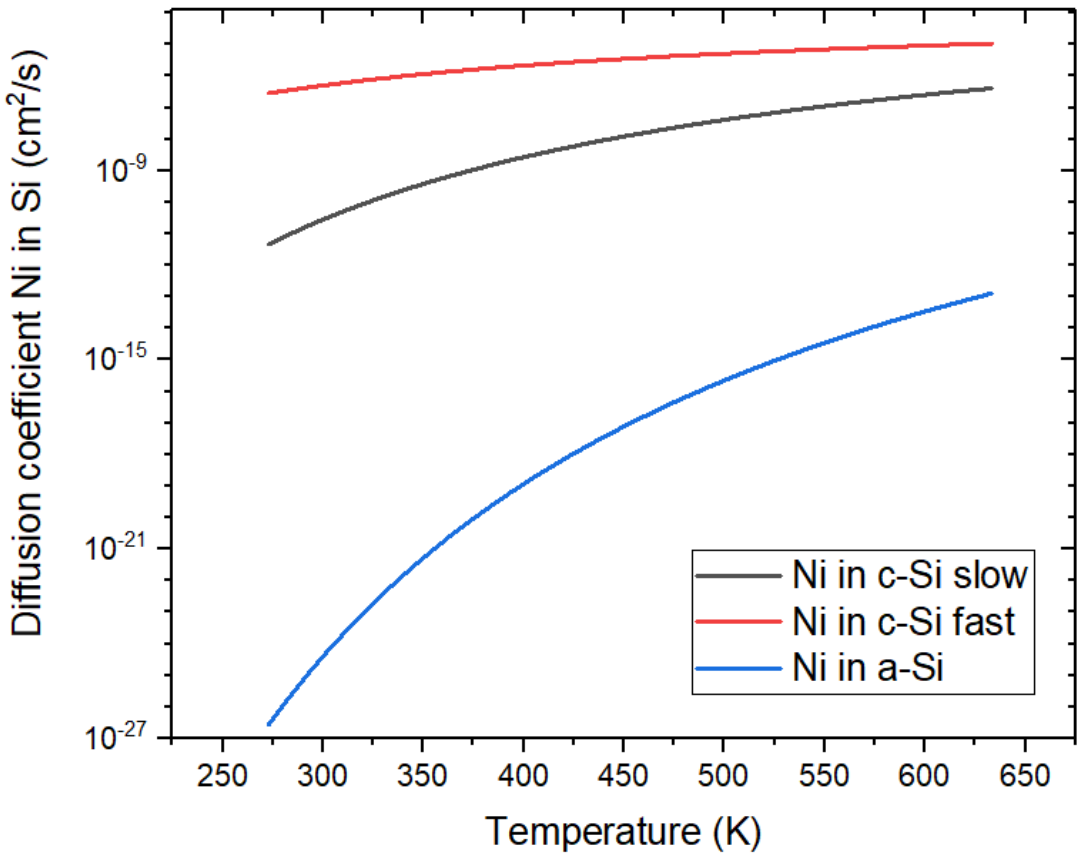


**Figure 2.17:** Diffusion coefficients of Ni in c-Si and a-Si as a function of temperature as reported by Bakhadyrkhanov [69] (black), Lindroos [66] (red) and Kuznetzov [67](blue). The diffusion coefficient proposed by Bakhadyrkhanov varies over 4 orders of magnitude for a temperature range between 0 and 300 °C, while that proposed by Lindroos is a few orders of magnitude higher and varies by only 1.5 orders of magnitude. The diffusion coefficient of Ni in a-Si layers is 15 orders of magnitude lower for room temperature and 7 for $T = 350$ °C, as compared to the diffusion coefficient of Ni in c-Si.

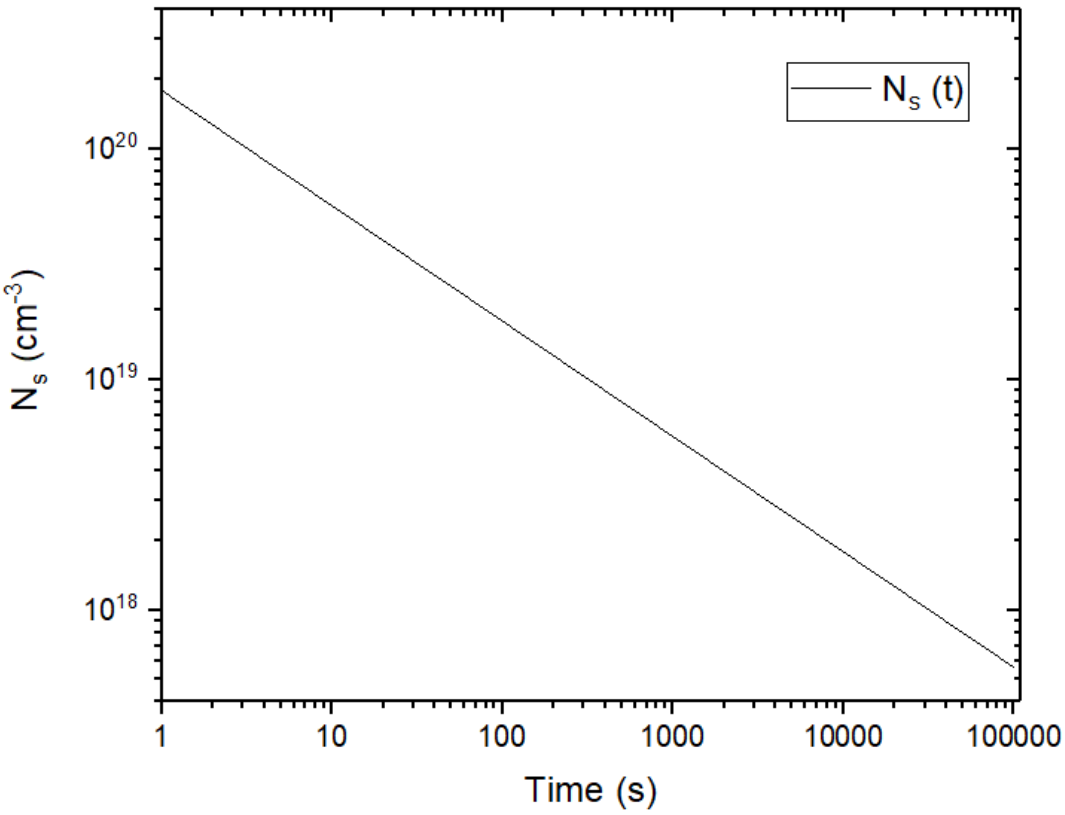


**Figure 2.18:** Nickel surface concentration as a function of time for room temperature using the diffusion coefficient proposed by Bakhadyrkhanov [69]. A diffusion from an exhaustible source into c-Si is considered. It can be seen that the surface concentration decreases over one order of magnitude in the first 100 seconds.

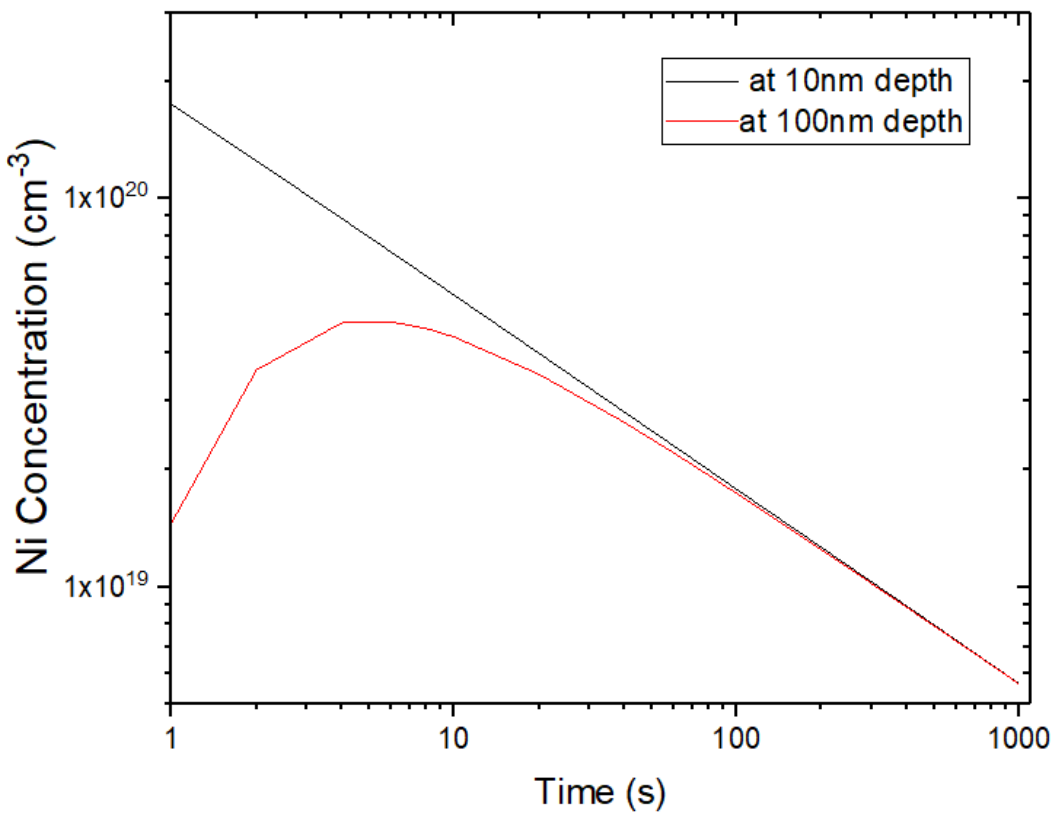


**Figure 2.19:** Ni concentration as a function of time for a depth of 10 nm and 100 nm, assuming diffusion at room temperature from a 1 nm nickel layer on c-Si.

Using the diffusion coefficient of Ni in c-Si for room temperature and the surface concentration as a function of time for a 1nm layer of nickel on c-Si the nickel concentration at a depth of 10 nm and 100 nm can be calculated and is shown in Figure 2.19. This calculation confirms the idea that if nickel atoms reach the c-Si surface a fast diffusion process would take place. The diffusion of Ni in c-Si would introduce recombination sites at the interface (energetic levels inside of the bandgap). This would lead to wafers with low charge carrier lifetimes due to recombination, and solar cells with a low $V_{\mathrm{OC}}$ and $I_{\mathrm{SC}}$.

# 3

# Deposition and Characterization Techniques

## 3.1 Deposition techniques

### 3.1.1 Sputtering

Sputtering is a physical vapor depositon method based on the erosion of a material and the subsequent deposition of the eroded atoms on a substrate. The experimental setup of a sputtering system consists of two plates between which a voltage is placed. On the positively charged plate, called the anode, the substrate to be covered is placed. On the other plate, negatively charged and called anode, the material which will be eroded is placed. This material is called the physical target (Figure 3.1).

In order to deposit films with high purity, the chamber in which the plates are placed is evacuated before the deposition process. After the chamber has reached a certain vacuum level, an inert gas, called process gas, is inserted into the chamber to start the sputtering process. An inert gas is used to ensure that the composition of the deposited film is equal, or at least very similar to the original target, since the process gas will not chemically react with the target.

In order to separate atoms from the physical target, some energy is needed. In the case of the sputtering technique, this energy is supplied by the impact of ionized process gas atoms, in a series of steps explained as follows:

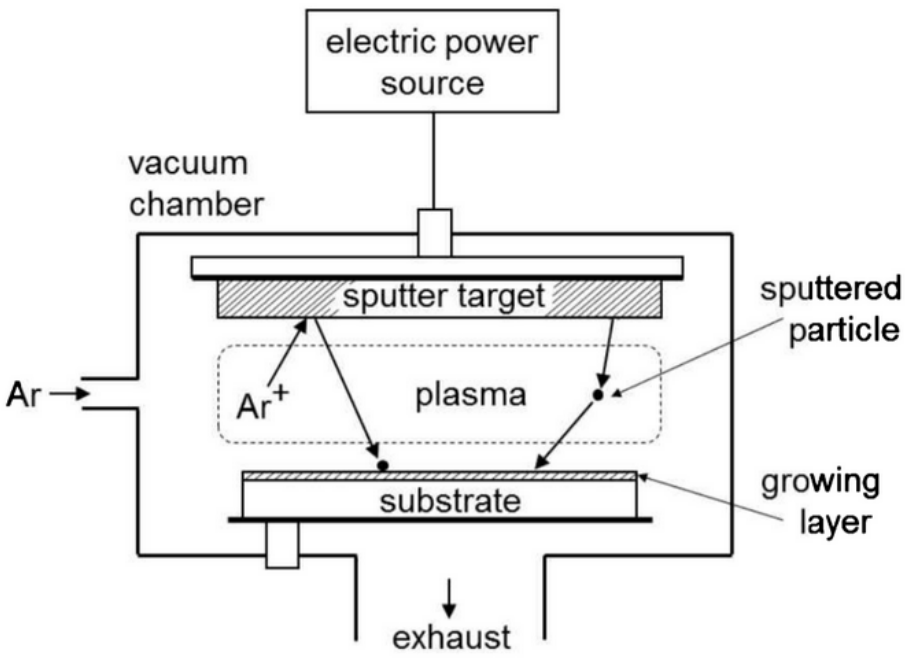


**Figure 3.1:** Sputtering process diagram. Taken from Dittrich [2].

After the process gas is inserted in the chamber and a voltage is set between the cathode and the anode, a high voltage is introduced into the chamber between the anode and the cathode, as shown in Figure 3.1. Since electrons have a very small mass compared to the atoms nuclei, the high voltage is able to separate the electrons from the atoms, ionizing them. The ionized atoms, which are positively charged, are attracted and accelerated to the cathode and by impacting it, transfer their kinetic energy to it, resulting in the separation of atoms from the target, some of which land later in the substrate.

For the work made in this thesis DC magnetron sputtering was used. In this technique, a magnet is placed behind the target, so that a magnetic field exists in the vicinity of it. This field forces the free electrons present in the plasma to move in the region near the target, increasing the probability of a collision between them and an argon atom. This leads to a higher rate of ionized atom argons which then hit the target and produce a higher deposition rate.

During sputtering a mixture of gases can be used if a reaction between the target material and the gas is desired in a process known as reactive sputtering. For the layers of this thesis the amount of oxygen inside the chamber was varied in order to obtain a variation of the film properties.

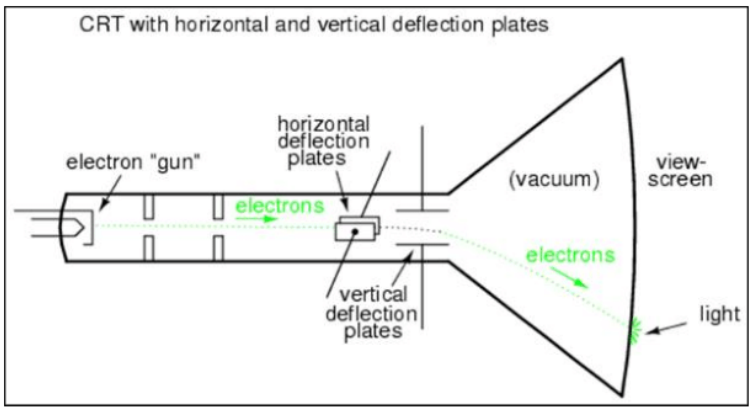


**Figure 3.2:** Cathodic ray tube Taken from Mahmoudzadeh [72].

### 3.1.2 Electron beam evaporation

Electron beam evaporation is a physical vapour deposition technique that makes it possible to heat the source locally, avoiding the problem of the source material reacting with the evaporation recipient.

It's working principle is based in a cathodic ray tube, also known as Crooks tube, a glass tube evaporated with electrodes inside in which electrons can be accelerated between a metallic cathode and an anode by using a potential difference that extracts the electrons of the cathode (Figure 3.2).

The anode of the ebeam system has a small hole in it, so a fraction of the electrons can go through it with a certain speed in what is called an electron beam (see Figure 3.3). On the second part of this setup an electromagnetic field is used to deviate the electron beam into the evaporation crucible directly into the source material.

This deviation of the electron beam is produced by the Lorentz force that the magnetic field causes on the charged particles, which is expressed by the last term of the following equation:

$$\vec{F} = q(\vec{E} + \vec{v} \times \vec{B}) \tag{3.1}$$

The kinetic energy of the electrons hitting the material in the crucible is transformed into heat which leads to the evaporation of the source and subsequent deposition of the material on the substrate placed over it.

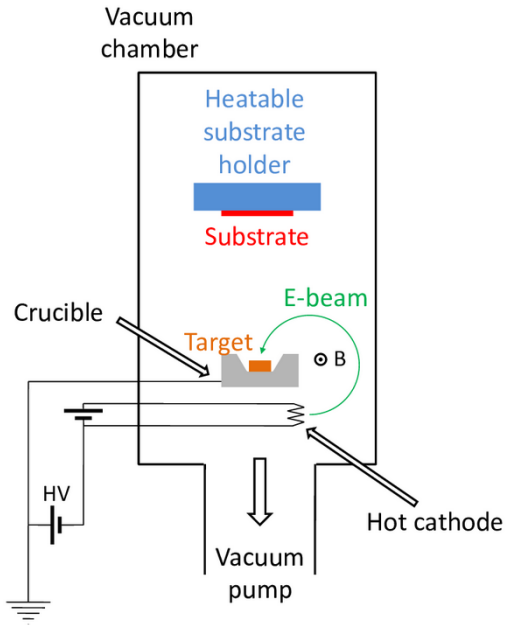


**Figure 3.3:** Electron beam evaporator diagram. Taken from Mazzi [73].

## 3.2 Characterization techniques

### 3.2.1 Sun simulator

A sun simulator is an artificial source of light that simulates the sun spectrum at standard test conditions (AM1.5G spectrum, 1000 W/m$^2$ and a cell temperature of 25 °C). Since the solar spectrum is approximated as the black body radiation spectrum of a black body at 5 800 K, the light source in the sun simulator has to be a combination of lamps which are combined and tuned with the help of filters.

Normally a combination of a halogen lamp and an arc xenon lamp are used to simulate the sun spectrum. The halogen and xenon arc lamps can be described as a blackbody with a temperature of 3 000 K and 10 000 K respectively. The halogen lamp has a very low intensity in the blue and ultraviolet range while the xenon arc lamp has a low intensity in the near infrared region of the electromagnetic spectrum, except for some specific emission lines of high intensity in this region which normally have to be filtered out before the light reaches the solar cell (Figure 3.4).

It can be seen that the halogen and the xenon arc lamp are combined using a half-mirror from where the light gets reflected, filtered to match the AM1.5G spectrum and directed into a collimator which illuminates the solar cell homogeneously. The solar cell is tempered at 25 °C so the standard test conditions are met. In order to illuminate solar cells with an area

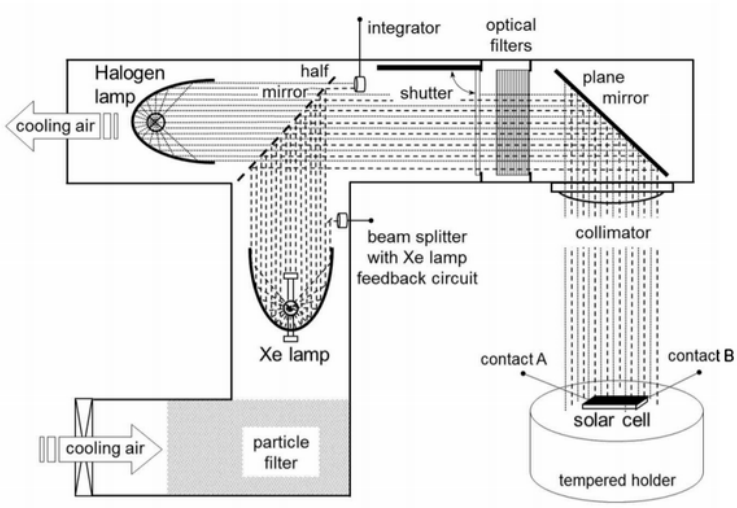


**Figure 3.4:** Experimental setup of a sun simulator. Taken from Dittrich [2].

of $10 \times 10$ cm$^2$, powerful light sources have to be used, so an air cooling system for the lamps is needed. A sun simulator has to be calibrated regularly, since the emission spectrum of the lamps can change over time. A halogen lamp has a lifetime of approx. 50 hours after which it has to be changed. The xenon arc lamp has to be monitored with a feedback circuit to ensure that its current is constant so the intensity of the lamp is stabilized.

### 3.2.2 Ultraviolet-Visible-Near Infrared Spectroscopy

The optical properties of a material, and specifically those of semiconductor thin films, can be determined using spectroscopy in wavelength range comprehending the ultraviolet (UV), visible (VIS) and near infrared (NIR) regions of the electromagnetic spectrum. For this thesis, this kind of measurements were performed using a Perkin Elmer spectrophotometer model Lambda 1050.

The reflection ($R$) and transmission ($T$) spectra of the films were measured from 250 nm to 1500 nm and the absorption of the films was calculated from those values by using the equation:

The experimental setup of the spectrometer (Figure 3.5) consists of a light source and a monochromator which makes it possible to radiate with a specific wavelength the incident light onto the sample. In order to be able to cover the whole spectrum from 250 to 2500 nm two different lamps are used, a deuterium lamp covers the frequencies in the UV region of the electromagnetic spectrum and up to 319 nm after which a halogen Wolfram lamp is used to measure the optical properties in the VIS-NIR range of the spectrum. In order to ensure

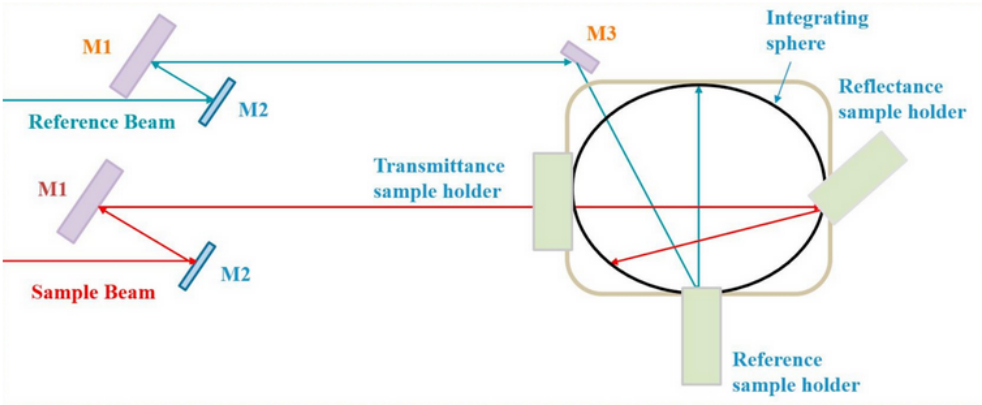


**Figure 3.5:** Experimental setup of the UV-VIS-NIR spectrometer lambda1050. Taken from Ghosh et al. [74].

reliable measurements, the lamps of this system have to be turned on for 20 minutes, so they achieve a stable state and the illumination does not vary during the measurement. Before performing a measurement of the sample, a 0% and 100% baselines are measured in order to calibrate the system. During the measurement of the films, the lightbeam is divided in a reference beam and a measurement beam which strikes in the sample. The transmitted or reflected light, depending on the measurement being made is collected by a photodetector which measures the intensity of the light. An Ulbricht sphere helps to redirect the reflected or scattered photons to the photodetector.

After measuring reflection and transmission of the samples the absorption can be calculated with the formula

$$A(\lambda) = 1 - R(\lambda) - T(\lambda) \tag{3.2}$$

and the absorption coefficient of the material as a function of the wavelength of the incident light can also be calculated using the Beer-Lambert law if the thickness of the film is known.

The optical band gap of nickel oxide was estimated from the absorption spectrum using a Tauc plot with $r = 1/2$ for direct allowed transitions [75].

### 3.2.3 Glow Discharge Optical Emission Spectrometry

Glow Discharge Optical Emission Spectrometry (GDOES) is a characterization technique that combines a sputtering unit with an optical spectrometer. This technique allows the user to obtain a depth profile of the contents of the sample since the working principle of sputtering requires that the sample is gradually ablated. For performing a measurement, the sample is

used as the cathode of a sputtering machine in which a plasma is established. The extracted atoms of the sample enter the plasma and emit electromagnetic radiation with characteristic wavelengths when electrons move between their energy levels.

This measurement technique has many advantages in comparison to other spectrometry techniques such as glow-discharge mass spectrometry or secondary ion mass spectrometry. The GDOES measurements made for this thesis were performed in a GDA650-system of the brand Spectruma Analytik in pulsed radio frequency mode. The system uses an Argon plasma for sputtering and a Charged Coupled Device (CCD) for photodetection of the light coming from the sample atoms during relaxation [76].

### 3.2.4 Photoluminiscence

Photoluminiscence is a characterization technique that allows us to analyze which type of recombination is taking place in a solar cell. Since one of the recombination types includes the emission of a photon with energy equal to the bandgap of the semiconductor material, while the other 3 recombination methods don't, it can be distinguished between them. For silicon solar cells, if the wafers used have high quality so that the SRH recombination is low, this characterization method is very useful since the passivation of surface can be analyzed in a quick and simple way.

There are two kinds of photoluminiscence measurements, in one of them, the solar cell is subjected to a reverse bias so that electrons enter the wafer and recombine. The other method consists in illuminating the wafer with photons with an energy greater than the bandgap of the material, so that charge carriers are generated. For the measurements made in this thesis the second method was used.

If radiative recombination takes place, it can be detected by means of taking a photograph with a CCD sensitive to photons coming with energy in the range of the bandgap of the semiconductor material. It is important for this purpose, that the CCD uses a filter to block out the photons with which the solar cell is being illuminated.

For high quality c-Si samples, like the ones used in this thesis it can be assumed that the concentration of bulk defects is very low and SRH recombination does not play a critical role in the recombination of charge carriers.

For this reason, if no photons are detected when subjecting the solar cell to illumination (or in the other case, to a reverse bias), the predominant recombination mechanism is surface

recombination, which is a sign of a bad or non-existent electronical passivation of the dangling bonds.

For this work, passivated silicon wafers were analysed after the nickel oxide deposition in order to find out if the deposition of nickel oxide by means of e-beam evaporation has a detrimental effect on the passivation properties of the a-Si:H layers deposited on the surface.

Details and applications about this technique for silicon solar cells can be found in Trupke et al. [77].

### 3.2.5 X-ray Photoelectron Spectroscopy

X-ray Photoelectron Spectroscopy is a characterization technique that makes it possible to analyze the surface (approximately the first 3–5 nm) of a material [78], in our case of the thin films prepared by e-beam evaporation. The working principle of XPS is the photoelectric effect, which states, that the electrons of an atom can be set free by a photon interacting with them, if the photon possess an energy equal or greater than the binding energy between the electron and the atom.

If a photon with an energy $X$ interacts with a surface electron of a material, and sets it free, it is possible to measure the kinetic energy $K$ that the electron has after leaving the energy potential it was bound to, and the difference between this two values will be equal to the binding energy of the electron to the atom. It must be noted, that in order to detect enough electrons extracted from a material, a large amount of photons with energy $X$ is needed, making it necessary to have a source of monochromatic photons at one's disposal.

Expressed in another way, if a sample of a certain material is illuminated with a monochromatic source of high energetic photons, the kinetic energy of the extracted electrons gives us information about the electronic core level in which they were before the electron-photon interaction.

Obtaining a monochromatic source of high energetic photons (in the range of X-ray) is not a difficult task, since it was found by Röntgen in 1895, that, if a high voltage of the order of 30 keV is placed between the electrodes of a cathodic ray tube, and the emission spectrum of it is measured, some emission lines unique for each element, appear over the Brehmsstrahlung spectrum, which can be seen only at lower voltages.

A radiation spectrum of a molybdenum target set under a potential difference of 35 kV is shown in Figure 3.6. Both the Bremsstrahlung spectrum and the characteristic X-rays of molybdenum can be seen as well.

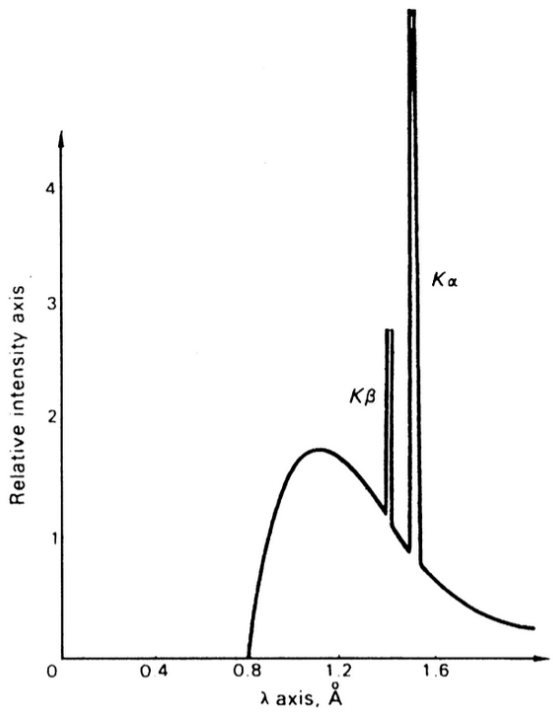


**Figure 3.6:** Characteristic spectrum of an X-ray tube. The high intensity signals $K\alpha$ and $K\beta$ coming from the electronic transitions between energetic levels can be seen over a continuous spectrum caused by Bremsstrahlung. Taken from Ladd et al. [79].

| **Transition Levels from** | **to** | **Emission Line** |
|---|---|---|
| 2 | 1 | K$\alpha$ |
| 3 | 1 | K$\beta$ |
| 4 | 1 | K$\gamma$ |
| 3 | 2 | L$\alpha$ |
| 4 | 2 | L$\beta$ |
| 4 | 3 | M$\alpha$ |
| 5 | 3 | M$\beta$ |

**Table 3.1:** Transitions of characteristic X-ray emission.

This characteristic emission lines are photons emitted by electrons moving between electronic levels of the mentioned element, more specifically moving from outer to inner electronic levels, and emitting a photon with an energy equal to the difference in energy between levels (see Figure 3.7). These lines are only seen at such high voltages between electrodes, because a high energy is needed in order to eject the electrons placed in the electronic levels nearer to the nucleus.

The names of the emission lines give the information about the levels between which the transition is taking place, and can be seen in Table 3.1.

As it have been experimentally measured, the transition from electrons from the second to the first electronic core level has a higher probability to occur than the other ones and,

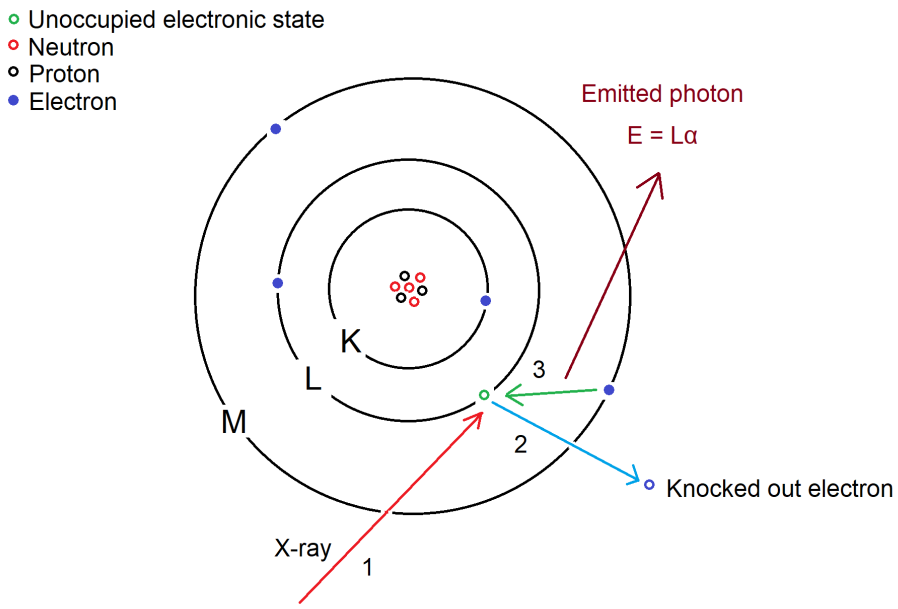


**Figure 3.7:** Emission of characteristic X-rays as a working principle for XPS. An X-ray (1) knocks out an electron from its energetic position (2), and an electron in a higher energetic state (3) moves to the unoccupied state emitting a photon with energy equal to the energetic difference between states

therefore, the first line of the spectrum (so to say, the K$\alpha$) has the highest intensity of these spectral lines and can therefore be used as a beam of monochromatic electromagnetic radiation.

In our setup, we are able to use two different materials for the X-ray producing anode, aluminum and magnesium, which gives us the possibility of investigating the surface of materials with X-rays of wavelength $\mathrm{Al}_{K\alpha} = 1486.6$ eV and $\mathrm{Mg}_{K\alpha} = 1253.6$ eV.

Once having this source of monochromatic X-rays it is possible to direct it to a material sample and analyze the electrons that are set free due to the photoelectric effect and measure their kinetic energy. The kinetic energy with which these electrons exit the material is equal to the energy of the incident X-rays minus the binding energy of the electrons. The raw results of the measurements are then analyzed using a software called XPSPEAK 4.1[1]. The signals are fitted using Voigt profiles which consist of the convolution of a Gaussian and a Lorentzian distribution (15% and 85% respectively). Different functions were used for fitting the background: in the case of the nickel, a Shirley background function was used and in the case of the oxygen XPS signal a linear background.

[1]Open software for the analysis of XPS spectra written by Raymund Kwok. https://xpspeak.software.informer.com/4.1/

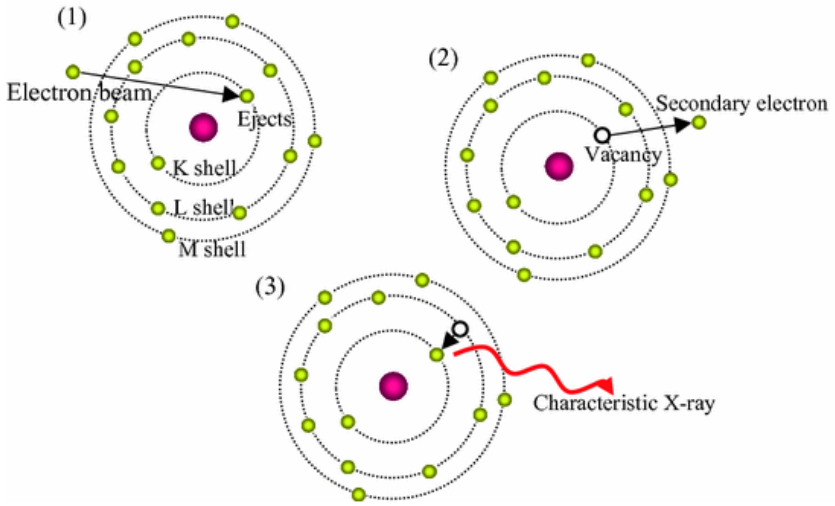


**Figure 3.8:** EDX working principle 1) a primary electron interacts with an electron in one of the inner energy levels of an atom, and ejects it from its orbital. 2) the ejected electron, called the secondary electron leaves its energy level empty. 3) an electron in a higher energy state moves to the lower energy level, emitting an x-ray photon in the process with energy equal to the difference of energy between the electronic levels. Taken from Morita [80].

### 3.2.6 Energy Dispersive X-ray diffraction

Energy Dispersive X-ray difraction is an analytical technique used to characterize the chemical composition of a sample. Its working principle is based in the analysis of characteristic X-rays emitted by electrons moving between the energy levels of the atoms of the sample, when excited by a beam of high energetic electrons.

The incident electrons, coming from an electron gun, in which the electrons are accelerated between a cathode and an anode, are called the primary electrons. If they interact with electrons inside the sample, they will transfer their energy to them and set them free from their atomic orbital. The electrons which were set free are called the secondary electrons. Neighbouring electrons positioned in a higher energy level can move to the lower, and now free electronic level, emitting during this process a photon with an energy equal to the difference in energy levels (normally in the x-ray region of the electromagnetic spectrum).

Since the difference between energy levels is unique for each element, the composition of the sample can be identified if the outcoming radiation of the sample is analysed with a diffractometer.

In comparison to XPS, EDX is able to analyze the bulk of the material, due to a larger penetration depth of the incident electrons, and the ability of the produced characteristic X-rays of the sample to leave the probe without interacting again with atoms in the sample.

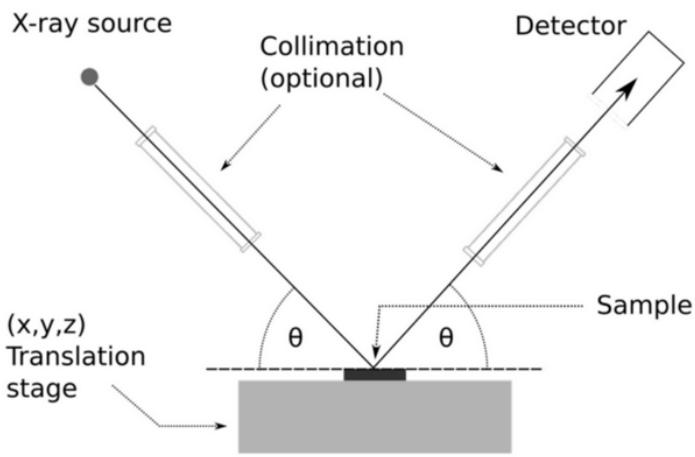


**Figure 3.9:** X-ray diffraction experimental setup. Taken from Kuhlmann [81].

For this thesis, the composition of 500 nm thick nickel oxide layers deposited under different oxygen pressures was analysed using electrons at an acceleration potential of 5 kV in a Hitachi 4100 with EDAX-System ApolloXV, Genesis. The primary electrons were accelerated with a potential of 5 kV, and no signal from the substrate was recorded, so the excitation volume was completely composed of the nickel oxide layer.

### 3.2.7 X-ray Diffraction

X-ray Diffraction is one of the most used techniques for characterization of crystalline materials. A monochromatic, collimated X-ray beam is directed to a crystalline probe with an incident angle that varies from normal incidence (0°) to almost parallel incidence (90°). A photodetector measures the intensity of the reflected light at an angle equal to the incident angle on the other side of the perpendicular line to the material, as shown in Figure 3.9.

Due to the fact that X-rays are electromagnetic waves and follow the superposition principle, the detected wave at a certain angle theta will be the superposition of the waves reflected by the parallel planes of the crystalline sample. The difference in optical path between a wave reflected by the first plane and the second plane is a function of the distance between planes and the incidence angle of the X-ray beam.

If the optical path difference is an integer multiple of the X-ray wavelength, there is no phase difference between the detected waves and they interfere constructively, so a larger signal is detected than for other incident angles. In particular, according to Braggs' law, there will be constructive interference when the following condition is met:

$$2d \sin\theta = n\lambda \tag{3.3}$$

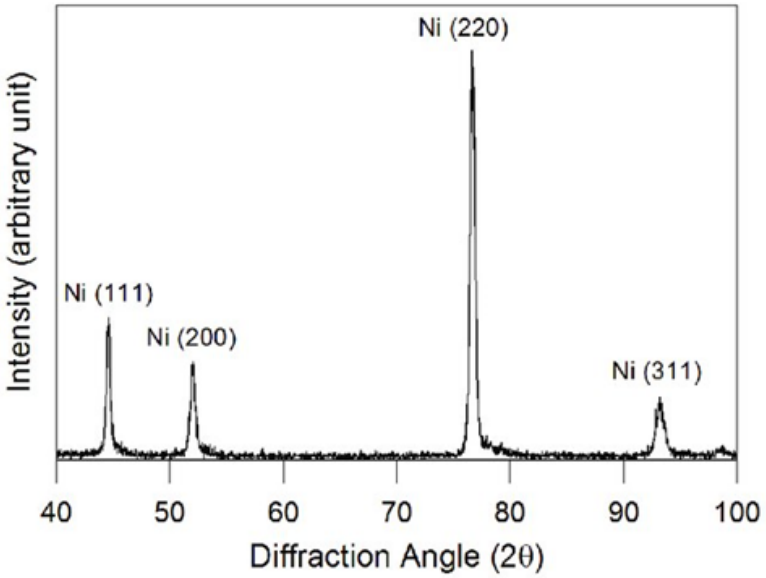


**Figure 3.10:** XRD pattern of electrodeposited nickel showing the main crystal plane orientations of this material. Taken from Ul-Hamid et al. [82].

where $d$ is the interplanar distance, lambda the wavelength of the incident X-rays, $\theta$ the incident angle and $n$, an integer number. It is possible then, if the wavelength of the X-rays is known, to determine the interplanar distance of a crystal by finding those angles where the interference is constructive. An XRD pattern of electrodeposited Nickel is shown in Figure 3.10.

### 3.2.8 Photoconductance decay measurements

In order to measure the lifetime of the minority charge carriers of a passivated wafer, a WCT-100 equipment from Sinton Consulting was used. The measuring system uses a short illumination pulse in order to generate free charge carriers in the wafer and measures the conductance of the wafer and therefore the amount of free charge carriers in it, as a function of time after the pulse. The amount of free charge carriers in the sample decreases over time due to recombination and if the decreasing pattern is analyzed the lifetime of the charge carriers as a function of their concentration can be calculated. The working principle of the measurement system is explained in detail in Sinton and Cuevas [83].

A typical measurement of this system looks like Figure 3.11 and contains information about the injection levels at which the different types of recombination takes place.

The minority charge carrier lifetime is limited by Auger recombination at high injection levels and by SRH recombination at low injection levels.

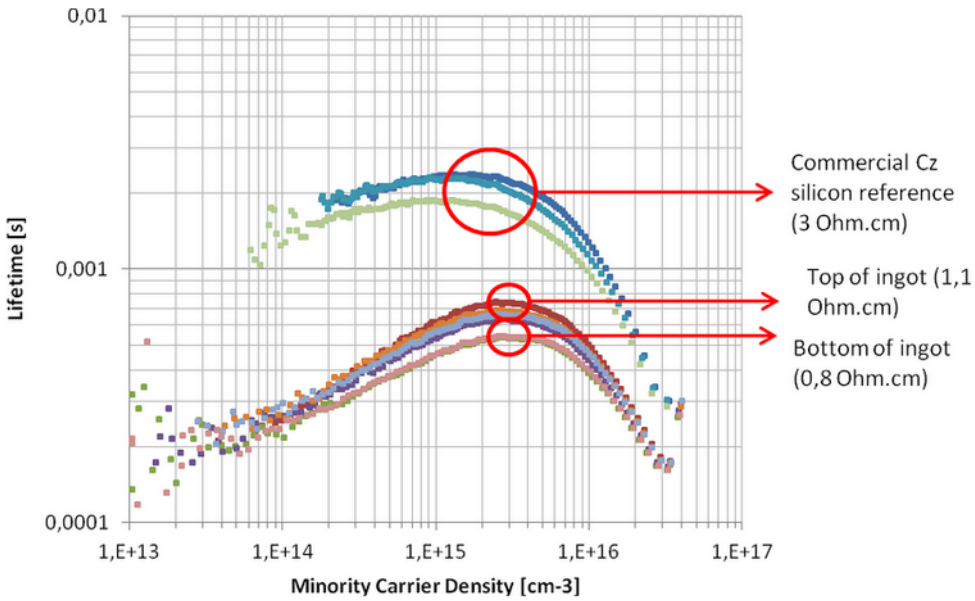


**Figure 3.11:** Minority carrier lifetime as a function of minority carrier density (injection level) of wafers taken out of different parts of a silicon ingot. It can be seen that the wafers taken from the extremes of the ingot show a lower charge carrier lifetime. Taken from Einhaus et al. [84].

### 3.2.9 Suns $V_{OC}$

This characterization technique, makes it possible to analyze the performance cell as if no series resistance were present in it. Its working principle is based in the illumination of a solar cell by a flash, which intensity decays over time, so a variation of the $V_{OC}$ of the solar cell is measured, Using the short circuit current density $j_{sc}$ obtained from the measurements in the sun simulator, a pseudo IV curve can be produced, which represents what the performance of the solar cell would be if no series resistance were present.

By comparing the real IV curve of a solar cell with its pseudo IV curve, the series resistance of it can be determined. For example by dividing the voltage difference between the pseudo IV curve and the real IV curve of the solar cell in the maximum power point, and dividing it by the current that is flowing through the solar cell in that point [85].

### 3.2.10 Transmission Line Measurements

In order to measure the sheet resistance and the contact resistivity of the ZnO:Al and ITO with the silver grid, Transmission Line Measurements (TLM) structures were prepared on the silicon wafers. TLM is a simple characterization method which can be used to obtain information about the electronical transport of layered materials.

The working principle is relatively easy to understand, TLM structures give us information about a system composed of two materials, normally used for thin films. In order to perform

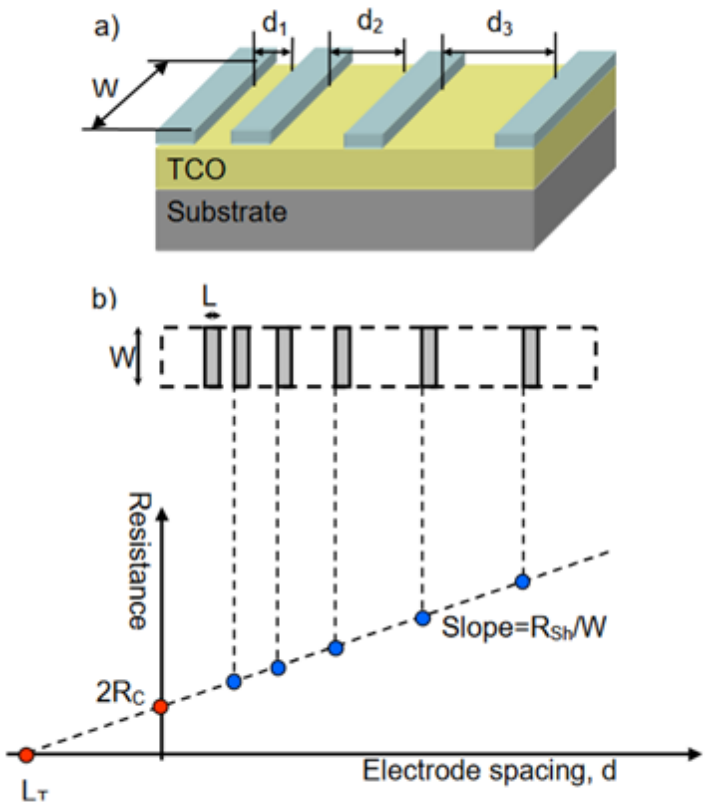


**Figure 3.12:** TLM structures and typical TLM measured data. a) representation of a TLM structure for a TCO/grid system, and b) graph of the measured data. Taken from Marinkovic [86].

the measurement, a sample of one material with a homogeneous thickness is prepared and thin stripes (at least three) of the other material are placed on top of it, such that no physical discontinuities of the first material exist as it is shown in Figure 3.12a.

The distance between the stripes and the resistance between every couple of stripes is also measured, resulting in a set of points with coordinates (distance, resistance) as shown in Figure 3.12b. If these points are plotted, and a straight line is fitted to them, the slope of the line will give us information about the sheet resistance of the material placed below, while the point where the line crosses the vertical axis gives us information about twice the contact resistance of the system.

In this thesis the systems ITO/silver and ZnO:Al/silver where analyzed in order to compare the contact resistivity of those materials with the silver grid.

The working principle can also be found in detail in Marinkovic [86] and Pysch et al. [85].

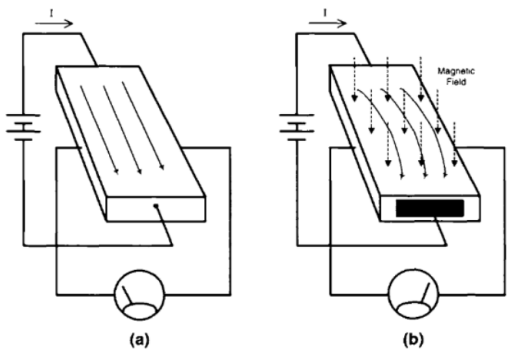


**Figure 3.13:** a) current flowing through a conductor with no magnetic field acting on it. b)current flowing through a conductor with a magnetic field perpendicular to the current flow. A voltage between the sides, called the Hall Voltage appears due to the lateral deviation of the electrons. Taken from Ramsden [87].

### 3.2.11 Hall effect measurements

A widely-used technique for measuring electronical properties of materials is the Hall effect. Some of the properties that can be accurately measured are for example mobility of the charge carriers and the conductivity of the material. For performing this measurement, a voltage is placed between two sides of the conducting material, so that a current is established. The setup is immersed in a magnetic field in which the moving electrons feel a force (Lorentz Force) that deviates them from their direction in a direction perpendicular both to the magnetic field and the current, so that they group on one of the extremes of the sample and a voltage, called the Hall voltage, can be detected (Figure 3.13).

For the layers presented in this work a measurement of the Hall effect in the van der Pauw geometry was performed. The van der Pauw geometry consists of a system with four electrodes,which are placed on the edges of a small square sample (approx 1 $cm^2$) and through which a measurement of the voltage and the current on separate pair of electrodes takes place to determine the resistivity of the sample, and also when the sample is immersed in the magnetic field, to measure the Hall voltage.

In order for this measurement to be reliable some conditions have to be met by the film. The film has to have a homogeneous film thickness and present no holes on its surface. The thin film samples should be contacted at the edges, and the size of the contacts should be smaller than the edges of the samples.

The details about this measuring technique can be found in many references such as Sze and Ng [3] and specific information about the van der Pauw configuration can be found in Pauw [89].

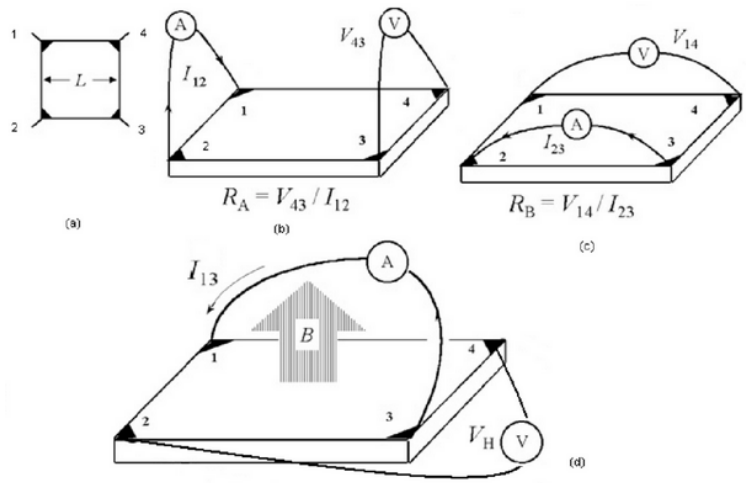


**Figure 3.14:** Hall effect measurement in the van der Pauw geometry. Voltage and current are measured with two pairs of needles on different corners of the sample. Taken from Narang [88].

Hall measurements for the ZnO:Al, ITO and NiOx single layers on glass were made using the van der Pauw geometry with the HMS-3000 Ecopia system. The magnetic field used in this system is a permanent magnet with a magnetic field of 0.56 T.

### 3.2.12 Mercury probe

The mercury probe is a non destructive and fast measurement technique for determining the electrical properties of conducting materials [90]. During the measurement, the sample is contacted using mercury electrodes with a well defined area and separation between them.

In order to achieve that the mercury gets into contact with the sample a vacuum pump is used to move the mercury upwards to the sample. After the sample has been contacted, an IV relation is measured in order to determine the resistance of the sample. If the thickness of the sample is known the resistivity can also be calculated.

# 4

# Experimental Approach

## 4.1 Aluminium doped zinc oxide layers

For optical and electrical characterization ZnO:Al and ITO layers were deposited on low-iron soda-lime glass (Saint-Gobain planiclear, $30 \times 30$ cm) using a pulsed DC magnetron sputtering system from Leybold Optics (A600V7). For ZnO:Al deposition a rotatable target (99:1 wt. % $ZnO:Al_2O_3$) was used, and for the ITO layers, a planar target (97:3 wt % $In_2O_3$:$SnO_2$). The rotatable target is 600 mm long and has a diameter of between 130 mm used and 166 mm new. The planar target is 600 mm long and 125 mm wide.

Both materials were deposited at a nominal substrate temperature of 200 °C. During sputtering, the mixture of oxygen to the argon sputtering atmosphere was used to tune the stoichiometry and conductivity of the layers. The $O_2$ flow ratio $r(O_2)=(O_2)/(Ar+O_2)$ was varied between 0% and 0.74% for the ZnO:Al and 0% and 5% for the ITO deposition.

Charge carrier concentrations and Hall mobility of the layers on glass were determined by Hall measurements in the van der Pauw geometry. Sheet resistance was measured using a four point probe. Layer thicknesses were obtained fitting a Drude-Lorentz-oscillator model to optical spectrometry measurements. All layers deposited on glass had a thickness of $98 \pm 6$ nm which, when deposited on textured silicon wafers with random pyramids, results in an effective thickness of 70–80 nm.

An initially 145 $\mu$m thick n-type Cz-Si wafer was used as the base. After saw-damage-etching, texturing and RCA cleaning, the amorphous intrinsic and doped silicon layers were deposited in an AKT1600 Plasma-Enhanced Chemical Vapor Deposition (PECVD) cluster

tool from Applied Materials. As the front-surface field and contact material to the front TCO a nanocrystalline silicon n-type layer was used [91]. For the back emitter an amorphous silicon p-type layer was used. TCO sputtering was done through shadow masks to define 4 $cm^2$ size cells.

For all cells the front metal-grid contacts were carried out by screen printing of silver contact grids which covered 2.7% of the cell area and was cured at 170 °C for 7 minutes. For bifacial cells the back contacts also consisted of screen printed silver grids, whereas full-area sputtered silver layers were used instead for monofacial cells. The rear contact of the monofacial solar cells was created using 80 nm ZnO:Al + 200 nm silver over the active area.

Five groups of samples, with two wafers each, were prepared. Each wafer holds 14 bifacial SHJ solar cells, three TLM structures and three grid-less solar cells for EQE measurements. Four groups feature a ZnO:Al front TCO sputtered with different $O_2$ concentrations (oxygen content variation), and are named according to the oxygen partial pressure during deposition, ZnO:Al 0%, ZnO:Al 0.3%, ZnO:Al 0.48% and ZnO:Al 0.74% respectively. One group, with ITO as front TCO is used as a reference and is named ITO 2.8% according to the oxygen partial pressure under which it was deposited. All of these samples have a 80 nm thick ITO layer in the back and were processed in bifacial configuration. To test the performance of ITO-free cells, one extra group of two wafers with 14 monofacial solar cells with ZnO:Al as the front and a ZnO:Al/Ag rear contact, was prepared and named MF ZnO:Al 0.3%. Special cells without grid were prepared for the EQE measurements.

The solar cells were characterized using illuminated IV measurements under AM1.5G illumination and standard test conditions in a dual source class AAA+ sun simulator. Intensity dependent open circuit voltage (SunsVoc) was measured using a Sinton Instruments WCT120. UV-VIS spectrometry was measured on a Perkin-Elmer LAMBDA 1050 UV/Vis/NIR Spectrophotometer. EQE and electrical measurements on the TLM structures were also made.

A calculation of the series resistance ($R_s$) of the cells is done adding the series resistance due to the transport through the TCO ($R_s^{\mathrm{TCO}}$) and the contact resistance between the TCO and the metal grid ($R_s^c$). This is a simplified calculation of the series resistance of the cell, since the contact resistivity between the TCO and the nanocrystalline silicon n-layer is neglected for these calculations, as well as the transport through the silicon wafer. Nevertheless, it represents qualitatively the electronic transport through the front stack of the solar cell in a way that allows us to understand the trends observed in the $FF$ and $j_{\mathrm{sc}}$ results of the section 5.1.3. $R_s^{\mathrm{TCO}}$ and $R_s^c$ were calculated using the sheet resistance ($R_{\mathrm{sh}}$) and contact resistivity ($\rho_c$) data

extracted from the TLM measurements and the mean distance travelled by the charge carriers through the TCO and the area of the contact, respectively. The area of the contact is taken as the area of the silver grid (2.7% of the total area).

## 4.2 Nickel Oxide layers

For characterization of single layers, NiOx was deposited on glass substrates using a UNIVEX450 e-beam equipment from Leybold systems. The precursors for these depositions were nickel pellets (Merck 99.9%) and gaseous oxygen (air liquide, $O_2$ N48). A graphite crucible was used to contain the nickel pellets. A variation of the oxygen content in the deposition atmosphere was undertaken, in order to investigate the possibility of producing layers with a variation in their electronical and optical properties. The UNIVEX450 ebeam equipment is able to reach a base pressure of approximately $1 \times 10^{-7}$ mbar, which sets the lower pressure limit for the depositions. On the other side, the upper limit of the available pressure conditions is determined by the highest possible pressure under which an electron beam between anode and cathode can be maintained. In our experimental configuration this value is reached at about $5 \times 10^{-3}$ mbar. The high voltage established between electrodes in the UNIVEX450 is 20 kV, and the operation current of the system is limited at 30 mA. This upper limit is set for health safety reasons related to the amount of radiation emitted by the e-beam system. Specifically that in the X-ray part of the electromagnetic spectrum.

The layer thickness determination was made using an Omni 3 quartz oscillator from Sloan, working at a frequency of 6 MHz, which is placed inside of the UNIVEX450 in spatial proximity of the substrate holder. The parameters used for determining the thickness of a pure nickel layer were found in the documentation of this equipment (density = 8.91 g/cm$^3$, Z factor = 0.33 and tooling factor = 115). For oxygen containing layers this value was adjusted by calibrating the quartz detector with thickness measurements made with a DektakXT profilometer from the manufacturer Bruker.

The characterization of the samples was made in two groups. One of them is mostly qualitative and mainly tries to answer the question about the possibility of producing oxygen-containing nickel layers using reactive e-beam evaporation. The other group of measurements is of quantitative nature and is focused on analyzing the electric and optical performance that this layers would have on a SHJ solar cell when implemented as a TCO or a charge selective contact.

XPS and EDX measurements were used to determine the existence of oxygen inside the deposited layers. According to the information depth distance of these two techniques (approx. 5 nm for XPS and 300–500 nm for EDX), using both of them gives us sufficient information about the chemical composition of the samples. XPS was made on 110 nm thick layers on glass substrates, using the $Al_{K\alpha}$ spectral line as excitation energy (1.486 keV). The XPS measurements were made on the $Ni_{2p}$ and $O_{1s}$ electronic core levels.

The XPS measurements were fitted using the software XPS peak fit, and according to the NiOx reference measurement presented in Mansour [92]. The presence of oxygen in the layers was correlated with the appearance and area-increase of the $O_{1s}$ XPS peak, as well as the form change of the $Ni_{2p}$ XPS peak. The similarity between the $Ni_{2p}$ XPS peak of samples deposited under an oxygen atmosphere and the NiOx reference [92] also suggests that a bonding between nickel and oxygen atoms in the layer is taking place.

For the EDX measurements, 500 nm thick layers were deposited on glass at three different oxygen pressures in order to investigate the presence of oxygen in the bulk of the material. The primary electron beam was accelerated with a 5 kV potential in a Hitachi 4100 with EDAX-System ApolloXV. No signal of the substrate was detected, so it can be assured that the excitation volume lies inside the NiOx layer.

The group of quantitative measurements includes optical characterization using UV-VIS spectrometry, and electrical characterization by means of Hall-effect measurements and measurement of the conductivity using the Hg Probe.

The UV-VIS measurements were performed in a Perkin-Elmer LAMBDA 1050 UV/Vis/NIR Spectrophotometer and further analyzed using Tauc plots for determining the bandgap of the deposited material, using the exponent $r = 1/2$ for an indirect allowed transition.

In order to analyze the effect of annealing temperature on the NiOx layers, annealing of the samples on a hot plate at temperatures of 120, 240, 360, 480 and 600 °C, for 10 minutes were performed, after which UV-VIS and Hall measurements were repeated.

Another set of samples, consisiting of 200 nm layers of NiOx were deposited on glass while varying the substrate temperature and then analyzed using X-ray diffraction in a Bruker D8 Advance XRD equipment, in order to find which crystalline structure the deposited material is deposited with, and if the substrate temperature during the deposition has an effect on its crystallinity.

Photoluminiscence measurements were made on electronically passivated silicon wafers covered. The passivation was achieved by depositing a-Si:H during a PECVD process using

hydrogen and silane gases with a $H_2$ to $SiH_4$ ratio of 3 (15 sccm $H_2$ to 5 sccm $SiH_4$) and a plasma power of 18W. The wafers were then covered with thin (5–10 nm) Ni and NiOx layers in order to analyze the effect of the e-beam deposition process on the passivated interface of the layered system. The e-beam deposition of NiOx on Si wafers was made using different mask configurations to achieve a better understanding of the detrimental effect produced on the passivation of the silicon. The masks used were glass, metal and glass+metal. A second experiment involving masks was done using glass directly in contact with the silicon wafer, or separated from it using glass spacers to allow the direct exposure of the wafer to the oxygen molecules present in the deposition atmosphere.

GDOES measurements were performed on c-Si wafers covered with thick a-Si layers (100–300 nm) and NiOx layers, which were subsequently annealed at 200 °C for different times in order to investigate the phenomenon of diffusion of nickel atoms through a-Si. The GDOES measurements made for this thesis were performed in a GDA650-system manufactured by Spectruma Analytik and were carried out in pulsed radio frequency mode. The system uses an Argon plasma for sputtering and a CCD for photodetection of the GDOES signal. Details of the setup can be found in Kodalle et al. [76].

# 5

# Results: Aluminium Doped Zinc Oxide

## 5.1 Comparison between ZnO:Al and ITO as a TCO for SHJ solar cells

This chapter presents results of SHJ solar cells with ZnO:Al replacing the commonly used ITO as the front TCO. This is done in order to replace indium by the much more abundant and lower-cost zinc. Generally, ITO features better opto-electronical properties, namely lower resitivity at comparable transparency, when deposited as approx. 100 nm thin layer at a rather low temperature of typically 200 °C, as is used for SHJ cell fabrication. It was, however, proposed by Bivour et al. [21] that for an adopted device design, namely with the p-type contact (junction or "emitter") at the rear side instead at the front side, which is generally done, the constrain on the conductivity of the TCO can be relaxed. This is because in rear-emitter configuration a more significant part of the lateral current transport is carried by the Si wafer, as compared to the front-emitter configuration.

The layers analysed in this section were prepared using DC magnetron sputtering under an atmosphere containing oxygen to be able to make a variation of the thin films properties. Sputtering is one of the most used techniques for depositing thin films of materials thanks to the control over the process and reproducibility, details about this deposition method can be found in Section 3.1.1.

The following section consists of the results published in Meza et al. [4].

### 5.1.1 ZnO:Al single layers on glass

Figure 5.1 a) and b) show sheet resistances ($R_{\mathrm{sh}}$) of about 100 nm thick ZnO:Al and ITO layers on glass, as well as the absorbed light expressed as an equivalent photo-current density ($j_{\mathrm{loss}}$). The $j_{\mathrm{loss}}$ value is calculated by multiplying the spectrally resolved absorption of the samples with the AM1.5G spectrum, integrating over the wavelength range from 300 to 1200 nm, and subtracting the absorption of the planiclear glass. This method for estimating the absorption of the TCO layer is used due to the similarity of the samples prepared, since all of them are deposited on the same substrate, with the same layer thickness and their refraction indexes and reflection are very similar. Both $R_{\mathrm{sh}}$ and $j_{\mathrm{loss}}$ are plotted against the oxygen partial flow during film deposition. Figure 5.1c) shows Hall mobility ($\mu$) vs charge carrier concentration ($N_e$) for the same layers.

The $R_{\mathrm{sh}}$ value of ZnO:Al layers deposited with increasing oxygen ratio in the process gas increases from 120 Ω/sq to 226 Ω/sq (sputtered under r($O_2$) = 0% and r($O_2$) = 0.74 %, respectively).

$N_e$ decreases from $2.2 \times 10^{20}$ cm$^{-3}$ to $1.3 \times 10^{20}$ cm$^{-3}$ for the same variation of $O_2$ partial flows, which is consistent with observations by Ellmer [93] and is often tentatively explained by a reduced density of oxygen vacancies in the TCO material, since oxygen vacancies provide intrinsic doping on ZnO. The Hall mobility stays almost constant around 20 cm$^2$/Vs for higher $N_e$ and decreases to 18 cm$^2$/Vs for the sample with the lowest $N_e$.

The $R_{\mathrm{sh}}$, $\mu$ and $N_e$ values of the ITO layers follow a similar trend. $R_{\mathrm{sh}}$ increases from 55 Ω/sq to 405 Ω/sq for an $O_2$ concentration increasing from r($O_2$) = 0% to r($O_2$) = 5 %. Hall mobility maximum values of 30–35 cm$^2$/Vs are reached for layers with carrier concentrations of 1–2 $\times 10^{20}$ cm$^{-3}$, decreasing for both increasing and decreasing carrier concentrations.

The Hall mobilities and charge carrier densities measured on our layers are in the same range as those reported in literature for comparable sputtered ZnO:Al and ITO layers [93, 94]. The decreasing $\mu$ with decreasing $N_e$ (for $N_e \leq 1 \times 10^{20}$ cm$^{-3}$) can be explained using the grain boundary scattering model [95]. In this model it is assumed, that the boundaries between adjacent grains or crystallites have a relatively high amount of trap states which are able to reduce the effective amount of charge carriers by trapping them. The trap states become electrically charged by this process and represent then an electrical potential barrier to the free charge carriers, reducing their Hall mobility.

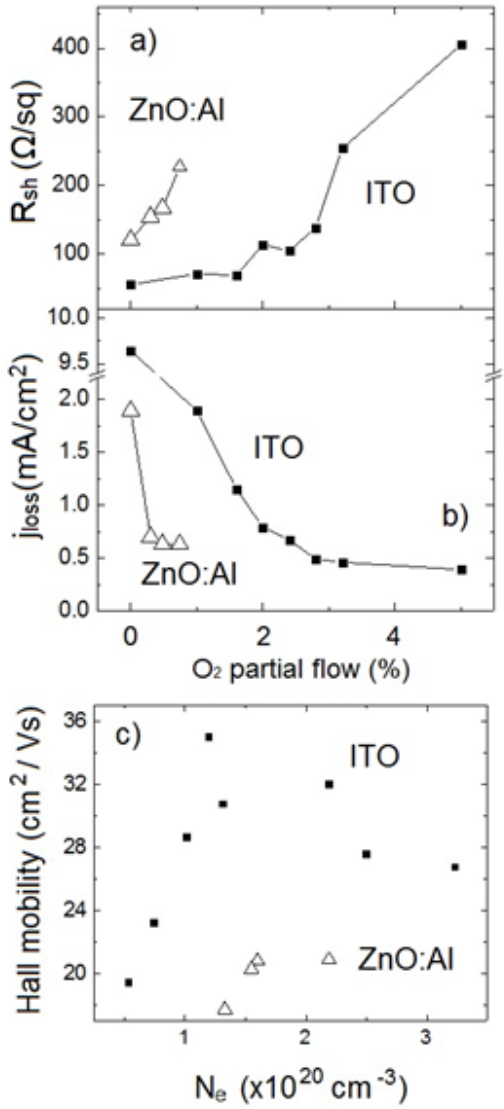


**Figure 5.1:** Optoelectronical properties of ZnO:Al and ITO layers. a) Sheet resistance and b) $j_{\text{loss}}$ due to absorption in the 300–1200 nm range of the ZnO:Al (open triangles) and ITO (filled squares) single layers on glass deposited under different $O_2$ concentrations. c) Hall mobility as a function of charge carrier concentration. Note the axis breaks in panel (b).

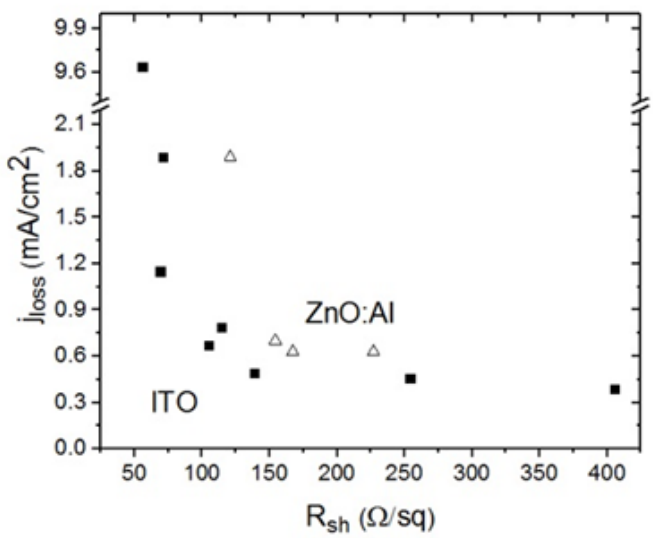


**Figure 5.2:** Sheet resistance vs. $j_{\text{loss}}$ due to absorption of the ZnO:Al (open triangles) and ITO (filled squares) single layers on glass. The sheet resistance values of this figure were measured with a four point probe. The optical absorption is similar for samples with a sheet resistance between 100 and 200 Ω/sq. Note the axis break in the vertical axis.

The increasing light absorption correlates with the increase of Ne extracted from the Hall mobility measurements [96].

From these measurements and calculations we found, that ZnO:Al and ITO layers deposited under r($O_2$) = 0.3% and r($O_2$) = 2.8%, respectively, exhibit similar $R_{\text{sh}}$ (approx. 150 Ω/sq) and optical absorption values (photocurrent-equivalent absorption loss 0.7 mA/cm$^2$ for the ZnO:Al and 0.5 mA/cm$^2$ for the ITO).

Figure 5.2 shows the $j_{\text{loss}}$ vs. sheet resistance due to absorption of the ≈ 100 nm thick ZnO:Al and ITO layers deposited on glass under the different oxygen concentrations described previously. As expected, both materials present a decrease in the $j_{\text{loss}}$ value when the sheet resistance is increased. It can be observed, that the prepared ITO layers feature better optoelectronical properties than the ZnO:Al samples: for two layers with a similar $R_{\text{sh}}$, the ZnO:Al layer absorbs a larger amount of light than the ITO layers. In particular, in the region near the desired optoelectronical working point of these materials (100–150 Ω/sq) the ZnO:Al layer absorbs an amount of photons equivalent to a current density between 0.6 and 2 mA/cm$^2$, while the ITO absorption stays relatively stable at a value between 0.5 and 0.8 mA/cm$^2$.

### 5.1.2 Transmission Line Measurements

Transmission Line Measurements are useful for obtaining information about the carrier transport properties of a material as well as the quality of the contacts between materials in a

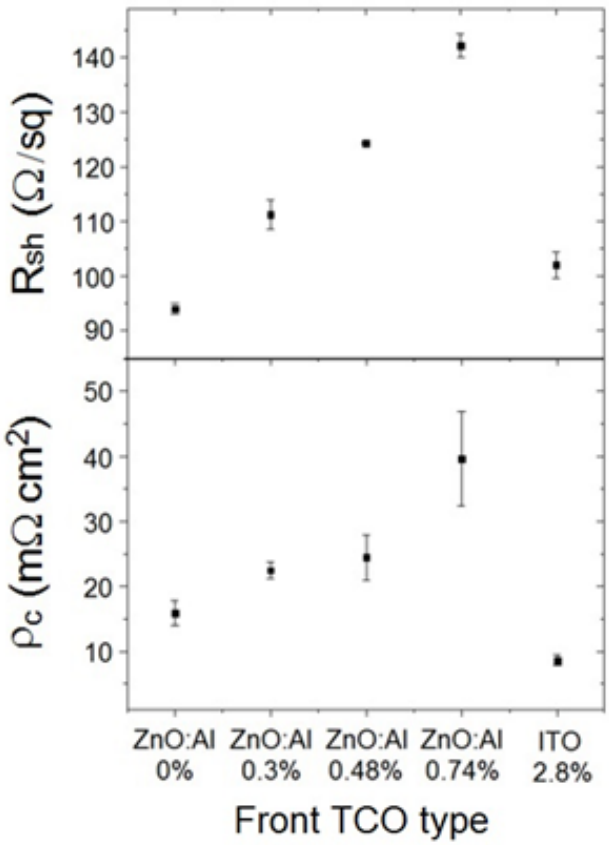


**Figure 5.3:** Contact resistance between TCO und metal grid, $\rho_c$, and sheet resistance, $R_{\mathrm{sh}}$, obtained from TLM measurements on the front side of rear emitter SHJ structures with ITO 2.8% as a reference and ZnO:Al as the front TCO deposited under different oxygen partial flows. Each item on the horizontal axis represents a group of samples, with the material for the front TCO and the oxygen partial pressure under which it was deposited.

layered system. An explanation of the TLM method can be found in Section 3.2.10 and with more details in Luan and Neudeck [97].

The electrical properties of TCO layers implemented in solar cells were investigated using dedicated TLM structures co-processed together with the SHJ solar cells, on the same wafer. Figure 5.3 shows $R_{\mathrm{sh}}$ and the contact resistance $\rho_c$ between the TCO layer and the silver grid. This data was extracted from TLM measurements for the front TCOs used in the SHJ structures with ZnO:Al and ITO, varying the $O_2$ concentration during the sputter-deposition.

The TLM measurements show an increase in $R_{\mathrm{sh}}$ with $O_2$ partial flow for the ZnO:Al front TCOs which correlates with the increasing $R_{\mathrm{sh}}$ values measured on the layers on glass with the 4-point-probe (Fig. 5.1a). It can be observed from Figure 5.3, that $R_{\mathrm{sh}}$ and $\rho_c$ of the ZnO:Al TLM structures are higher than those of the ITO reference. While $R_{\mathrm{sh}}$ of the ZnO:Al is only 5–20% higher than $R_{\mathrm{sh}}$ of the ITO, the contact resistance $\rho_c$ is approximately three times higher. Furthermore, comparing the TCO layers on glass vs. those on the solar cells, the $R_{\mathrm{sh}}$ value of the TLM structures increases from 94 Ω/sq to 142 Ω/sq for ZnO:Al with an

$O_2$ partial flow ratio variation from r($O_2$) = 0% to r($O_2$) = 0.74%, for the ZnO:Al layers on glass it increases from 120 Ω/sq to 226 Ω/sq. This difference can be explained by the lateral current transport through the Si wafer.

The contact resistance, $\rho_c$, of all the ZnO:Al samples with the silver grid is higher than that of the ITO reference sample, increasing from 16 mΩ cm$^2$ to 40 mΩ cm$^2$ for a partial $O_2$ oxygen flow of r($O_2$) = 0% to r($O_2$) = 0.74%. For the ZnO:Al samples deposited under r($O_2$) = 0.3% to r($O_2$) = 0.48% the value is similar (around 23 mΩ cm$^2$), while the sample deposited under r($O_2$) = 0.74% presents a value almost twice as large, and approximately 4 times larger than the $\rho_c$ of the ITO reference.

Taking into account the measured $R_{\mathrm{sh}}$ values of the ZnO:Al layers on glass, and the wafer having a resistivity of approx. 5 Ω cm at 125$\mu$m thickness ($R_{\mathrm{sh,cSi}}$ = 400 Ω/sq), the equivalent sheet resistance of the system can be calculated assuming a simple model of two resistors (the TCO and the c-Si) connected in parallel: $R_{\mathrm{sh,tot}} = [(R_{\mathrm{sh,cSi}})^{-1} + (R_{\mathrm{sh,TCO}})^{-1}]^{-1}$. According to this model, the overall resistance of the system then ranges from 92 Ω for a sample deposited under r($O_2$) = 0% to 144 Ω for a sample deposited under r($O_2$) = 0.74%. Note, that this model neglects TCO/Si contact resistivity and changes in charge carrier density in the c-Si, which occur both upon contact formation and under illumination, i.e. excess charge carrier generation. Interestingly, the calculated values are in good accordance with the $R_{\mathrm{sh}}$ values determined from the TLM measurements. This indicates that the assumption of a negligible TCO/Si contact resistivity is low enough to justify the parallel resistor model as done here. In a solar cell, under operation (e.g. under illumination) the contact resistivity does contribute and has to be investigated in more detail, as was done by Wang et al. [98].

Using the data obtained from the TLM measurements, an estimation of the different contributions of the $R_{\mathrm{s}}$ of the solar cells was made. A direct comparison to the series resistance of the solar cells obtained by contrasting the IV curve with the SunsV$_{oc}$ curve is shown in Table 5.1. This series resistance is calculated following the method by Pysch et al. [85].

| **TCO Variation** | $R_{\mathrm{s}}^{\mathrm{c}}$ [Ω] | $R_{\mathrm{s}}^{\mathrm{TCO}}$ [Ω] | $R_{\mathrm{s}}^{\mathrm{c}} + R_{\mathrm{s}}^{\mathrm{TCO}}$ [Ω] | $R_{\mathrm{s}}^{\mathrm{SunsVoc-IV}}$ [Ω] |
|---|---|---|---|---|
| 0% | 0.5 | 0.3 | 0.8 | 1.1 |
| 0.3% | 0.8 | 0.4 | 1.2 | 1.1 |
| 0.48% | 0.8 | 0.4 | 1.2 | 1.1 |
| 0.74% | 1.3 | 0.5 | 1.8 | 1.2 |
| ITO | 0.3 | 0.4 | 0.7 | 1.0 |

**Table 5.1:** Calculated contact resistance ($R_{\mathrm{s}}^{\mathrm{c}}$), TCO resistance ($R_{\mathrm{s}}^{\mathrm{TCO}}$) and its addition. Series resistance of the cell extracted from SunsV$_{\mathrm{oc}}$ and IV measurements ($R_{\mathrm{s}}^{\mathrm{SunsVoc-IV}}$).

The simple model used for estimating the $R_s$ contributions of the wafer/TCO/silver grid system uses the data extracted from the TLM measurements, and takes into account two main contributions, one due to lateral transport through the TCO to the silver grid, and other due to the contact between TCO and the silver grid (calculated using the $\rho_c$ extracted from the TLM measurements and dividing it through the contact area between the TCO and the silver grid).

Table 5.1 shows the calculated contact resistance ($R_s^c$), TCO resistance ($R_s^{TCO}$), and the sum of those two quantities. The last column shows the $R_s$ measured from the comparison of the $SunsV_{oc}$ and the sun simulator IV curve ($R_s^{SunsVoc-IV}$).

The estimated $R_s$ using a simple model is close to that found when comparing the IV and the $SunsV_{oc}$ measured curves. However, the changes in $R_s^{SunsVoc-IV}$ are less pronounced than $R_s^c + R_s^{TCO}$ expected from the model. It can be observed, that the measured values and the calculated values are very similar for those samples deposited under $r(O_2) = 0.3\%$ and $r(O_2) = 0.48\%$, and deviates more significantly for the samples deposited under $r(O_2) = 0\%$ and $r(O_2) = 0.74\%$, which are the extremes of the oxygen variation. The layer deposited under $r(O_2) = 0\%$ possess both the lowest $R_{sh}$ and the highest absorption (and therefore, smaller $j_{sc}$), while for the layer deposited under $r(O_2) = 0.74\%$ the opposite is true. It is possible, that the combination of these factors (low $R_{sh}$ and low $j_{sc}$ for one of the samples, high $R_{sh}$ and high $j_{sc}$ for the other) accounts for the deviation between the measured and the calculated values for these samples. This is also confirmed by the TLM measurements where it can be seen that the contact resistivity of the layer deposited under $r(O_2) = 0.74\%$ to the silver grid is almost twice the value of those deposited under $r(O_2) = 0.3\%$ and $r(O_2) = 0.48\%$.

Furthermore, it is important to note that the $R_s$ contribution from the lateral transport in the TCO behaves differently than $R_s$ contribution from the TCO/Ag contact resistance: The $R_s$ due to the transport stays almost constant for all the ZnO:Al samples and is similar to that of the ITO reference, while the $R_s$ due to the contact is higher for all the ZnO:Al samples than that of the ITO reference. This result was expected already from the TLM analysis.

For a more accurate analysis of the $R_s$ difference between the measured values and the calculated ones it would be useful to repeat the TLM measurements under illumination, since the conductivity of the system could be different when photocurrent generation is taking place. Under illumination, the photogenerated charge carriers would lower the effective resistivity of the TCO/c-Si stack [96], producing a smaller deviation between the calculated and measured values.

### 5.1.3 Solar cell results

The produced solar cells were characterized with a sun simulator and a EQE system from which the results shown in this section were obtained. This characterization methods, shown in sections 3.2.1 and 2.3 respectively, give us information about the internal working of a solar cell and the loss mechanisms that take place in them.

Figure 5.4 shows the IV parameters for the Bifacial (BF) SHJ solar cells with ZnO:Al and ITO as front TCOs. The TCO on the rear side of all the cells was kept constant, the reference ITO ($r(O_2) = 2.8\%$) was used. With the exception of the ZnO:Al sample deposited under 0% oxygen partial pressure, the solar cells with ZnO:Al front TCO show a slightly higher $j_{sc}$ compared to those of the ITO reference cells. The $j_{sc}$ of these solar cells increases with increasing $O_2$ partial flow. The fill factors of all ZnO:Al samples are lower than that of the ITO sample, and they show a decreasing trend with increasing $O_2$ partial flow ($r(O_2) = 0...0.74\%$). This result agrees qualitatively with the increase of the $R_{sh}$ value of ZnO:Al layers deposited under an increasing oxygen ratio in the process gas. The average FF of the ITO BF samples (78.4%), is higher than those of the ZnO:Al solar cells. This is the main reason for the better performance of the ITO solar cells, since their $j_{sc}$ and Voc are in the same range as those of the ZnO:Al solar cells, excluding the ZnO:Al solar cell deposited under 0% oxygen flow, which presents both a lower $j_{sc}$ and Voc than all other samples. The $V_{oc}$ of all these cells is very similar and in the range of approx. 728 mV.

The smaller FF of the ZnO:Al solar cells is explained in the section 3.3 in terms of a higher value of the series resistance of the solar cells, measured using the TLM structures.

Figure 5.5 shows the EQE measurements of the solar cells with the highest power conversion efficiency of three groups: a BF ITO cell, and a BF and a MF ZnO:Al solar cell both deposited under $r(O_2) = 0.3\%$, as well as $1 - R_{tot}$, the fraction of non-reflected light from the UV-VIS measurements.

The Monofacial (MF) ZnO:Al solar cell has a higher EQE for long wavelengths, mainly due to the silver back contact, which reflects a fraction of the light back into the solar cell. In case of the BF solar cells a fraction of light is transmitted, lowering the $j_{sc}$.

The EQE response of both BF cells could suggest, that the ITO cell performs worse than the ZnO:Al cell in the short wavelength region. Nevertheless, when analyzed in detail, it can be seen, that the reflection minimum is different for ITO and ZnO:Al, which could be

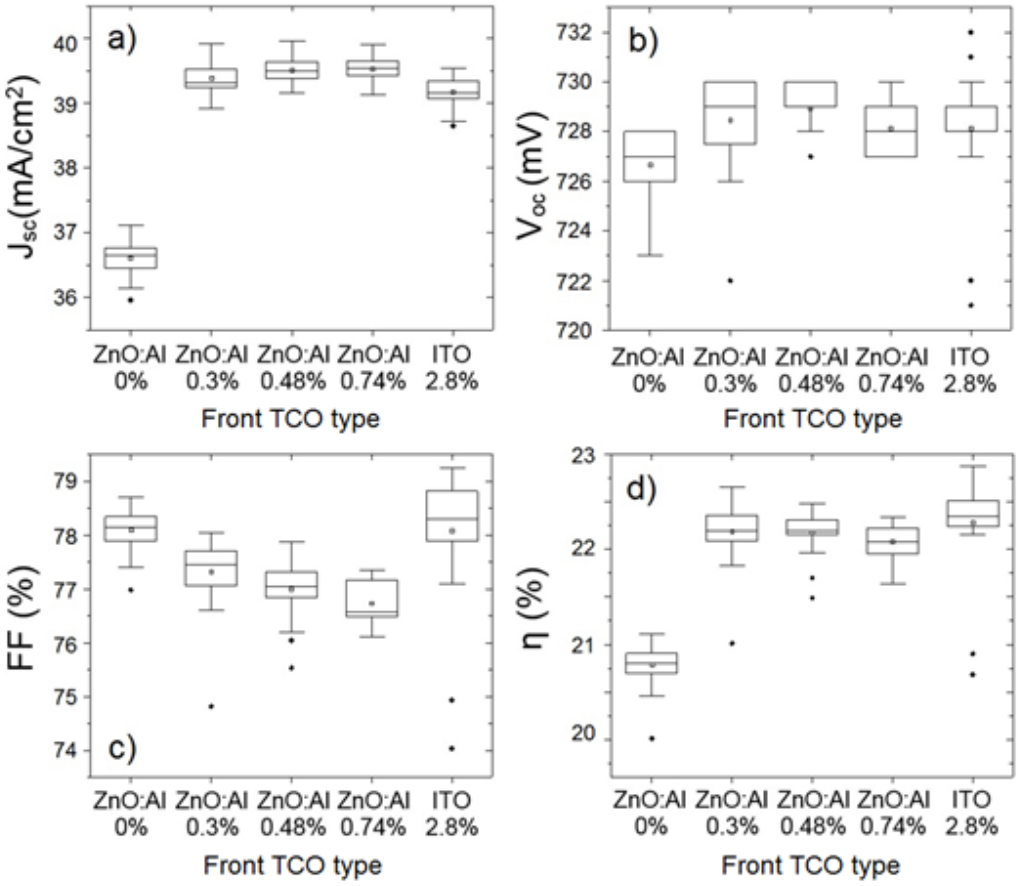


**Figure 5.4:** Solar cell results of SHJ cells with ZnO:Al and ITO as a front TCO. a)$j_{sc}$, b)$V_{oc}$, c)FF and d)power conversion efficiency, $\eta$, for the Bifacial (BF) ZnO:Al solar cells and the ITO reference. The box plots represent the statistics of the measurements made on the 2 wafers with 14 cells each. The horizontal axis of each graph shows the material used in that group as a front TCO and the partial oxygen flow under which this material was deposited.

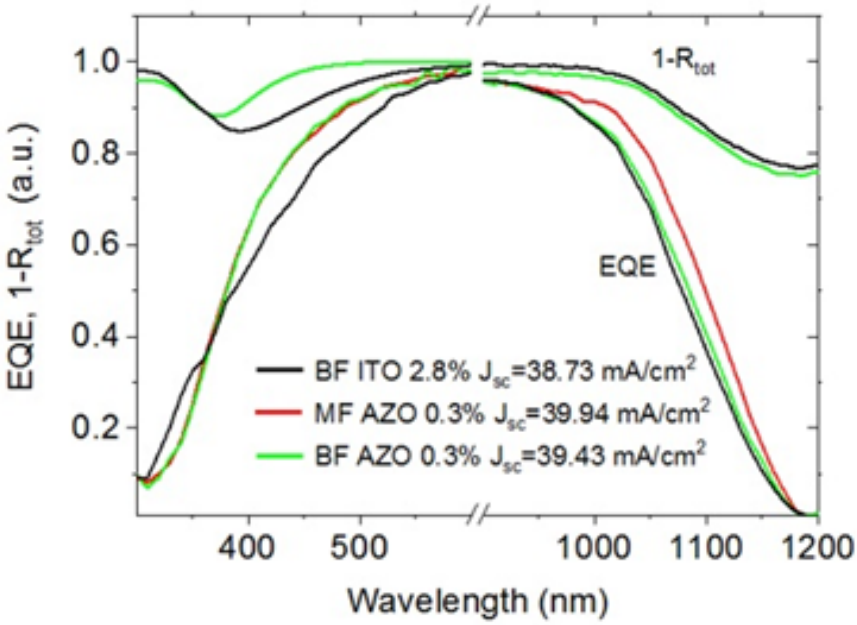


**Figure 5.5:** External quantum efficiency (EQE) and $1 - R_{\text{tot}}$ vs. wavelength of the solar cells with the highest power conversion efficiency of three groups. Monofacial (MF) and Bifacial (BF) ZnO:Al solar cells (red and green lines, respectively) compared to a BF ITO reference solar cell (black line). For the $1 - R_{\text{tot}}$ spectra, only one of the ZnO:Al curves is shown, since there is no difference between the MF and the BF cell on the UV-VIS reflection measurement of the front side.

caused by a thickness deviation of the ITO layer. The $j_{\text{sc}}$ of the EQE measurements agrees qualitatively with the IV measurements.

### 5.1.4 Chapter Summary

It was proposed by Bivour et al. [21] that, when using the rear emitter configuration, a TCO layer with slightly worse optical and electronical properties than those of indium doped tin oxide could be used achieving a similar performance, and for this reason, aluminium doped zinc oxide was investigated as an indium-free TCO for SHJ solar cells in the rear emitter configuration.

Using magnetron sputtering, ITO and ZnO:Al layers were prepared and characterized, undertaking a variation of the oxygen content present during the sputtering deposition in order to achieve a variation of the optoelectronical properties of the ZnO:Al layers. Rear emitter SHJ solar cells were prepared and characterized achieving a high power conversion efficiency well above 22% for both solar cells using ITO and ZnO:Al as a TCO layer, nevertheless, the ZnO:Al layers showed a 0.2% lower efficiency than the ITO ones, which was due to a lower FF.

Using the standard characterization techniques (IV curve, EQE, TLM measurements) these two types of cells were compared in order to find the reason of the underperformance of the ZnO:Al solar cells. As the sheet resitance of all ZnO:Al layers is in a relatively narrow range of 100–140 Ω for all oxygen flow ratios (compare Figure 5.3), with ITO being in the same range, we concluded that the contact resistance between the ZnO:Al and the silver grid is more relevant. It was found to be approximately twice as high as that of the ITO/silver grid system, and with TLM mesurements it was possible to identify this factor as being one of the responsibles for the slight underperformance of the ZnO:Al cells. Looking to improve the contact resistance between these two materials could lead to the fabrication of indium-free SHJ solar cells with a higher PCE. An additional contribution to the series resistance leading to the lower FF of the ZnO:Al based cells could be a higher (n)Si/ZnO:Al contact resistance as compared to the (n)Si/ITO contact. This, however, is beyond the scope of this thesis and needs to be investigated in future work.

# 6

# Optoelectronic properties of electron-beam evaporated NiOx

Nickel Oxide is an interesting material for application in photovoltaic materials and in general in the semiconductor industry since it has been shown, that it is intrinsically p-doped, which is an important difference to most of the semiconductors often used for producing contact layers, such as ZnO:Al and ITO which are n-doped. This property of the NiOx layers together with its large optical bandgap of around 3.6–3.8 eV would make it suitable for a contact layer on the p-side of a pn junction which could act either as a TCO or as a charge selective contact for holes, while blocking electrons.

Until now, NiOx has been used in many applications such as UV photodetectors, electrochromic devices [50, 99] or solar cell electrodes [100], and thin layers have been produced using different methods such as sputtering [101], non-reactive e-beam deposition [102], and thermal evaporation of NiOx powder [103]. This has been discussed in more detail in section 2.12.

The results shown in the following section consist of a material characterization and the effects found when depositing this material by means of reactive e-beam evaporation on top of passivated silicon wafers. The passivation was done using a-Si:H thin films fabricated in one of the PECVD chambers of the Energy Materials In-situ Laboratory (EMIL) cluster using $SiH_4$ and $H_2$ as precursor gases.

The e-beam evaporation technique is explained in Section 3.1.2 and all depositions were performed in a UNIVEX450 system from Leybold vacuum products.

## 6.1 Layers on glass / oxygen content variation

The physical characteristics of the e-beam-evaporated nickel layers, deposited on glass substrates under different oxygen pressures are shown in this section. It is important to note, that it is assumed that the oxygen pressure is identical to the chamber pressure during the deposition, i.e. it is assumed that oxygen is the main gas in the chamber. This is reached after achieving a vacuum of approx. $4 \times 10^{-7}$ mbar and then introducing oxygen by means of a valve into the chamber until the pressure value under which the e-beam deposition takes place, is achieved.

The measured data from the Hg probe and the Hall resistivity measurements possess a very small uncertainty value due to the high accuracy of the measurement technique. The error bars of these measurements can not be seen, because they lie inside the dot presented in the graph. The graphs show, nevertheless, the general behaviour of the optoelectronic properties of the thin layers on glass for the oxygen variation.

### 6.1.1 Resistivity measured with a mercury probe

Figure 6.1 shows the variation of the resistivity of 110 nm thick NiOx layers as measured with the Hg probe (cf section 3.2.12), deposited under different oxygen pressures. These values are found when the deposition is undertaken in an atmosphere with an oxygen partial pressure between $4 \times 10^{-7}$ mbar and $1 \times 10^{-4}$ mbar. These values represent the maximum range in which a NiOx deposition is possible in the e-beam evaporation system UNIVEX 450. The lowest pressure value ($4 \times 10^{-7}$ mbar) corresponds to the lowest pressure achieved by the vacuum pump of the system, and the highest achievable pressure value ($10^{-4}$ mbar) that can be used for depositing a sample for which the electronic properties can be measured. At deposition pressures higher than $10^{-4}$ mbar, the samples possess such a high resistivity that this and other electronic properties such as Hall mobility and charge carrier concentration cannot be successfully measured with the Hg probe. It is also important to note that at pressure values higher than $10^{-3}$ mbar, the high voltage between anode and cathode of the system is not always stable, and for this reason it is not always possible to produce a stable electron beam.

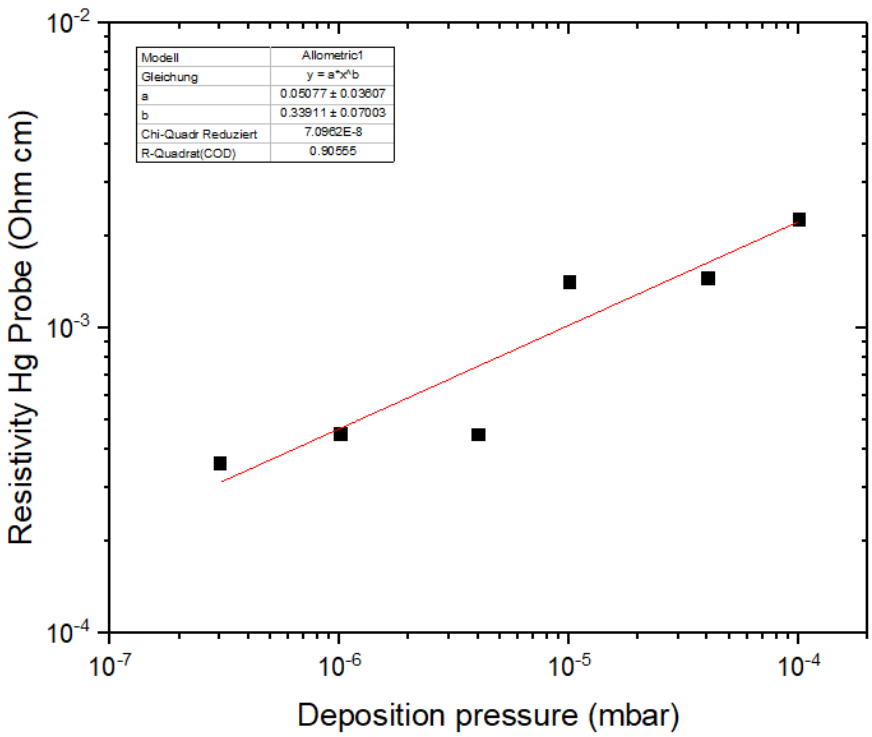


**Figure 6.1:** Resistivity of 110 nm thick NiOx layers, deposited under different oxygen pressures, as measured with the Hg probe. The error bars are of the same order of magnitude as the size of the dots.

For a 110 nm thick nickel sample measured with the profilometer, deposited at the lowest achievable system pressure ($4 \times 10^{-7}$ mbar), a resistivity of 0.3 mΩ cm was measured. The resistivities of the nickel layers increase as the oxygen pressure under which they were deposited increases. The resistivity increases until a value of approx. 2.3 mΩ cm is found for a layer deposited under an oxygen pressure of $10^{-4}$ mbar.

The measured data from the Hg probe and the Hall resistivity measurements possess a very small uncertainty value due to the high accuracy of the measurement technique. The error bars of these measurements can not be seen, because they lie inside the dot presented in the graph. The graphs show, nevertheless, the general behaviour of the optoelectronic properties of the thin layers on glass for the oxygen variation.

The first 3 points, deposited under oxygen pressures of $4 \times 10^{-7}$ mbar, $1 \times 10^{-6}$ mbar and $4 \times 10^{-6}$ mbar, show almost no change in their resistivity, staying at a value of 6–8$\times 10^{-5}$ Ω cm. For values higher than $1 \times 10^{-5}$ mbar, the resistivity shows an increase until reaching the highest measurable resistivity value of $4 \times 10^{-4}$ Ω cm. A fit on the data (see figure 6.1) shows that the change in resistivity follows a power law dependence with the oxygen partial pressure during the deposition.

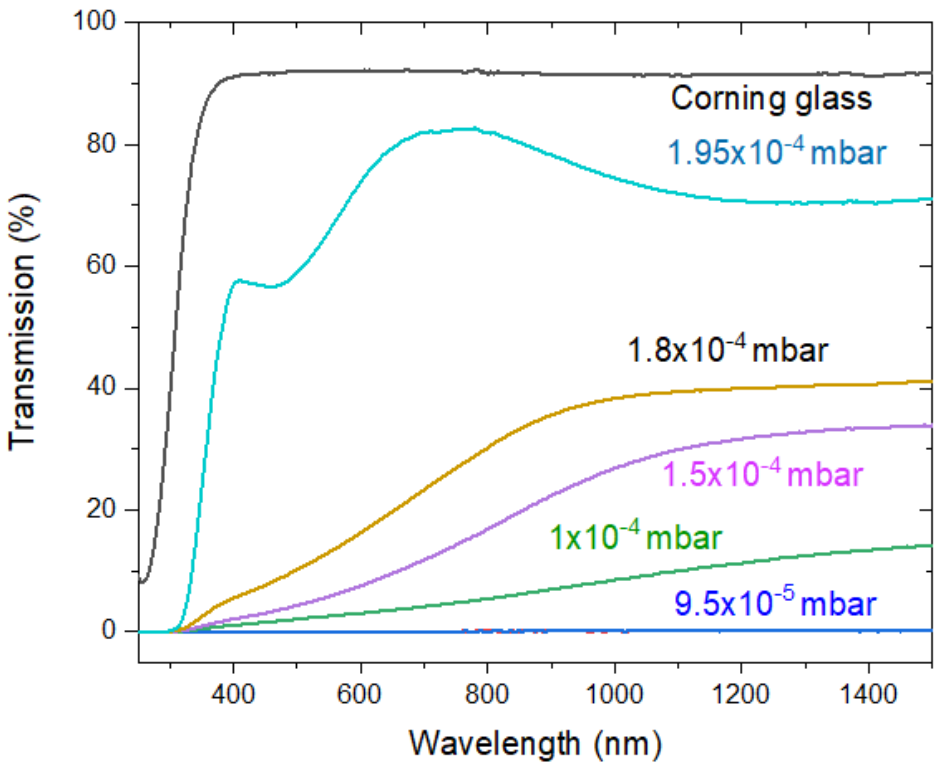


**Figure 6.2:** Optical transmission of 110 nm thick NiOx samples deposited on glass at different oxygen deposition pressures. A Corning glass reference is also shown with a higher transmission for all wavelengths; notably for lower wavelenghts, its transmission is still about ten percent. A trend can be seen in which the transmittance of the layers increases for higher oxygen deposition pressures. The most transparent sample shows a transmission of only 80% at its highest value. Layers deposited at $9.5 \times 10^{-5}$ mbar and lower pressures show no transmission. Layers deposited at higher pressures than $1.95 \times 10^{-4}$ mbar show the same amount of transmission as this layer.

### 6.1.2 UV-VIS measurements

The optical transmission of the layers on glass as measured with UV-VIS spectrometry (see Section 3.2.2) is shown in Figures 6.2 and 6.4.

In Figure 6.2, the transmission spectra of 110 nm NiOx layers on glass can be observed. The five samples represented in this graph are the layers deposited under $9.5 \times 10^{-5}$ mbar, $1 \times 10^{-4}$ mbar, $1.5 \times 10^{-4}$ mbar, $1.8 \times 10^{-4}$ mbar and $1.95 \times 10^{-4}$ mbar oxygen pressures.

These pressure values were chosen after finding that layers deposited under an oxygen pressure of $9.5 \times 10^{-5}$ mbar showed practically no transmission, and layers deposited above $1.95 \times 10^{-4}$ mbar achieved the highest transmission for NiOx layers. As stated before, trying to deposit NiOx layers at oxygen pressure values above $1 \times 10^{-3}$ mbar cannot always be done in a stable evaporation process due to the instability of the electron beam.

The transmission spectra of the layers in Figure 6.2 show, in other words, the pressure range in which the optical properties of the NiOx layers show a variation, going from completely

opaque to partially transparent. This is the range in which we are interested for using the NiOx layers as a TCO.

It can be seen that the optical transmission of these layers increases when the amount of oxygen present during the deposition also increases. This behaviour is also observed in the previous section, where ZnO:Al and ITO layers were studied. Nevertheless, the only sample that shows transmission values over 50% is that deposited under the highest oxygen pressure value of $1.95 \times 10^{-4}$ mbar, discarding the other layers as possible materials for the elaboration of a transparent conductive film with antireflection properties. Taking into account the optoelectronical properties of the as deposited samples (i.e. before any kind of treatment to improve them is undertaken), their exclusion as a possible TCO can be decided without further analysis, since a layer absorbing more than 50% of the available photons placed in front of a solar cell made out of a silicon wafer would result in a photovoltaic device with a very low $I_{\mathrm{SC}}$, of approximately $20\,\mathrm{mA/cm^2}$. This value is less than half of the maximum potential value that a silicon solar cell could achieve, and such a solar cell would not even be close to the power conversion efficiency values achieved by conventional solar cells.

This leaves only one of the layers as a possible candidate to be used as a TCO: the layer deposited under an oxygen pressure of $1.95 \times 10^{-4}$ mbar, which is the only one to show a transmission spectrum in the normal level of a TCO, at around 60% to 80% transmission. This value is higher than some values found in the literature for thermal evaporation of nickel oxide [104], but also lower than the transmission of standard ITO and ZnO:Al, which lies between 80% and 95% [11].

The reflection, absorption and transmission spectra of that sample are shown in Figure 6.3. From the transmission spectrum it can be seen, that the transmission of the sample decreases from 250 to 500 nm and stays low for wavelengths larger than 500 nm, this might indicate, that the NiOx prepared by ebeam evaporation in a reactive process is not a degenerated TCO since no free charge carrier absorption can be seen for long wavelengths.

The optical bandgap of the layer deposited under an oxygen pressure of $1.95 \times 10^{-4}$ mbar was analysed by means of a Tauc plot (see Section 3.2.2) with $r = 1/2$ for direct allowed transitions (Figure 6.4) and it was found to be $\approx 3.34$ eV, which is similar although slightly smaller than the value found in other studies (see for example Jlassi et al. [44] and Raut et al. [43]).

If the UV-VIS spectrum of the sample deposited under an oxygen pressure of $1.95 \times 10^{-4}$ mbar is multiplied by the AM 1.5 solar spectrum, it is found that the amount of

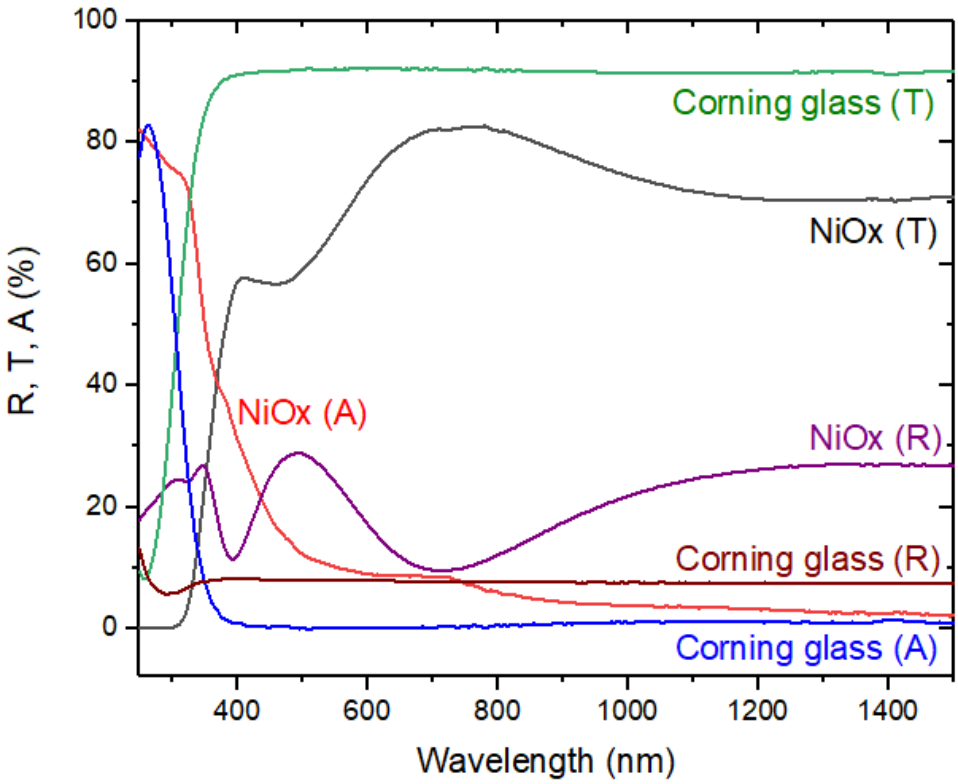


**Figure 6.3:** Reflection, absorption, and transmission spectra of the 110 nm NiOx layer deposited under $1.95 \times 10^{-4}$ mbar and of a glass reference. This is the layer with the highest transmittance.No free carrier absorption can be seen at longer wavelengths, so this material is likely a non-degenerate semiconductor.

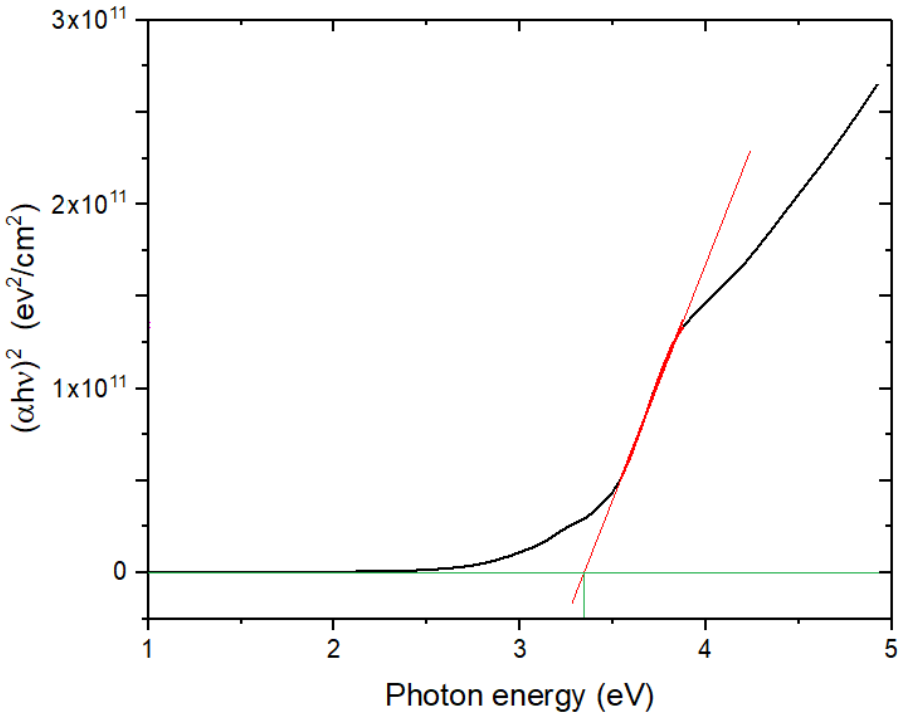


**Figure 6.4:** Tauc plot of the layer deposited under an oxygen pressure of $1.95 \times 10^{-4}$ mbar. A bandgap of 3.34 eV was determined.

photons absorbed by this layer in the photon wavelength range that can be absorbed by a silicon solar cell with bandgap of 1.1 eV, is approximately 4 times higher than that of the ITO and ZnO:Al samples presented earlier in this thesis. The number of transmitted photons by this layer is thus relatively low, accounting for only (when converted to an electrical current, and assuming an IQE of 100% and no recombination losses) a maximum possible $I_{SC}$ of $33.4\,\mathrm{mA/cm^2}$, which is a low value when compared to usual solar cells like the ones produced in the last section.

These facts make it possible for us to discard the 110 nm thick NiOx layer deposited under an oxygen pressure of $1.95 \times 10^{-4}$ mbar as a possible TCO for solar cells.

### 6.1.3 Hall mobility measurements

Hall measurements were made in van der Pauw geometry, which uses four contacts, one pair for measuring voltage and the other pair for measuring current (see Section 3.2.11).

Their Hall resistivity, charge carrier concentration and Hall mobility were measured in order to have a more complete material study. These properties are shown in Figures 6.5 and 6.6.

Figure 6.5 shows resistivity values of the NiOx samples as measured with the Hall measurement system HMS Ecopia 3000 (squares and triangles) and compared to the resistivity values measured with the Hg probe (circles). The resistivity values show a variation from $1{\times}10^{-5}\ \Omega\,\mathrm{cm}$ to $1{\times}10^{-3}\ \Omega\,\mathrm{cm}$ when the deposition pressure changes from $4 \times 10^{-7}$ mbar to $1 \times 10^{-4}$ mbar. It can be seen that the critical value for which the change in resistivity starts to appear is approx. at $1 \times 10^{-5}$ mbar.

A difference between the data measured with the mercury probe and the Hall measurement system can be seen. Since the Hall measurement system is calibrated with an ITO reference before every measurement it could be considered that this technique is more reliable than the mercury probe, which was not calibrated. Another reason for the higher resistivity values measured with the mercury probe could be the sample size. For the mercury probe measurement a 1 sq in glass is used, while the Hall measurement is done on a smaller, $0,25\ cm^2$ glass taken from the center of the 1 sq in glass. This might lead to a greater homogeneity of the film on which the Hall measurement is made.

Figure 6.6 shows the variation of the charge carrier concentration (squares) and the Hall mobility (triangles) of the layers on glass as measured with the Hall measurement system (HMS 3000 Ecopia) of samples deposited under an oxygen pressure ranging from $4 \times 10^{-7}$ mbar

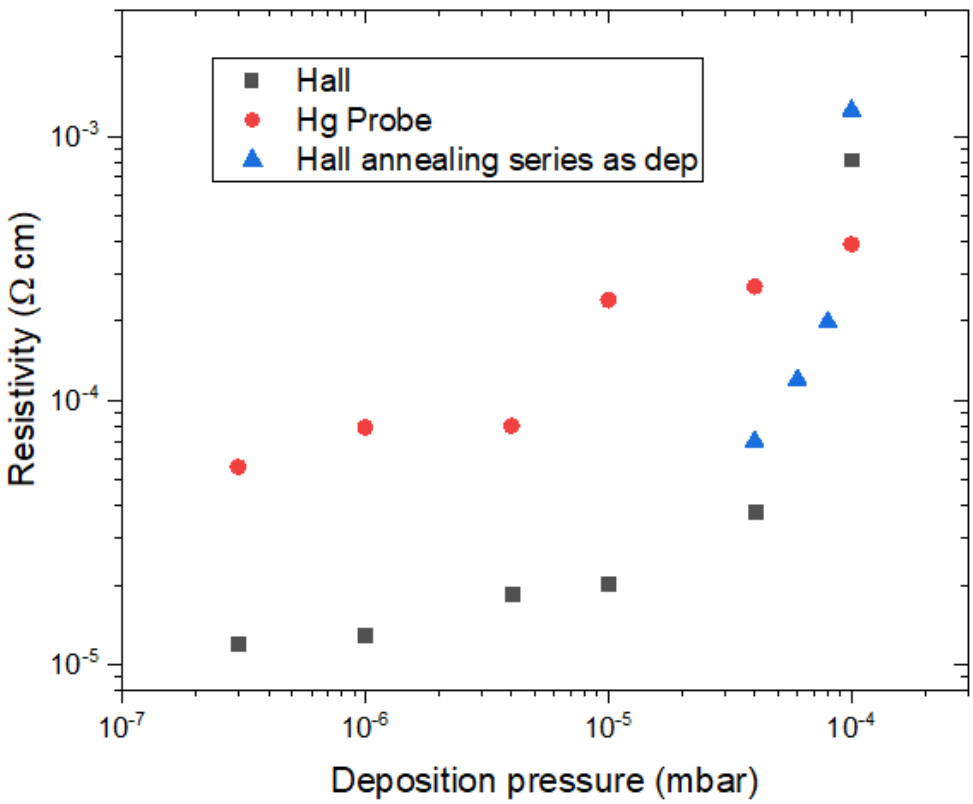


**Figure 6.5:** Hall resistivity of the NiOx samples as measured with the Hall measurement system HMS 3000 Ecopia (squares and triangles) and compared to the resistivities measured with the Hg Probe (circles). For layers deposited at higher oxygen deposition pressures the values could not be measured due to a very high resistivity.

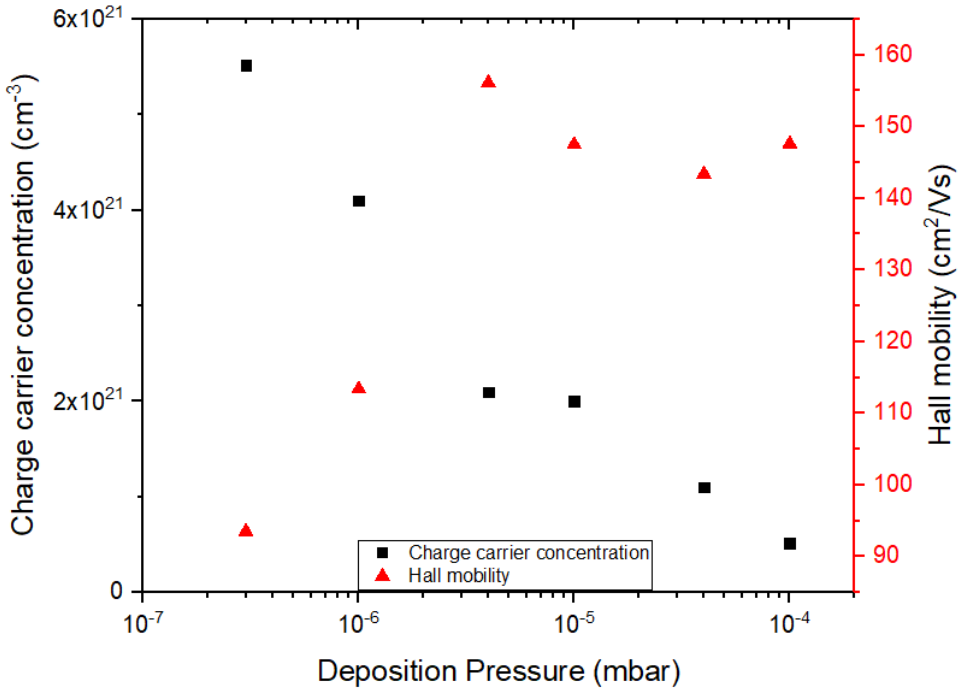


**Figure 6.6:** Charge carrier concentration (squares) and Hall mobility (triangles) of the NiOx samples as measured with the Hall measurement system HMS 3000 Ecopia. The highest value is found for the most metallic sample and decreases for more oxidic samples. For layers deposited at higher oxygen deposition pressures the values could not be measured due to a very high resistivity.

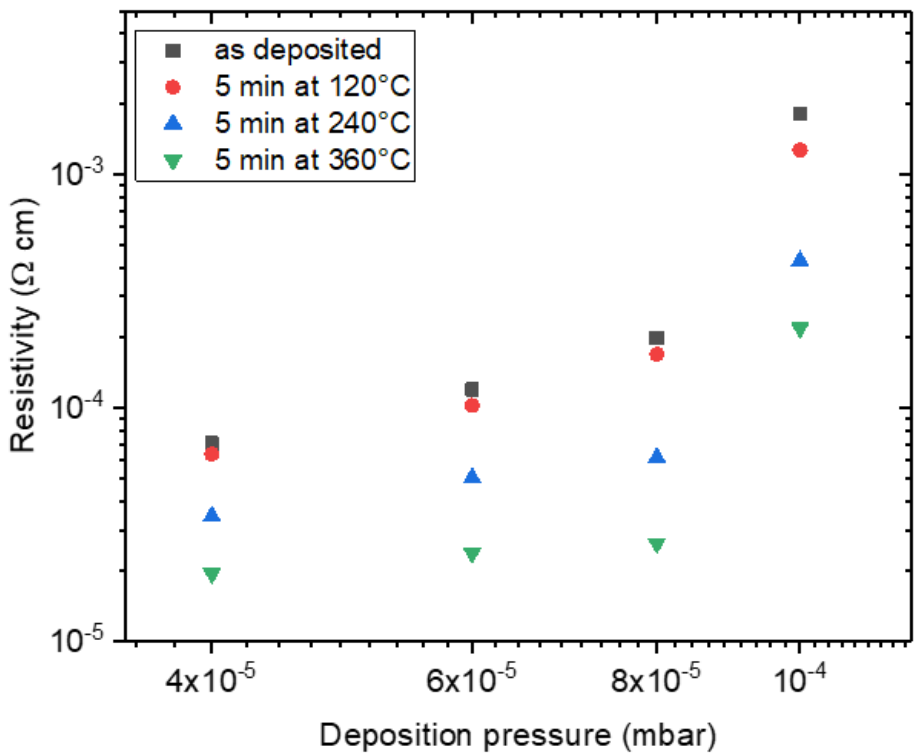


**Figure 6.7:** Resistivity of the NiOx samples after annealing steps as measured with the Hall effect system HMS 3000 Ecopia. Layers deposited at higher oxygen pressures could not be measured due to a very high resistivity

to $1 \times 10^{-4}$ mbar. The highest value is found for the sample deposited without an oxygen atmosphere and decreases for samples deposited under higher oxygen pressures. The charge carrier concentration of these samples decreases from $5.5 \times 10^{21}$ to $5 \times 10^{20}$ cm$^{-3}$ when the deposition pressure increases along the aforementioned range. This result agrees with the idea that layers deposited under a higher oxygen pressure have a less metallic behaviour due to the fact, that atoms of the metal are forming a bond with oxygen atoms and are not free to react to an electric field anymore.

The Hall mobility of the layers shows a variation when the deposition pressure increases from $4 \times 10^{-7}$ mbar to $1 \times 10^{-4}$ mbar, as seen in Figure 6.6. Starting at a mobility of 93 cm$^2$/Vs for an oxygen deposition pressure of $4 \times 10^{-7}$ mbar and increasing to a value of 156 cm$^2$/Vs for an oxygen deposition pressure of $4 \times 10^{-6}$ mbar, increasing the deposition pressure above this value lowers the Hall mobility of the samples to a value of 147 cm$^2$/Vs for a layer deposited under $1 \times 10^{-4}$ mbar.

In order to analyse if an annealing treatment produces a reduction in the resistivity of the NiOx layers, a sequential set of annealing processes (in air) was undertaken for 110 nm thick samples deposited under oxygen pressures of $4 \times 10^{-5}$, $6 \times 10^{-5}$, $8 \times 10^{-5}$ and $1 \times 10^{-4}$ mbar.

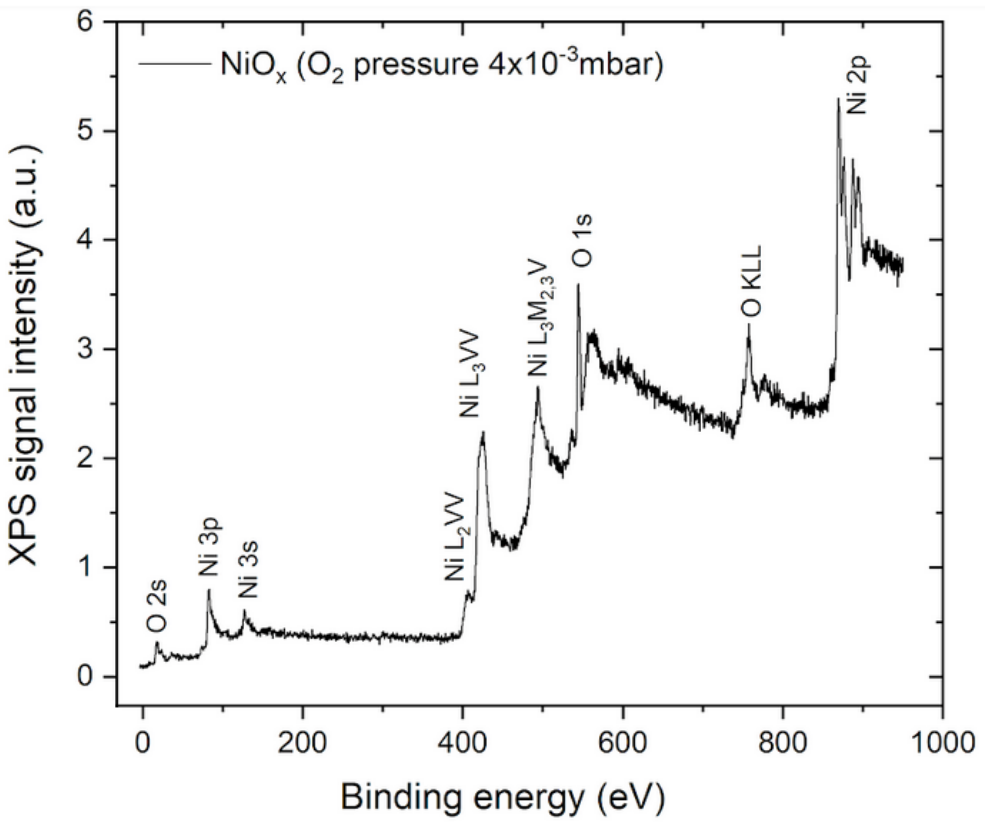


**Figure 6.8:** Survey XPS spectrum of a NiOx layer deposited under showing only nickel and oxygen core level signals. The $O_{1s}$ and $Ni_{2p}$ core levels were analysed in detail to investigate the composition of the films.

These measurements can be seen in Figure 6.7. In general, it can be said that the resistivity of these samples decreases by about one order of magnitude if they are annealed at successively temperatures of 120 °C, 240 °C and 360 °C for 5 minutes. The annealing treatments can not be considered as the only factor having an effect in the resistivity of the layers since additional oxidation of the samples during the process could have an influence in their physical properties. Samples deposited under higher oxygen pressures, could not be measured, since their resistivity lies outside the measurement range of the Hall measurement system and the annealing steps have a detrimental effect on the structural properties of the layers, which start turning into a powder-like material which falls off the glass substrates in flakes.

## 6.2 XPS measurements

In order to investigate the chemical composition of the thin films, XPS measurements were performed (see details in Section 3.2.5).

Figure 6.8 shows an example of an XPS survey spectrum of the layer deposited under the highest oxygen pressure, $4 \times 10^{-3}$ mbar . The core levels of nickel and oxygen as well as the

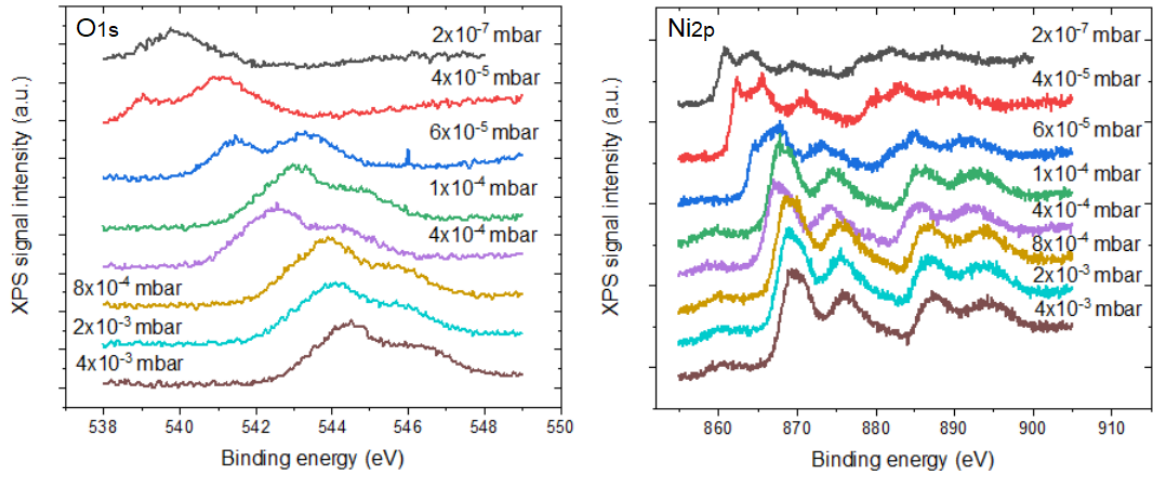


**Figure 6.9:** XPS spectra of the NiOx layers on glass. The signals of the orbitals $O_{1s}$ (*left*) and $Ni_{2p}$ (*right*) are shown for a variation of the oxygen deposition pressure. Spectra are offset along the ordinate for better visibility.

respective Auger signals are indicated. As can be seen from the survey spectrum, no XPS signal (above the detection limit of XPS) belonging to other species than nickel and oxygen is present.

For further analysis, the $O_{1s}$ and $Ni_{2p}$ XPS detail spectra of the NiOx layers, deposited under increasing oxygen pressures are recorded. The raw data is shown in Figure 6.9. It can be seen that both core levels, $O_{1s}$ and $Ni_{2p}$ shift along the binding energy up to 6.8 eV towards higher binding energy, for an increasing oxygen pressure. Such a shift is possible due to different reasons: a change in the chemical state of the materials, a change in the Fermi level position relative to the band edges or electrostatic charging of the sample during the measurement. Since the layers were deposited directly on a glass substrate without any additional conductive layer, it is likely that a charging effect is present. As we have seen above, the resistivity of the samples increases with increasing oxygen deposition pressure, which can be correlated to the more pronounced shift for those layers. The exact shift of the XPS measurements, relative to literature reference positions is quantified in Figures 6.11 and 6.12. Note, that this does not affect the peak area or the peak position of the core levels relative to each other.

A change in the peak composition of the XPS signals can be clearly observed, especially for $O_{1s}$, which changes gradually from a single to a double peak. For the sample deposited at oxygen pressures of up to $6 \times 10^{-5}$ mbar, the O-Ni signal, located at lower binding energies, shows a lower intensity than the O-C signal, which is located at higher binding energies. This is analysed in detail by doing a fitting of the XPS signal, later in this section.

For samples deposited at higher oxygen pressures than $6 \times 10^{-5}$ mbar, the relation between the O-Ni signal shows a higher intensity than the O-C signal. This already indicates a higher content of NiOx in the samples deposited at higher oxygen pressures, as expected.

For the $Ni_{2p}$ the XPS spectra range from a spectrum similar to that of pure nickel as reported by Grunthaner et al. [105] to that of NiOx reported by Mansour [92]. The three layers deposited at the three lowest deposition pressures show a mixture of metallic nickel and nickel oxide, as it can be seen by the appearance of an additional shoulder on the lower binding energy side of the spectrum, which corresponds to the XPS signal of metallic nickel [105]. For higher deposition pressures this shoulder vanishes, which indicates more oxidic layer compositions. This will also be analyzed quantitatively in the following figures.

These results show, that NiOx was successfully deposited on glass substrates using e-beam evaporation in a reactive process evaporating nickel from pure nickel pellets in an atmosphere containing different amounts of oxygen.

In order to analyse the data in more detail the core level spectra were fitted using the following models adapted from the fitting models of Grunthaner et al. [105] and Mansour [92].

The oxygen signal $O_{1s}$ shown in Figure 6.11 was fitted with a model consisting of two single peaks corresponding to the oxygen bound to either carbon (O-C) or nickel (O-Ni) as already mentioned above. A linear background was assumed since the peak structure of the $O_{1s}$ is much more simple to model in this special case. The expected positions of those peaks are 531.1 eV and 529.1 eV, respectively [92]. Therefore, the distance between the peaks relative to each other was fixed at 2 eV. The FWHMs of the peaks were free fitting parameters. The O-Ni peak showed a similar FWHM after fitting for all samples of $1.7 \pm 0.2$ eV . The variation of the FWHM of the O-C peak is larger, most probably due to the fact that different surface contaminations might be present.

The model consists of five peaks (Figure 6.10) which correspond to metallic Nickel (Ni), Nickel Oxide (NiOx), Nickel Hydroxide ($Ni(OH)_2$) and two shakeup features resulting from ionized nickel atoms. A Shirley background was applied [92]. The distances between the peaks were fixed for each spectrum. The binding energy difference between the peaks was determined from their expected peak positions found in the aforementioned literature (see Table 6.1).

The FWHM for the metallic nickel peak was a free fit parameter for all samples and resulted in a value of $1.6 \pm 0.1$ eV. For the NiO and the $Ni(OH)_2$ peaks, the ratio between their respective FWHMs was set to 1.25, as suggested by Mansour [92]. The FWHM ratios for those peaks stayed similar across all samples. This indicates that the applied model contains

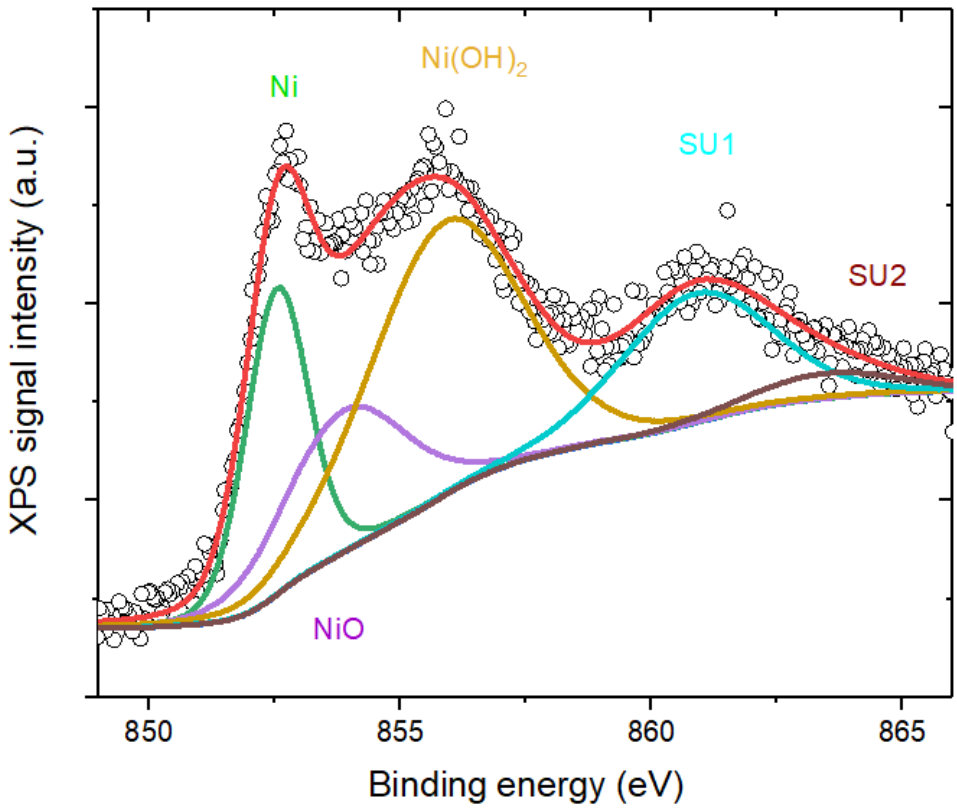


**Figure 6.10:** Example of an XPS fit of the $Ni_{2p}$ core level (red) showing the experimental data (open circles) and the components used, metallic nickel (green), nickel oxide (purple), nickel hydroxide (yellow) and also 2 shake up structures, SU1 (blue) and SU2 (maroon). A Shirley background was used as was found in [92]. The expected position of these peaks can be found in table 6.1

**Table 6.1:** Components of the XPS fit model for the $Ni_{2p}$ core level

| **Peak** | **Expected Position [reference]** | **$\Delta E$ relative to $Ni(OH)_2$** |
|---|---|---|
| Ni | 852.6 eV [105] | 3.6 eV |
| NiO | 854.1 eV [92] | 2.1 eV |
| $Ni(OH)_2$ | 856.2 eV [92] | 0 eV |
| Shake-up 1 | 861.2 eV [92] | 5 eV |
| Shake-up 2 | 863.8 eV [92] | 7.6 eV |

all components and no additional signal needs to be added to the fitting model. The FWHM of the shakeup peaks was a free fit parameter.

In the following, the relative peak areas, extracted from the fitting of the whole oxygen variation series are discussed in more detail, first the $O_{1s}$ and then the $Ni_{2p}$ core level. In order to focus on the relative peak area, the spectra of the different samples were shifted horizontally such that the same peak component appears always at the same binding energy position. The O-Ni and the $Ni(OH)_2$ position were used as arbitrary references for the alignment of the signals, and fixed to their expected values at 530.1 eV and 856.2 eV, respectively. The area of the single peaks is the information needed in order to determine the presence and relative amount of nickel oxide and metallic nickel in the layers.

As a representation of the evolution of the peak structure, the fitted spectra of the four samples, deposited at the lowest oxygen pressures are shown for $O_{1s}$ and $Ni_{2p}$ in Figures 6.11 and 6.12, respectively. For higher deposition pressures, the spectra do not differ significantly from the sample deposited at $10^{-4}$ mbar, which is why they are not shown in detail here.

As it can be seen in Figure 6.11 the $O_{1s}$ detail spectrum for the sample, deposited at $2 \times 10^{-7}$ mbar, was unfortunately not measured far enough to observe the possibly existing signal of O-Ni at around 531 eV. The fact that the background slope has a different sign than that of the other samples indicates that indeed O-Ni bonds might exist. Nevertheless, since this sample is deposited without oxygen during the deposition it can be supposed that the O-Ni signal comes only from surface oxidation. For this sample a relative area fraction of O-C to O-Ni between 0% and 17%, which is the O-Ni fraction of the sample with the next higher deposition pressure, could be expected.

The relative peak areas, resulting from the fitted $O_{1s}$ spectra are shown in Figure 6.13 (*left*). It can be observed, that the relative peak area of the O-Ni increases from 17% at $4 \times 10^{-5}$ mbar to 75% at $1 \times 10^{-4}$ mbar and stays almost constant for higher deposition pressure. If a roughly constant amount of surface contamination is assumed, this implies that the total amount of

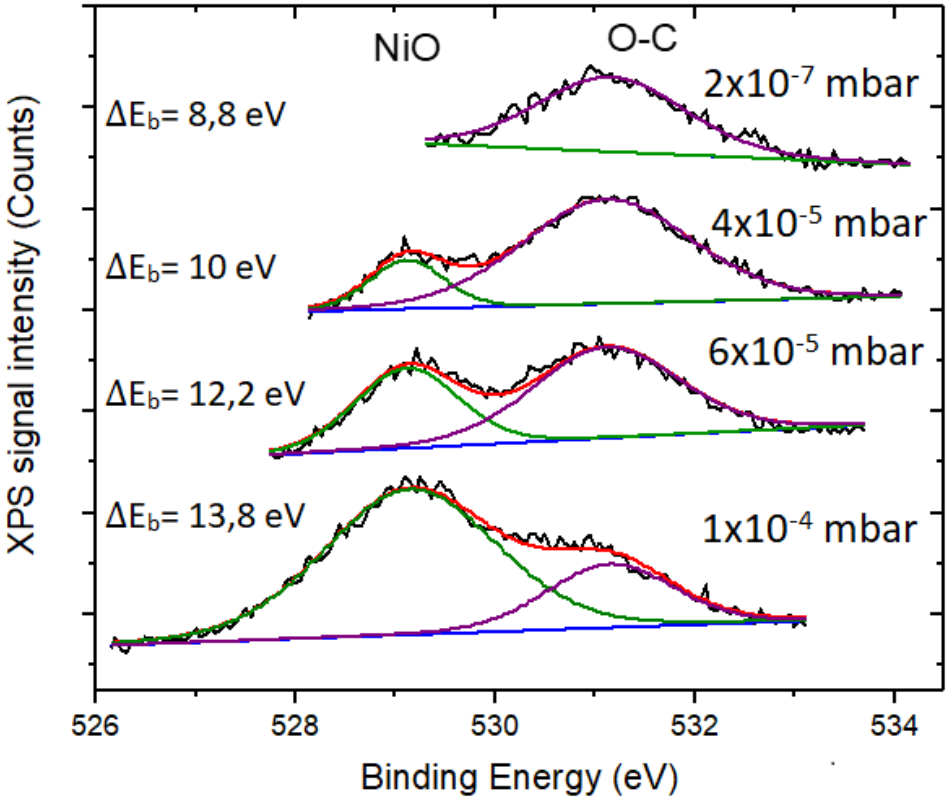


**Figure 6.11:** $O_{1s}$ spectra of NiOx samples deposited at different oxygen pressures. The spectra were shifted so that the XPS peak from the O−C bond appears always at 530.1 eV as measured by Mansour [92].

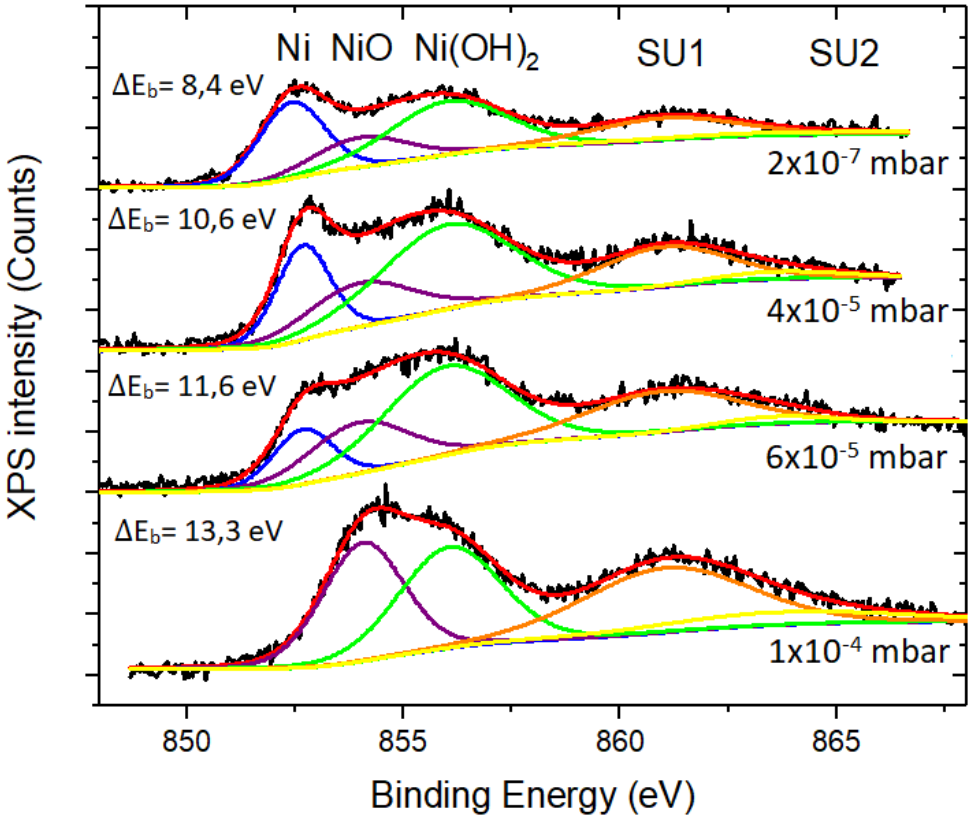


**Figure 6.12:** $Ni_{2p}$ XPS spectra of NiOx samples deposited at different oxygen pressures. The spectra were shifted accordingly so that the XPS peak from the $Ni(OH)_2$ bond appears always at its position measured by Mansour [92] (856.2 eV)

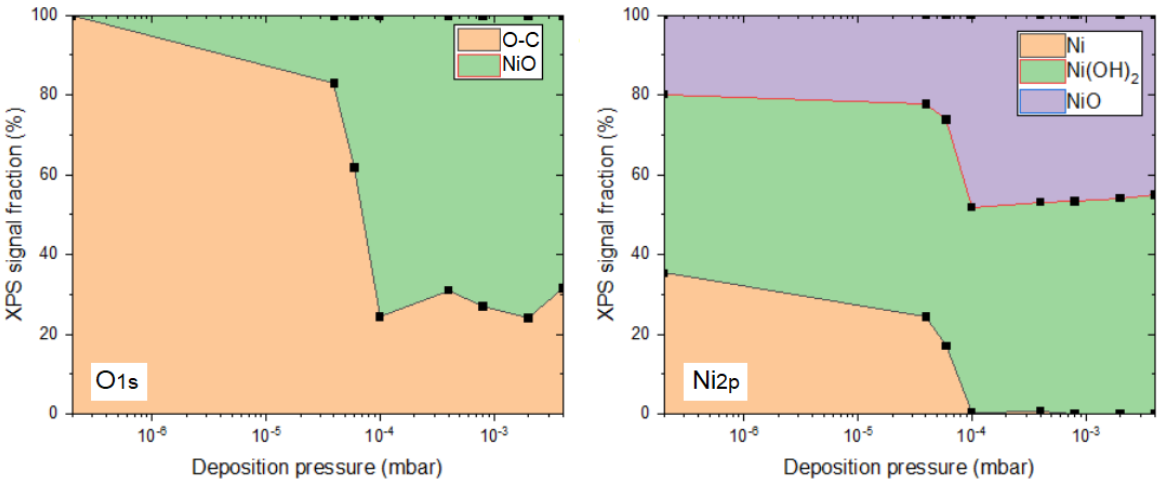


**Figure 6.13:** XPS signal fraction of the peak components used for fitting the XPS spectra as a function of the deposition pressure under which the layers were deposited. On the left, the information about the oxygen 1s peak can be seen and on the right that of the $Ni_{2p}$ core level. It can be seen, that the deposition range in which the change from metallic nickel to nickel oxide happens is between $1 \times 10^{-5}$ mbar and $1 \times 10^{-4}$ mbar.

oxygen bound to nickel (O-Ni) increases with increasing deposition pressure, with a sharp increase at $4 \times 10^{-5}$ mbar.

As it is shown in Figure 6.13 (*right*) for the $Ni_{2p}$ core level, the relative peak area of metallic nickel (Ni) decreases from 35% at $2 \times 10^{-7}$ mbar to 0% at $1 \times 10^{-4}$ mbar. As mentioned above for the $O_{1s}$ core level, the layer, deposited without any additional oxygen flow also shows NiOx in the $Ni_{2p}$ core level with a relative peak area of 19%. Again, this can be attributed to the fact that the samples were transported between the e-beam evaporator and the XPS measurement system by breaking the vacuum. It can be expected that the surface of the samples oxidizes to a certain degree during this time, which is then clearly visible by the very surface sensitive measurement. The relative peak area of the NiO increases from 22% to 48%, when increasing the deposition pressure from $4 \times 10^{-5}$ mbar to $1 \times 10^{-4}$ mbar. This sudden increase coincides with the disappearance of the metallic nickel signal. For higher oxygen deposition pressures, the fraction of NiO stays constant at around 46%. Over the whole deposition pressure range, the relative peak area of $Ni(OH)_2$ remains constant at around 50%. This results most probably, similar to the O-C bonds, from surface contamination and hydroxidation and is in agreement with relative peak areas also seen by Mansour [92].

From the analysis presented in this section, it can be concluded that in general the amount of NiOx in the layers increases for depositions with increasing oxygen deposition pressure, while the metallic fraction disappears. A significant change in composition occurs between $4 \times 10^{-5}$ mbar and $1 \times 10^{-4}$ mbar.

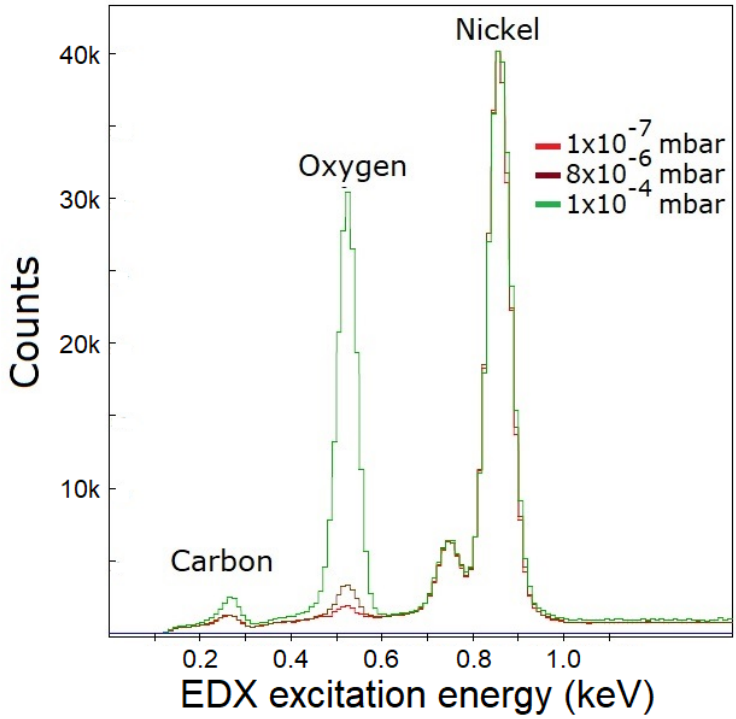


**Figure 6.14:** EDX measurements of 500 nm thick NiOx samples on glass. A primary electron acceleration voltage of 5 kV was used. The increasing amount of oxygen in the layer deposited at the higher oxygen pressure can be clearly seen.

## 6.3 EDX measurements

EDX measurements of 500 nm thick layers are shown in Figure 6.14. The data are normalized to the intensity of the Ni peak, in order to be able to appreciate the relative size of the oxygen peak relative to the Ni peak for layers deposited under different pressures. The samples analysed were deposited at oxygen pressures of $1 \times 10^{-7}$, $8 \times 10^{-6}$ and $1 \times 10^{-4}$ mbar. The EDX signal corresponding to oxygen can be seen to increase in intensity accordingly with the amount of oxygen present in the deposition atmosphere. The relative peak areas of nickel, oxygen and carbon of these samples is obtained from the peak areas and shown in Table 6.2. The EDX signal of carbon measured in the samples can be a consequence of the graphite crucible which is used as a nickel reservoir during the e-beam evaporation.

| **Pressure** [mbar] | **Nickel** [at.%] | **Oxygen** [at.%] | **Carbon** [at.%] |
|---|---|---|---|
| $1 \times 10^{-7}$ | 88 | 6 | 6 |
| $8 \times 10^{-6}$ | 83 | 11 | 6 |
| $1 \times 10^{-4}$ | 44 | 50 | 6 |

**Table 6.2:** Relative peak areas of nickel, oxygen and carbon in samples from EDX. These results also indicate that the oxygen present in the atmosphere during the deposition is being built-in into the layers.

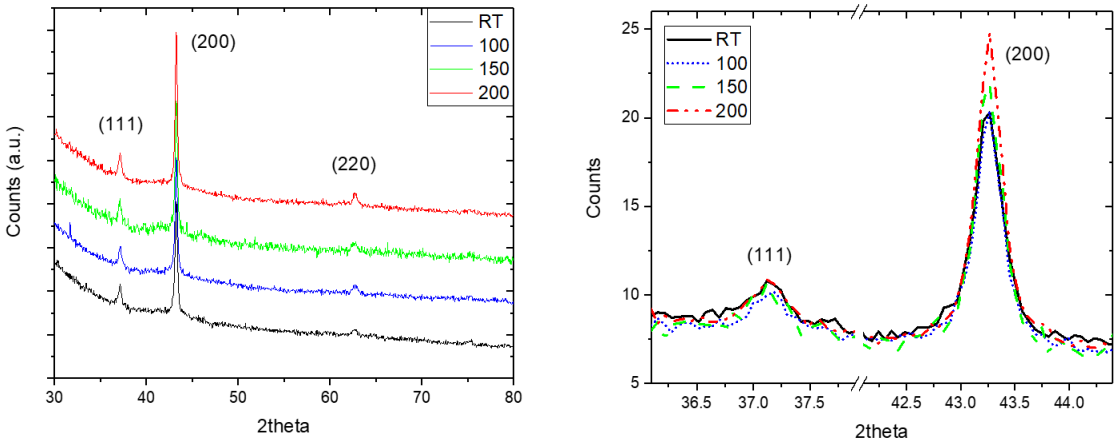


**Figure 6.15:** XRD spectra of 200 nm thick NiOx layers deposited on substrates heated at different temperatures are shown. A small increase in the intensity of the peak at $2\theta = 43.2°$ can be observed. This peak is related to the (200) crystalline plane orientation of nickel oxide, indicating an increase in the crystallinity of the material for higher substrate temperatures. The small peak at $2\theta = 37.2°$, is related to the (111) crystalline plane orientation of NiOx.

These results also indicate that the oxygen present in the atmosphere during the deposition is being built-in into the layers. This results are in agreement with the previous XPS spectra, which also suggested that oxygen atoms are present inside the thin films. It should be noted, nevertheless, that the difference between the information depth of the EDX and XPS measuring techniques could lead to discrepancies in the measured signals of the films, and also, that these techniques give us only a signal fraction and not a quantitative amount of nickel and oxygen in the samples. The fact that XPS is a more surface sensitive technique and that there is a vacuum break between NiOx deposition and XPS measurement, which could lead to impurities and oxygen adhering to the surface of the sample, could produce a measurement in which the XPS signal of these impurities plays a bigger role in the spectrum.

## 6.4 XRD measurements

Figure 6.15 shows XRD spectra (see Section 3.2.7) of NiOx layers with a thickness of 200 nm, deposited with e-beam evaporation on substrates at different temperatures. The substrate temperatures were room temperature, 100 °C, 150 °C and 200 °C. This was made in order to investigate if the substrate temperature during growth has an influence on the crystallinity of the layers. A small increase in the intensity of the peak at $2\theta = 43.2°$ when increasing the substrate temperature can be appreciated. This peak is related to the (200) crystalline plane orientation of nickel oxide, and it has a higher intensity than the peak appearing at $2\theta = 37.2°$,

so it can be concluded that the NiOx layers produced with e-beam evaporation in a reactive process are crystalline samples.

Analysing these peaks and using Scherrer's equation, it can be said that the average size of the crystallites forming the film increase in size from 16 nm to 18 nm when increasing the substrate temperature from room temperature to 200 °C.

## 6.5 Electronic properties of NiOx/a-Si:H/c-Si heterojunctions

After the material characterisation was completed and the NiOx layers were discarded as a suitable material for the elaboration of TCO layers, they were tested for their performance as charge selective contacts by depositing thin layers with a thickness from 3 to 5 nm on top of silicon wafers passivated on both sides with 5 nm (i)a-Si:H (see Section 4.2). The minority charge carrier lifetime can be measured indirectly by measuring the photoconductance of a silicon wafer as a function of time after it is illuminated with a flash light that photogenerates electron-hole pairs (see Section 3.2.8).

The NiOx depositions showed a strong detrimental effect on the passivation properties of the approx. 5 nm thick a-Si layer previously deposited on the silicon wafer, lowering the minority charge carrier lifetime of these samples from several milliseconds by a couple orders of magnitude to the microseconds range, as it can be seen in Figure 6.16.

Annealing treatments at temperatures up to 200 °C had no beneficial effect for the charge carrier lifetime of the passivated silicon wafers on which NiOx was deposited.

In order to analyse this phenomenon a detailed analysis of the depositions was made, in order to rule out a range of possible factors that could be causing the strong decrease in charge carrier lifetimes.

### 6.5.1 Investigation of the interaction between X-rays and the a-Si layer

The first hypothesis consisted of the possibility that the X-rays produced during the e-beam deposition, which are emitted tangentially to the trajectory of the electrons, irradiate the passivated wafer, and their energy is responsible for destroying the bonds between the atoms within the a-Si layer and in the c-Si wafer. This therefore destroys the surface passivation properties of the a-Si layer, and lowers the charge carrier lifetime of the wafers.

In order to discard this hypothesis, a wafer passivated with 5 nm (i)a-Si was placed in the substrate holder between two glass pieces, so that the X-rays produced during the e-beam

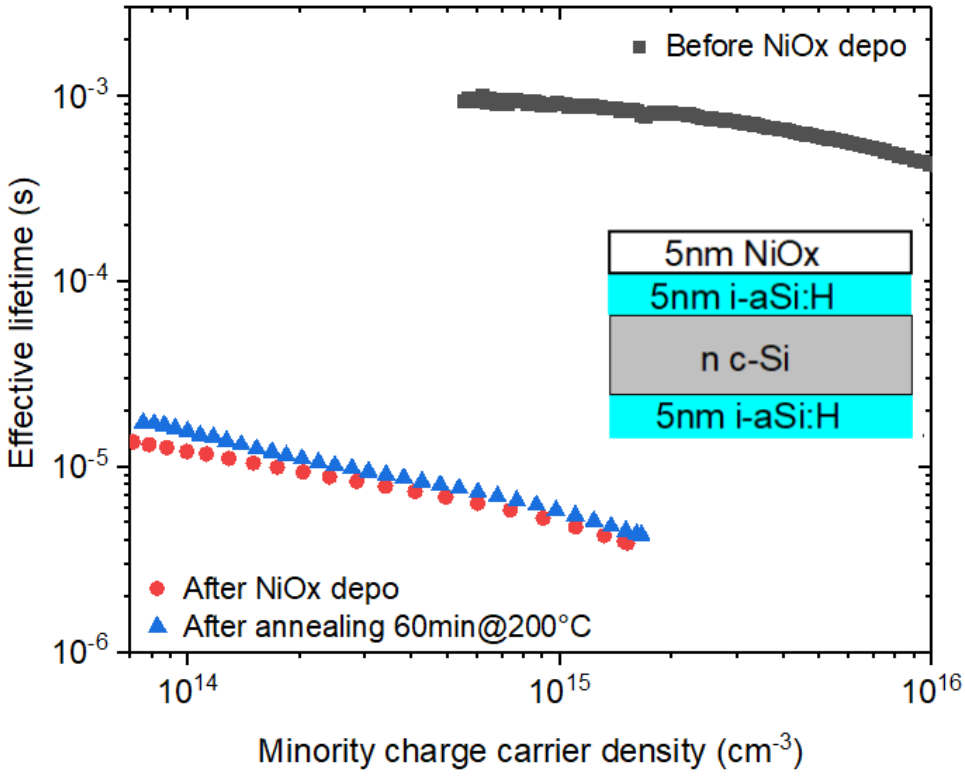


**Figure 6.16:** Minority charge carrier lifetime of an electronically pasivated wafer as a function of the minority charge carrier density. A decrease in the lifetime over 2 orders of magnitude can be seen after the e-beam deposition. An annealing treatment improves the lifetime slightly, but not to the original value.

evaporation process at an oxygen partial pressure of $4 \times 10^{-3}$ mbar could reach the wafer but the NiOx was deposited on the glass piece. This experiment made it possible to analyse the detrimental effect of the deposition environment separated from any chemical reaction that could be taking place between the nickel, the oxygen and the silicon.

The charge carrier lifetime of these samples showed no significant decrease, which allowed us to discard the X-ray radiation of the e-beam process as being responsible for the destruction of the passivation. The measured minority charge carrier lifetimes can be seen in Figure 6.18 (black, red). Both wafers show a small decrease in lifetime, nevertheless it is not critical for the production of a solar cell since the value after the deposition is still an indicator of good surface passivation.

### 6.5.2 Investigation of a possible oxidation of the a-Si surface aided by the energy of the X-rays

A new hypothesis was formulated as follows: the X-ray radiation of the e-beam process, together with the oxygen present in the atmosphere, are responsible for the decrease in charge carrier lifetimes of the samples.

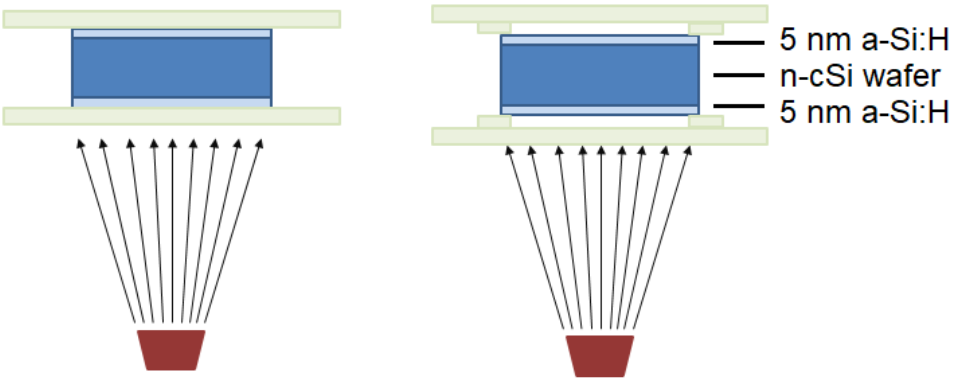


**Figure 6.17:** Experimental setup for testing the effect of X-ray and oxygen atmosphere on the passivation properties of the a-Si layer. The passivated silicon wafer is placed between two glasses during the deposition to investigate the effect of X-rays separated from the nickel deposition (*left*) and covered by glass and separated from them by 4 small glass spacers that allow the contact of oxygen with the a-Si layer (*right*), to investigate a possible oxidation aided by X-rays.

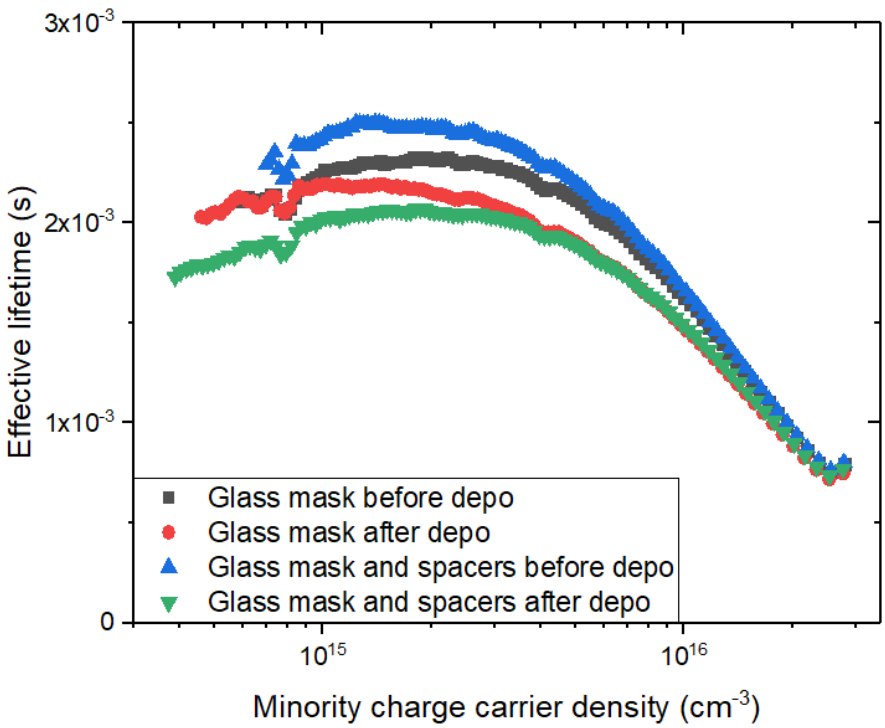


**Figure 6.18:** Charge carrier lifetimes of passivated wafers as a function of the minority charge carrier density. The data of samples covered by glass and by glass and spacers are shown before and after the NiOx e-beam depositions. A decrease in lifetime for lower charge carrier densities can be seen, probably due to handling of the samples.

In order to test this hypothesis, a wafer passivated with 5nm a-Si:H was placed in between two glass pieces, but small glass spacers were placed on the corners of the wafer, so that the oxygen present in the atmosphere is allowed to be in contact with the wafer while the deposition of NiOx under an oxygen partial pressure of $4 \times 10^{-3}$ mbar was performed. The experimental setup can be seen in Figure 6.17.

Once again, the charge carrier lifetime of these passivated wafers showed no significant decrease after deposition as it can be seen in Figure 6.18 (blue, green). A small decrease in the charge carrier lifetime can be seen, which can be attributed to the handling of the wafers. Due to the fact that the samples covered by glass showed no significant decrease in charge carrier lifetime after the e-beam process, a new experiment was planned, in order to analyse the effect of the NiOx deposition and the possible X-ray effect separated from each other. In the new experimental setup, a passivated wafer was placed on the substrate after a fraction of its surface was masked with a glass piece. A small part of the wafer surface was left unmasked. This made it possible for the evaporated nickel to reach this part of the wafer and deposit itself on it, which might have lead to an interaction between the a-Si layer and the nickel. Using photoluminiscence measurements it is possible to analyse a silicon wafer and differentiate between regions in the wafer in which radiative recombination is taking place from regions in which other recombination types are limiting the charge carrier lifetime (see Section 3.2.4).

The photoluminescence measurement of the wafer on which a partial deposition of NiOx was done is shown in Figure 6.19. This photoluminescence image lets us conclude that the reason for the drastic decrease in the charge carrier lifetime of the samples is not related to the interaction of the passivated wafer and the X-ray radiation produced during the e-beam process, while the wafer is in an oxygen atmosphere. It is now clear that the main detrimental factor to the passivated properties of the a-Si layer is the actual deposition of nickel atoms or NiOx molecules (in case they are formed in the gas phase during deposition) on the surface of the wafer, maybe due to a chemical reaction between nickel and silicon and the introduction of electronic trap states in the interface between these two materials.

## 6.6 Hypothesis about NiOx deposition on a-Si/c-Si

Since it was found that a NiOx deposition on passivated wafers had a detrimental effect on the charge carrier lifetime of the samples, a new hypothesis was formulated consisting of the possibility of nickel atoms reaching the a-Si/c-Si interface. This could happen due to a damage

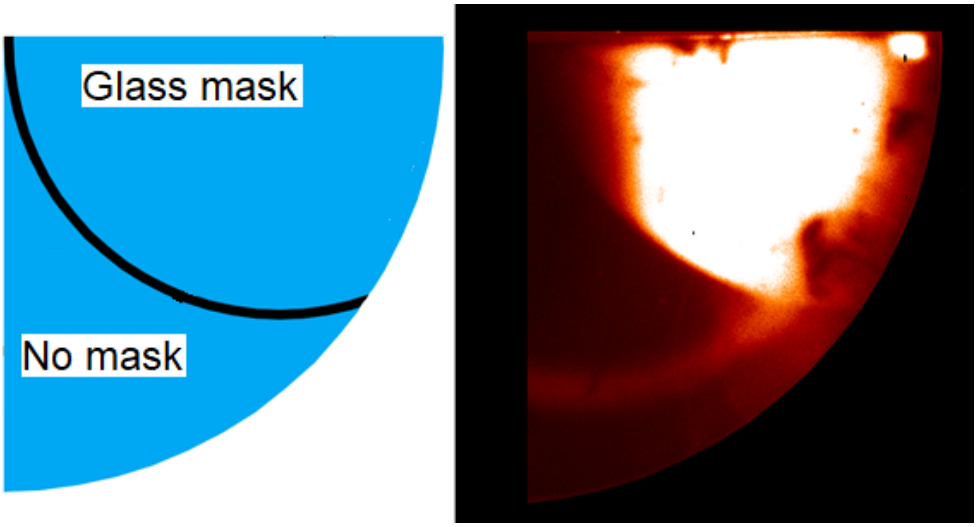


**Figure 6.19:** Photoluminescence measurements of a partially covered silicon wafer after NiOx deposition. The glass mask used only covered a region of the wafer in order to analyse if the deposition of NiOx has a detrimental effect on the surface passivation. The image shows that the covered part of the wafer still has good surface passivation after the e-beam deposition.

of the thin a-Si layer caused by a reaction with nickel atoms or due to a diffusion of nickel atoms through the layer. Taking into account the low diffusion coefficient of Ni in a-Si this is improbable, but it was nevertheless investigated using GDOES.

GDOES is a method for analysing the composition of a material, especially useful for layered systems because its working principle is based on the analysis of the surface atoms while ablating the sample, so that deeper layers of the system can be successively analysed. Further details in Section 3.2.3.

The first structures that we tested were planned to be solar cells, and for this reason the a-Si layer had a thickness of only 5 nm. This thickness ensures that a passivation of the c-Si dangling bonds takes place, but the parasitic absorption of the a-Si layer is maintained at a reasonably low value.

In order to test qualitatively if nickel is diffusing in the a-Si layer, the sample shown in Figure 6.20 was analysed using GDOES. This sample consists of a c-Si wafer with a 160 nm thick layer of a-Si and 10 nm of pure nickel on top.

The GDOES measurement of the layered system shown in Figure 6.20 can be seen in Figure 6.21. In the GDOES measurement the signal of nickel and of silicon can be seen as a function of measurement time. At the beginning of the measurement, both the signals of silicon and nickel show a sudden increase, which can be caused by the fact, that the plasma used for measuring GDOES takes a few seconds to stabilize. The signal intensity of nickel is larger than that of silicon at the beginning of the measurement but both materials can

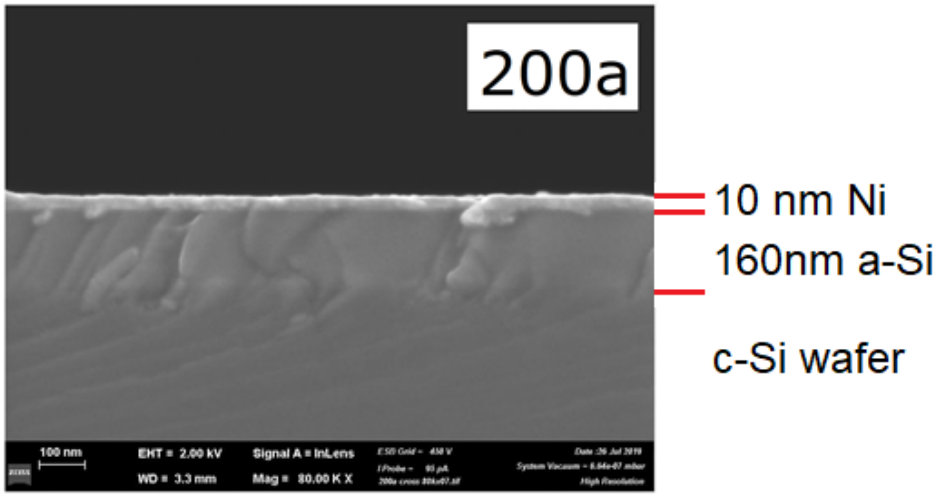


**Figure 6.20:** SEM image of a c-Si wafer with a 160 nm thick a-Si layer and a 10 nm nickel layer on top.

be detected, pointing to a possible coexistence of nickel and silicon in this region, either as separated phases or as nickel silicide. After some seconds, the intensity of the nickel signal decreases exponentially while the signal of silicon stabilizes.

The exponential decrease in the Ni signal could indicate that a diffusion process is taking place, but it has been shown by Olowolafe et al. [65] that nickel and silicon react and form nickel silicide during an e-beam deposition of nickel on a-Si. Similar studies for e-beam depositions of nickel on a-Si in a reactive process under an oxygen atmosphere were not found by the author.

If a diffusion process is taking place, this system can be considered a diffusion of nickel into silicon from an exhaustible source, since the initial concentration of nickel atoms at the surface should decrease over at least one order of magnitude if the 10 nm nickel layer is distributed homogeneously over an a-Si layer that is more than one order of magnitude thicker.

For testing if nickel can be further diffused into a-Si, a layered system consisting of a c-Si wafer, 160 nm a-Si and 200 nm NiOx was prepared and cut into 4 pieces. Each piece received a different annealing treatment. Three of those pieces were annealed at 200 °C for 10, 60 and 180 minutes, while one of them was not annealed, representing the “as deposited” state. After this, GDOES was measured on the samples and the results are shown in Figure 6.22. The signal represents the amount of nickel inside of the sample as a function of GDOES measuring time and therefore as a function of the depth inside the sample.

The expected result of this experiment in the case that a diffusion process takes place, was a variation in the nickel GDOES signal as a function of time. The Ni GDOES signal is related to the Ni concentration in the a-Si:H layers. Such a result would show that for longer

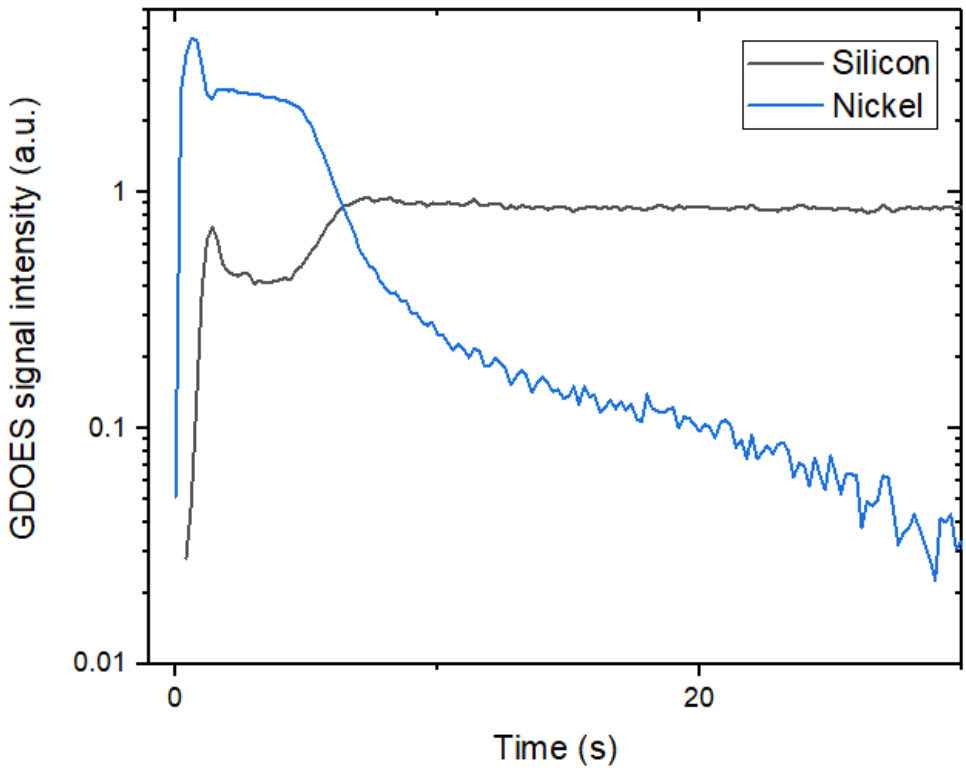


**Figure 6.21:** GDOES measurement of the sample shown in Figure 6.20. An exponential decay of the nickel signal can be seen for an increasing measurement time as well as an increase and stabilization in the silicon signal. The measurement time is proportional to the measurement depth inside of the sample. A region in which Ni and Si coexist can be seen.

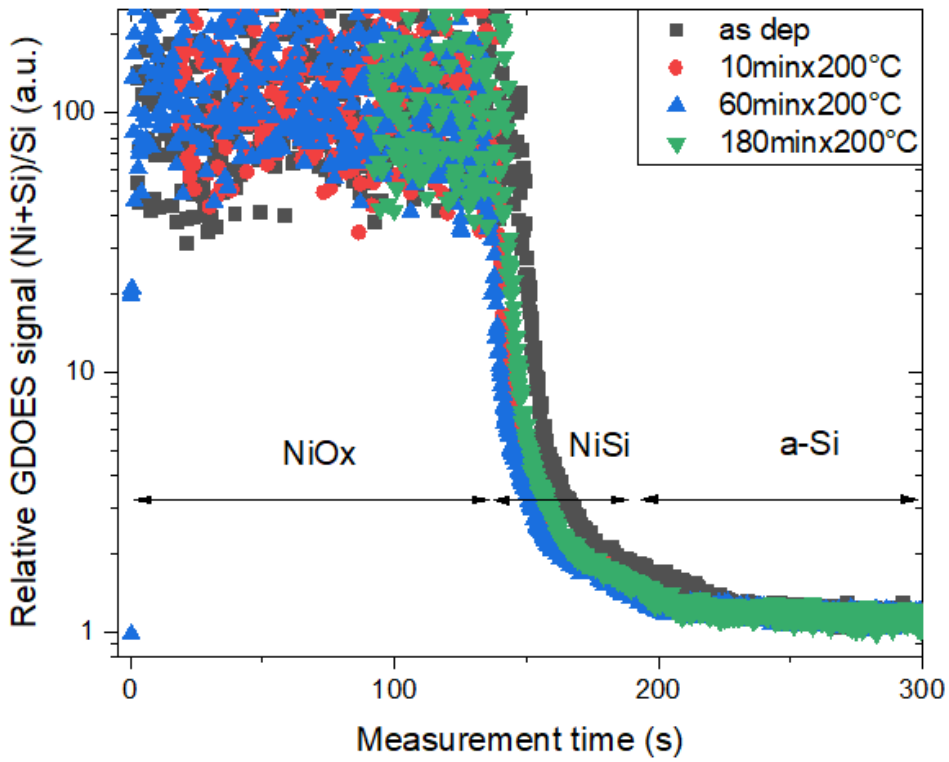


**Figure 6.22:** GDOES signal of nickel relative to the total GDOES signal for samples consisting of silicon wafers with 160 a-Si and 200 nm NiOx deposited on top and annealed at 200 °C for different amounts of time. A similar exponential decay can be observed for all samples. A small horizontal offset can also be seen, probably due to variations in the mounting of the samples in the GDOES measuring device.

annealing times the nickel atoms can be found at a greater depth inside of the a-Si. The results of the experiment contradict this hypothesis.

As it can be seen from Figure 6.22 the decreasing behaviour of the curves is very similar for all the samples, even for that which was not annealed. For a short region in the middle of the graph GDOES signals of Ni and Si can be detected simultaneously. From this observation it was concluded that a diffusion process is not taking place, but more probably a reaction between nickel and silicon atoms at the beginning of the NiOx deposition. Annealing steps made after the deposition to the layered system do not have a great effect on the nickel diffusion inside of the amorphous silicon layer. The small difference between the position of the curves (horizontal offset) could be explained by a small inhomogeneity in the thickness layer due to the deposition technique and a variation of the spot on the wafer on which the GDOES measurement was made. For the samples annealed for 10 minutes and 3 hours, some data at the beginning of the measurement was not recorded by the GDOES system, it was assumed, nevertheless, that the nickel GDOES signal is similar to that of the "as dep" case

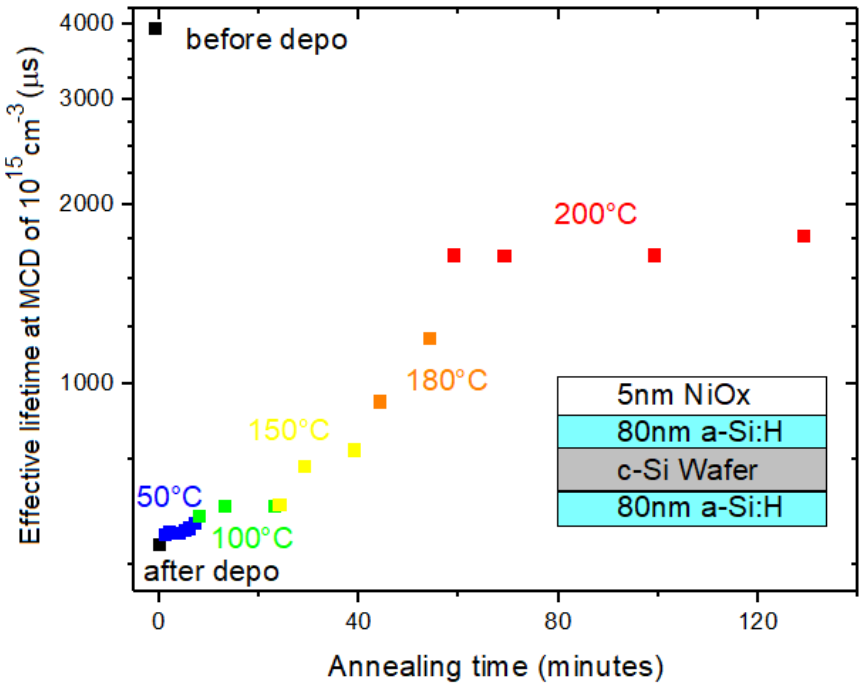


**Figure 6.23:** Variation of the charge carrier lifetime for a sample consisting of a c-Si wafer with 80 nm a-Si and 5 nm nickel oxide. The black dot on the upper left of the graph shows the charge carrier lifetime before deposition and the one on the lower left the charge carrier lifetime exactly after the nickel deposition. An increase in charge carrier lifetime can be seen for this sample after annealing treatments were performed at temperatures varying from 50 to 200 °C.

and the sample annealed for 1 hour, since this region represents the GDOES measurement on the NiOx layer.

The annealing tests for thick a-Si layers revealed also some new information. It was found that, for thick a-Si layers (approx. 100 nm for example), the charge carrier lifetime of the sample does not decrease as drastically after the NiOx deposition as it was the case of the same experiments with thin a-Si layers.

Furthermore, the minority charge carrier lifetime at a density of $1 \times 10^{15}$ cm$^{-3}$ of the samples increased after successive annealing steps at different temperatures up to 200 °C, as is shown in Figure 6.23. The two black dots on the left represent the lifetime before and after the deposition, and the coloured dots represent the increase in lifetime for annealing at different temperatures, indicated in the graph by the same colour as the respective dots.

As it can be seen in Figure 6.23, the charge carrier lifetime before the NiOx deposition at 4 ms indicates good surface passivation. After NiOx deposition, this lifetime decreases to approximately 500 $\mu$s, but successive annealing steps make it possible to restore the lifetime back to a value over 1 ms.

At this point, a distinction between thin (5 to 10 nm) and thick (100 nm and thicker) a-Si layers has to be made. The results mentioned in the previous section show that for thin a-Si

layers, the decrease in charge carrier lifetime can not be recovered by annealing the samples. Since this is not the case for thick a-Si layers, the following hypothesis appears reasonable: the interaction (most probably a chemical reaction) between nickel and silicon atoms at the interface between these two materials is a process that happens shortly at the beginning of the deposition. Once this process has taken place the subsequent nickel atoms arriving to the substrate get deposited and combine with the oxygen present in the atmosphere, so no more nickel atoms react with the surface silicon atoms of the a-Si layer.

The hypothesis would suggest that the beginning of the deposition is enough to affect the first 10 nm of a-Si, maybe through a chemical reaction, forming nickel silicide for example, but at some distance between the first 10 nm and the following 90 nm, the interaction between nickel and silicon atoms stops, allowing the a-Si/c-Si interface to maintain its passivating properties.

In particular, as it has been found in the literature about NiSi formation [65], the author thinks that the formation of nickel silicide in the first nanometers of the Ni/a-Si interface acts as a barrier that stops subsequent nickel atoms from reacting with silicon atoms located deeper into the silicon layer. This makes it possible for the NiOx molecules to deposit onto the previously formed NiSi layer.

## 6.7 Formation of nickel silicide at the interface between nickel oxide and silicon

After discarding the hypothesis that a diffusion of nickel atoms through the a-Si layers was responsible for the strong decrease of its passivation properties, the XPS measurements of the NiOx/a-Si/c-Si system were analysed.

For this purpose, some of the previously prepared samples with NiOx layers of 2 and 110 nm deposited at an oxygen partial pressure of $4 \times 10^{-3}$ mbar were analysed and compared. Specifically the XPS spectra of these samples were taken into account in order to check if an XPS signal of nickel silicide can be appreciated.

Peaks related to nickel silicide were found by Tam and Nyborg [106] with different nickel-to-silicon ratios and at a binding energy slightly lower than the position of the $Ni_{2p\ 3/2}$ related to NiOx. In that paper, nickel silicides with different nickel to silicon ratios are analyzed and their position is found approx. between that of metallic nickel ($\approx$ 853 eV) and the peak related to NiOx ($\approx$ 854.3 eV).

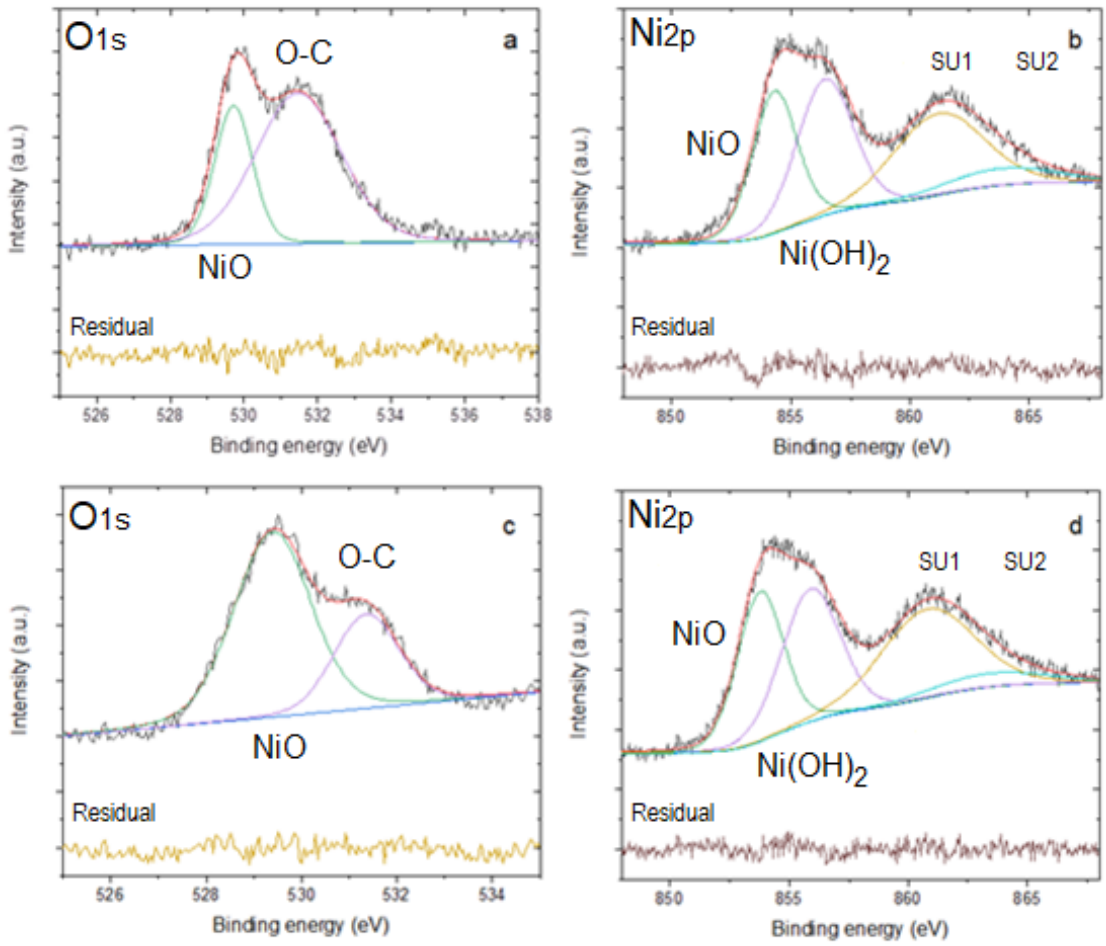


**Figure 6.24:** XPS detail spectra of c-Si/a-Si/NiOx layered systems. The sample with 2 nm NiOx is shown in a ($O_{1s}$) and b ($Ni_{2p}$). The sample with 110 nm NiOx is shown in c ($O_{1s}$) and d ($Ni_{2p}$). A clear difference can be seen for the $O_{1s}$ peaks. The signal component situated at a lower binding energy, which is related to the NiOx peak has a higher intensity for the 110 nm NiOx layer in comparison with the 2 nm NiOx layer, this might be caused by the fact that such a thin NiOx layer does not have enough material to produce a reasonable XPS signal. For the $Ni_{2p}$ peak of the 2 nm layer a small difference between the XPS signal and the fit can be seen on the left side of the NiO peak, around 853 eV. The residual signal for each case is shown in the lower part of the graph.

In the XPS spectra of these samples, shown in Figure 6.24, the $Ni_{2p}$ and the $O_{1s}$ peak can be seen. The parameters used for fitting these XPS spectra are the same as the ones used for the NiOx layers in Section 6.2.

If the XPS spectra of the samples with 2 nm NiOx and 110 nm NiOx are compared, a small difference between the XPS signal and the fit can be seen at approximately 0.5 eV to the left of the NiOx peak (i.e. at a lower binding energy) in Figure 6.24 b). It has been reported by Tam and Nyborg [106] that the XPS signals of nickel silicides can be found at such binding energy values.

Figure 6.25 shows a fitting of the XPS signal of the 2 nm thick sample using the fitting parameters of Section 6.2, in which the data were shifted so that the $Ni_{2p\,3/2}$ peak appears

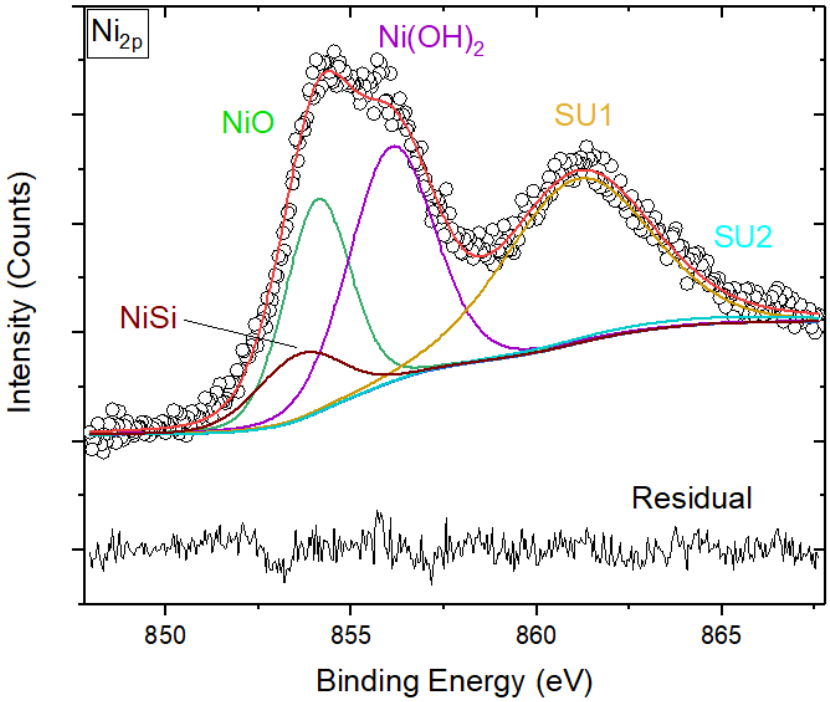


**Figure 6.25:** $Ni_{2p\ 3/2}$ XPS signal of the 2 nm thick NiOx on silicon sample, showing the presence of nickel silicide at approx. 853.6 eV. The spectrum was shifted accordingly so that the XPS peak from the $Ni(OH)_2$ bond appears at its position measured by Mansour [92] (856.2 eV)

at 854.1 eV, as reported also by Mansour [92], and a new peak was added to account for a possible NiSi signal at 853.6 eV with a FWHM of 2.7 eV which is similar to the FWHM of the other XPS peaks. It has been shown by Tam and Nyborg [106] that the position of the NiSi depends on the amount of nickel and silicon in the sample going from 853.2 eV for a sample containing 66% Ni to 854.1 eV to a sample containing only 20% Ni. Since in our system the specific composition of the material was not determined, and even different ratios of Ni to Si could be present, the presence of this new peak is only meant to confirm the presence of NiSi in the sample, at the interface between silicon and nickel oxide. If the same peak is added to the 110 nm sample, the fitting software reduces the area of this peak to zero when optimizing the areas and positions of the peaks, indicating an absence of a NiSi signal for that sample.

These results could point to a confirmation of the hypothesis that the first monolayers of nickel deposited on the a-Si surface react with the silicon atoms, binding to them and forming nickel silicide. After this reaction takes place and a nickel silicide layer is formed, the following nickel atoms that are deposited onto the nickel silicide surface do not diffuse through the nickel silicide, and subsequently form a bond with the oxygen atoms present in the deposition atmosphere forming nickel oxide.

In order to confirm this unequivocally, a more detailed analysis of the XPS signal of the system should be performed. Either preparing many samples with different thicknesses ranging from fractions of a nanometer to approx. 10 or 20 nm (this thickness value would ensure that the XPS measurement is made far from the a-Si/Ni interface), or, even better, depositing a 20 nm thick layer of NiOx on a c-Si wafer passivated with a-Si and sputtering away small quantities of NiOx in between XPS measurements and without exposing the samples to contact with the atmosphere. The second approach would ensure that the XPS measurements are done on a less contaminated system since the vacuum would not be broken between measurements. An analysis of the silicon XPS signal in such an experiment would give useful information about the nickel silicide formation at the interface. For the experiments made in this thesis the $Si_{2p}$ XPS signal was not analysed, since the focus of the measurements was on a possible change in the $Ni_{2p\ 3/2}$ XPS signal.

The presence of a nickel silicide at the interface would also indicate that the oxidation of the evaporated nickel atoms does not take place while the nickel is in a gaseous phase and moving towards the substrate, but only after it reaches the substrate. This would be a general conclusion about the e-beam deposition process, since it can be assumed this is the same for all the samples, not only for the nickel deposited onto silicon. This lets us establish a chronological order of the processes taking place when this deposition technique is used for producing NiOx layers.

According to these measurements, the electronic system that we obtain after the reactive e-beam deposition of nickel under an oxygen atmosphere is not NiOx/a-Si/c-Si but NiOx/NiSi/a-Si/c-Si, which is not the system in which NiOx can be used as a charge selective contact, since an interlayer is formed which seemingly cannot be avoided.

New approaches to this problem could be to analyse if it is possible to tune the properties of the NiSi layer in order to form an electronic contact or trying to deposit the NiOx using another deposition technique, specifically a non-reactive process for which the Ni-O bonds are already formed at the beginning of the deposition and therefore a formation of NiSi can be avoided.

In particular, according to the existing literature about NiSi as a contact material for Si solar cells (see Section 2.13) and specially the work of Olowolafe et al. [65], the author of this thesis thinks that a more detailed study of the formation of NiSi from a-Si layers and e-beam evaporated nickel should be investigated. If a systematic study on this topic is performed it might be possible to find an optimum a-Si:H layer thickness from which a fraction of the a-Si:H

material combines with nickel to form a conductive layer while the remaining amount of a-Si:H performs as a passivation layer. This topic is unfortunately out of the scope of this thesis.

## 6.8 Chapter Summary

Nickel Oxide was investigated as a potential material to be used as a charge selective contact for holes in SHJ structures. Layers were prepared using a reactive e-beam evaporation process using nickel pellets as a source and carrying out the evaporation in an oxygen atmosphere on glass substrates. It was shown using XPS and EDX measurements, that it is possible to obtain a range of layer stoichiometries from metallic nickel to NiOx when increasing the amount of oxygen present in the deposition atmosphere. The layers were characterized using UV-VIS and electrical measurements, and it was found that the resistivity of the most metallic layers can be lowered over one order of magnitude if annealing steps at temperatures up to 600 °C were performed. Using XRD measurements it was found that the NiOx layers crystallize mainly in the (200) orientation, and that the average size of the crystallites conforming the layers can be increased from about 16 to 18 nm if the evaporation is performed on a substrate heated at 200 °C instead of room temperature.

It was found, that a deposition of NiOx on silicon wafers passivated with a few nm a-Si:H (SHJ structures) decreases the minority charge carrier lifetime in the samples over many orders of magnitude to the microseconds range and a detailed analysis of the cause of this phenomenon was undertaken. It was possible to rule out the X-ray radiation produced by the e-beam process as the reason of the lifetime decrease as well as a possible oxidation of the a-Si layers due to the oxygen atmosphere. The possibility of diffusion of nickel atoms through the a-Si layers up to the a-Si/c-Si interface was considered as the reason for the lifetime decrease and NiOx/a-Si/c-Si structures were prepared and annealed at 200 °C for different amounts of time in order to measure the diffusion coefficient of nickel in silicon. However, GDOES measurements of the samples suggest that a process of diffusion is not taking place in this structures.

XPS measurements of a-Si:H passivated wafers with 2 nm NiOx and 110 nm NiOx were compared and a small XPS signal was found in the 2 nm NiOx layer which is not present in the 110 nm layer. This XPS signal is placed at a binding energy that corresponds to nickel silicide according to studies made by Tam and Nyborg [106], which suggests that a thin layer of nickel silicide is being formed between the a-Si and the NiOx. The author considers this

interlayer to be the reason for the detrimental effects of the NiOx deposition on the a-Si layers, nevertheless this should be investigated in more detail, as it is a new system consisting of NiOx/NiSi/a-Si/c-Si and not the intended system consisting of only NiOx/a-Si/c-Si.

# 7

# Conclusions and Outlook

In this thesis ZnO:Al and nickel oxide were tested as possible replacements for ITO as a contact for SHJ solar cells.

It has been shown, that when using pulsed-DC sputtered ZnO:Al as a front TCO on a rear emitter SHJ solar cell the power conversion efficiency of the device is only 0.2% lower than that of the cell with an ITO front TCO reaching an efficiency well above 22%.

This was an unexpected good result, since it is known that ZnO:Al sputtered as a 75 nm thin layer at a rather low temperature, below 200°C, usually results in poor crystallographic quality, and, hence, low electrical performance. Because ZnO:Al grows as crystalline film with a relatively thick and low quality incubation layer on the substrate, it requires a certain minimum film thickness, typically several hundred nanometers, and a temperature ideally well above 200°C, to form a dense structure with large grains, which is required for a high charge carrier mobility and hence high conductivity at low charge-carrier density. ITO, in contrast, forms relatively large grains even as a thin layer and at temperatures around or even below 200°C. For that reason no SHJ cell with ZnO:Al as the front TCO had been reported with a performance being comparable to that of a cell with ITO. We found that two specific facts, however, can explain the good cell results with ZnO:Al. Firstly, the ZnO:Al exhibits excellent optical transparency leading to high short circuit current. Secondly, to cope with the limited lateral conductivity, we chose the rear emitter (also: rear junction) cell design. Traditionally, Si solar cells are in front emitter design in order to allow the minority carriers to have the shorter path to the junction. With high quality, i.e. high lifetime Si wafers, as used for SHJ cells, this is not limiting any more. Therefore, the rear emitter design was suggested

by Bivour et al. [21]. It relaxes the demand on a highly conductive front TCO as the Si wafer supports lateral current transport significantly. The reason for the slight underperformance can be identified mainly as a higher contact resistivity between the ZnO:Al and the silver grid in comparison to the contact resistivity of the system composed of ITO and silver.

A way to improve the performance of SHJ devices using ZnO:Al as a front TCO would be therefore to find a method for improving the contact between these two materials. One option would be to investigate a different silver paste, which forms a better contact with the ZnO:Al surface. Also a thin ITO capping layer might improve the contact to the metal.

During the investigation of the nickel oxide films, it has been concluded, first of all, that it is possible to produce nickel oxide thin films from a nickel target in a reactive process under an oxygen atmosphere using an e-beam evaporator.

The properties of these thin films can be varied from well-conducting pure nickel layers to nickel oxide thin films with an optical bandgap of $\approx 3.34$ eV if the oxygen partial pressure of the system is varied. The conductivity of the more metallic films can be lowered by more than order of magnitude if the layers are subjected to a thermal treatment in ambient air of up to 360 °C.

By observing the optical and electronical properties of these layers they can be ruled out as possible TCO materials, since the combination of their transmittance and electrical conductivity is not in the same range as those of other TCOs such as ZnO:Al or ITO. For this reason the nickel oxide layers were investigated as a possible material for forming charge selective contacts for the collection of holes.

The deposition of nickel oxide thin films on test SHJ structures leads to a pronounced degradation of the passivation properties of the a-Si layers, which is measured as low minority charge carrier lifetimes in the wafers using photoluminescence and photoconductance decay measurements. The X-rays produced during the e-beam evaporation as well as a possible oxidation of the a-Si layers due to the oxygen atmosphere were ruled out as a possible reason for the decrease in charge carrier lifetime. A diffusion of nickel atoms through the a-Si layers was also ruled out by preparing Ni/a-Si/c-Si samples, annealing them for different times and measuring GDOES on them. A variation in the distribution of nickel inside of the silicon wafers as a function of annealing time was not found.

While it was found that the deposition of nickel on thin (3 to 5 nm) a-Si:H layers has a detrimental effect on the passivation of the wafer, this effect is not present when the a-Si:H layer is 10 to 20 times thicker.

By using XPS measurements of NiOx/a-Si/c-Si systems it has been found that there is a difference between the XPS signal of thin NiOx layer and a thick one. In the thin layers, the XPS signal of nickel silicide at the interface between silicon and nickel can be seen. This is due to the fact that this interface is inside the XPS measurement depth.

This fact would hint to a formation of nickel silicide in the interface between NiOx and a-Si, which makes sense if it is taken into account that the NiOx was deposited using a reactive process, in which there is a probability, that the nickel atoms are deposited onto the a-Si layer and react with it forming nickel silicide before the nickel atoms bond to oxygen atoms and form nickel oxide.

This phenomenon could be analysed in detail in a future project, but for the purposes of this thesis it can be concluded, that, even if it is possible to deposit nickel oxide layers using e-beam in a reactive process, it is not possible to use them as a TCO due to their optoelectronical properties, and also that the e-beam evaporation of nickel oxide in a reactive process under an oxygen atmosphere is not suitable for forming a charge selective contact for holes on an SHJ solar cell. The most probable reason for this is a formation of a nickel silicide interlayer between the NiOx and the a-Si, forming the system NiOx/NiSi/a-Si/c-Si which in general should behave different from the system NiOx/a-Si/c-Si.

In the opinion of the author the system NiSi/a-Si:H is worth to be investigated as a contact by repeating the experiments made at the end of this work in a systematic way to form a NiSi layer on top of the a-Si:H layer without consuming the complete a-Si:H material so the passivation of the a-Si/c-Si interface is not degraded.

In particular, the author proposes the investigation of NiSi as a replacement for silver in the metallization of SHJ solar cells, either as a seed layer for the subsequent metallization with copper as it has been implemented for other photovoltaic technologies or as a contact layer itself. If the amount of nickel deposited on top of the a-Si:H layers and their thickness is engineered correctly it should be possible to form a structure that works as a passivation layer, charge selective contact and conductive layer (i-aSi:H/n-aSi/NiSi).

# References


[1] Susanne Dröge. *The Paris Agreement 2015: turning point for the international climate regime*. Vol. 4/2016. SWP Research Paper. Berlin: Stiftung Wissenschaft und Politik -SWP- Deutsches Institut für Internationale Politik und Sicherheit, 2016, p. 33.

[2] Thomas Dittrich. *Materials concepts for solar cells*. Vol. 1. World Scientific Publishing Company, 2014.

[3] Simon M Sze and Kwok K Ng. *Physics of semiconductor devices*. John Wiley & sons, 2006.

[4] Daniel Meza, Alexandros Cruz, Anna Belen Morales, Lars Korte, and Bernd Stannowski. "Aluminum-Doped Zinc Oxide as Front Electrode for Rear Emitter Silicon Heterojunction Solar Cells with High Efficiency". In: *Applied Sciences* 9 (2019), p. 862.

[5] Daryl M Chapin, CS Fuller, and GL Pearson. "A new silicon p-n junction photocell for converting solar radiation into electrical power". In: *Journal of Applied Physics* 25.5 (1954), pp. 676–677.

[6] C. P. Murcia, R. Hao, C. Leitz, A. Lochtefeld, and A. Barnett. "Thin crystalline silicon solar cells with metallic back reflector". In: *2011 37th IEEE Photovoltaic Specialists Conference*. 2011, pp. 661–664.

[7] Kenneth E Bean. "Anisotropic etching of silicon". In: *IEEE Transactions on electron devices* 25.10 (1978), pp. 1185–1193.

[8] M Tucci and G De Cesare. "17% efficiency heterostructure solar cell based on p-type crystalline silicon". In: *Journal of Non-Crystalline Solids* 338 (2004), pp. 663–667.

[9] Seung Jik Lee, Se Hwan Kim, Dae Won Kim, Ki Hyung Kim, Beom Kyu Kim, and Jin Jang. "Effect of hydrogen plasma passivation on performance of HIT solar cells". In: *Solar energy materials and solar cells* 95.1 (2011), pp. 81–83.

[10] Jonas Geissbühler, Jérémie Werner, Silvia Nicolas, L. Barraud, A. Hessler-Wyser, Matthieu Despeisse, Sylvain Nicolay, A. Tomasi, Bjoern Niesen, Stefaan De Wolf, and Christophe Ballif. "22.5% efficient silicon heterojunction solar cell with molybdenum oxide hole collector". In: *Applied Physics Letters* 107 (Aug. 2015).

[11] Hyeongsik Park, Youn-Jung Lee, Jinjoo Park, Youngkuk Kim, Junsin Yi, Youngseok Lee, Sangho Kim, Chang-Kyun Park, and Kyung-Jin Lim. "Front and back TCO research review of a-Si/c-Si heterojunction with intrinsic thin layer (HIT) solar cell". In: *Transactions on Electrical and Electronic Materials* 19.3 (2018), pp. 165–172.

[12] Kunta Yoshikawa, Hayato Kawasaki, Wataru Yoshida, Toru Irie, Katsunori Konishi, Kunihiro Nakano, Toshihiko Uto, Daisuke Adachi, Masanori Kanematsu, Hisashi Uzu, and Kenji Yamamoto. "Silicon heterojunction solar cell with interdigitated back contacts for a photoconversion efficiency over 26%". In: *Nature Energy* 2 (Mar. 2017), p. 17032.

[13] Katharina Lodders. "Solar System Abundances of the Elements". In: *Principles and Perspectives in Cosmochemistry* 2 (Oct. 2010).

[14] H Sato, T Minami, S Takata, and T Yamada. "Transparent conducting p-type NiO thin films prepared by magnetron sputtering". In: *Thin solid films* 236.1-2 (1993), pp. 27–31.

[15] Rafael Betancur, Marc Maymó, Xavier Elias, Luat Vuong, and Jordi Martorell. "Sputtered NiO as electron blocking layer in P3HT:PCBM solar cells fabricated in ambient air". In: *Solar Energy Materials and Solar Cells* 95 (2011), pp. 735–739.

[16] R. Islam, P. Ramesh, Ju Hyung Nam, and K. C. Saraswat. "Nickel oxide carrier selective contacts for silicon solar cells". In: *2015 IEEE 42nd Photovoltaic Specialist Conference (PVSC)*. 2015, pp. 1–4.

[17] The London Metal Exchange - an HKEX Company. 2020. URL: `https://www.lme.com/` (visited on 07/13/2019).

[18] Kitco Inc. *Base & Industrial Metals - News, Charts & Quotes - KITCO Metals*. 2020. URL: `http://www.kitcometals.com/` (visited on 07/13/2019).

[19] Alexandros Cruz, Er-Chien Wang, Anna B Morales-Vilches, Daniel Meza, Sebastian Neubert, Bernd Szyszka, Rutger Schlatmann, and Bernd Stannowski. "Effect of front TCO on the performance of rear-junction silicon heterojunction solar cells: Insights from simulations and experiments". In: *Solar Energy Materials and Solar Cells* 195 (2019), pp. 339–345.

[20] DBM Klaassen. "A unified mobility model for device simulation—I. Model equations and concentration dependence". In: *Solid-State Electronics* 35.7 (1992), pp. 953–959.

[21] Martin Bivour, Heiko Steinkemper, Jan Jeurink, Sebastian Schröer, and Martin Hermle. "Rear emitter silicon heterojunction solar cells: Fewer restrictions on the optoelectrical properties of front side TCOs". In: *Energy Procedia* 55 (2014), pp. 229–234.

[22] Hiromichi Ohta, Masahiro Hirano, Ken Nakahara, Hideaki Maruta, Tetsuhiro Tanabe, Masao Kamiya, Toshio Kamiya, and Hideo Hosono. "Fabrication and photoresponse of a pn-heterojunction diode composed of transparent oxide semiconductors, p-NiO and n-ZnO". In: *Applied Physics Letters* 83.5 (2003), pp. 1029–1031.

[23] Jayasundera Bandara, C.M. Divarathne, and S.D. Nanayakkara. "Fabrication of n–p junction electrodes made of n-type SnO2 and p-type NiO for control of charge recombination in dye sensitized solar cells". In: *Solar Energy Materials and Solar Cells* 81 (2004), pp. 429–437.

[24] Daisuke Kawade, Kazuma Moriyama, Fumika Nakamura, Shigefusa F. Chichibu, and Mutsumi Sugiyama. "Fabrication of visible-light transparent solar cells composed of NiO/NixZn1-xO/ZnO heterostructures". In: *physica status solidi c* 12.6 (2015), pp. 785–788.

[25] W Van Roosbroeck and W Shockley. "Photon-radiative recombination of electrons and holes in germanium". In: *Physical Review* 94.6 (1954), p. 1558.

[26] Pierre Auger. "Sur les rayons $\beta$ secondaires produits dans un gaz par des rayons X." In: *Comptes rendus de l'Académie des sciences* 177 (1923), p. 169.

[27] Loic Tous. "Nickel/Copper Plated Contacts as an Alternative to Silver Screen Printing for the Front Side Metallization of Industrial High Efficiency Silicon Solar Cells". PhD thesis. Jan. 2014.

[28] Kyung-Sun Kim, Kwan-Hee Lee, Ung-In Cho, and Jae-Shi Choi. "A Study of Nonstoichiometric Empirical Formulas for Semiconductive Metal Oxides". In: *Bulletin of the Korean Chemical Society* 7.1 (1986), pp. 29–35.

[29] P. Drude. "Zur Elektronentheorie der Metalle". In: *Annalen der Physik* 306.3 (1900), pp. 566–613.

[30] Kirstin Alberi and John Gregoire. "The 2019 materials by design roadmap". In: *Journal of Physics D: Applied Physics* 52 (Jan. 2019).

[31] Richard L Anderson. "Experiments on ge-gaas heterojunctions". In: *Electronic Structure of Semiconductor Heterojunctions*. Springer, 1988, pp. 35–48.

[32] Vidhya Chakrapani. "Semiconductor Junctions, Solid-Solid Junctions". In: pp. 1882–1893. ISBN: 978-1-4419-6995-8.

[33] Jianhua Zhao, Aihua Wang, Martin A Green, and Francesca Ferrazza. "19.8% efficient "honeycomb" textured multicrystalline and 24.4% monocrystalline silicon solar cells". In: *Applied Physics Letters* 73.14 (1998), pp. 1991–1993.

[34] ZA Weinberg, GW Rubloff, and E Bassous. "Transmission, photoconductivity, and the experimental band gap of thermally grown SiO2 films". In: *Physical Review B* 19.6 (1979), p. 3107.

[35] Mikio Taguchi, Akira Terakawa, Eiji Maruyama, and Makoto Tanaka. "Obtaining a higher Voc in HIT cells". In: *Progress in Photovoltaics: Research and Applications* 13.6 (2005), pp. 481–488.

[36] Yasufumi Tsunomura, Yukihiro Yoshimine, Mikio Taguchi, Toshiaki Baba, Toshihiro Kinoshita, Hiroshi Kanno, Hitoshi Sakata, Eiji Maruyama, and Makoto Tanaka. "Twenty-two percent efficiency HIT Solar Cell". In: *Solar Energy Materials and Solar Cells* 93 (2009), pp. 670–673.

[37] S Rauscher, Th Dittrich, M Aggour, J Rappich, H Flietner, and HJ Lewerenz. "Reduced interface state density after photocurrent oscillations and electrochemical hydrogenation of n-Si (111): A surface photovoltage investigation". In: *Applied physics letters* 66.22 (1995), pp. 3018–3020.

[38] Thomas Lauinger, Jan Schmidt, Armin G Aberle, and Rudolf Hezel. "Record low surface recombination velocities on 1 Ω cm p-silicon using remote plasma silicon nitride passivation". In: *Applied physics letters* 68.9 (1996), pp. 1232–1234.

[39] Bram Hoex, Jan Schmidt, P Pohl, MCM Van de Sanden, and WMM Kessels. "Silicon surface passivation by atomic layer deposited Al2O3". In: *Journal of Applied Physics* 104.4 (2008), p. 044903.

[40] J Schmidt, A Merkle, R Brendel, B Hoex, MCM van de Sanden, and WMM Kessels. "Surface passivation of high-efficiency silicon solar cells by atomic-layer-deposited Al2O3". In: *Progress in photovoltaics: research and applications* 16.6 (2008), pp. 461–466.

[41] Stefaan De Wolf, Antoine Descoeudres, Zachary C Holman, and Christophe Ballif. "High-efficiency silicon heterojunction solar cells: A review". In: *Green* 2.1 (2012), pp. 7–24.

[42] Stephan Lany, Jorge Osorio-Guillén, and Alex Zunger. "Origins of the Doping Asymmetry in Oxides: Hole Doping in NiO Versus Electron Doping in ZnO". In: *Physical Review B* 75 (2007).

[43] BT Raut, SG Pawar, MA Chougule, Shashwati Sen, and VB Patil. "New process for synthesis of nickel oxide thin films and their characterization". In: *Journal of Alloys and Compounds* 509.37 (2011), pp. 9065–9070.

[44] M Jlassi, I Sta, M Hajji, and H Ezzaouia. "Synthesis and characterization of nickel oxide thin films deposited on glass substrates using spray pyrolysis". In: *Applied Surface Science* 308 (2014), pp. 199–205.

[45] Muhammad Z Sialvi, Roger J Mortimer, Geoffrey D Wilcox, Asri Mat Teridi, Thomas S Varley, KG Upul Wijayantha, and Caroline A Kirk. "Electrochromic and colorimetric properties of nickel (II) oxide thin films prepared by aerosol-assisted chemical vapor deposition". In: *ACS Applied Materials & Interfaces* 5.12 (2013), pp. 5675–5682.

[46] Robert Karsthof, Arthur Markus Anton, Friedrich Kremer, and Marius Grundmann. "Nickel vacancy acceptor in nickel oxide: Doping beyond thermodynamic equilibrium". In: *Physical Review Materials* 4 (3 Mar. 2020), p. 034601.

[47] M Predanocy, I Hotový, and M Čaplovičová. "Structural, optical and electrical properties of sputtered NiO thin films for gas detection". In: *Applied Surface Science* 395 (2017), pp. 208–213.

[48] A Mallikarjuna Reddy, A Sivasankar Reddy, and P Sreedhara Reddy. "Thickness dependent properties of nickel oxide thin films deposited by dc reactive magnetron sputtering". In: *Vacuum* 85.10 (2011), pp. 949–954.

[49] Francesca Menchini, Maria Luisa Grilli, Theodoros Dikonimos, Alberto Mittiga, Luca Serenelli, Enrico Salza, Rosa Chierchia, and Mario Tucci. "Application of NiOx thin films as p-type emitter layer in heterojunction solar cells". In: *physica status solidi c* 13.10-12 (2016), pp. 1006–1010.

[50] R.C. Sahu, Tzu-Jung Wu, Sheng-Chang Wang, and Jow-Lay Huang. "Electrochromic behavior of NiO film prepared by e-beam evaporation". In: *Journal of Science: Advanced Materials and Devices* 2 (May 2017).

[51] Ramsés Gamboa, Oscar Jaramillo-Quintero, Yarimeth Alarcón Altamirano, Maria-Olga Concha-Guzman, and Marina Rincón. "A novel nanocomposite based on NiOx-incorporated P3HT as hole transport material for Sb2S3 solar cells with enhanced device performance". In: *Journal of Colloid and Interface Science* 535 (2019), pp. 400–407.

[52] Marko Jošt, Tobias Bertram, Dibyashree Koushik, Jose A Marquez, Marcel A Verheijen, Marc D Heinemann, Eike Köhnen, Amran Al-Ashouri, Steffen Braunger, Felix Lang, et al. "21.6%-Efficient monolithic perovskite/Cu (In, Ga) Se2 tandem solar cells with thin conformal hole transport layers for integration on rough bottom cell surfaces". In: *ACS Energy Letters* 4.2 (2019), pp. 583–590.

[53] Diego Di Girolamo, Nga Phung, Marko Jošt, Amran Al-Ashouri, Ganna Chistiakova, Junming Li, José A Márquez, Thomas Unold, Lars Korte, Steve Albrecht, et al. "From Bulk to Surface: Sodium Treatment Reduces Recombination at the Nickel Oxide/Perovskite Interface". In: *Advanced Materials Interfaces* 6.17 (2019), p. 1900789.

[54] Diego Di Girolamo, Fabio Matteocci, Felix Utama Kosasih, Ganna Chistiakova, Weiwei Zuo, Giorgio Divitini, Lars Korte, Caterina Ducati, Aldo Di Carlo, Danilo Dini, et al. "Stability and Dark Hysteresis Correlate in NiO-Based Perovskite Solar Cells". In: *Advanced Energy Materials* 9.31 (2019), p. 1901642.

[55] Steffen Braunger, Laura E Mundt, Christian M Wolff, Mathias Mews, Carolin Rehermann, Marko Jošt, Alvaro Tejada, David Eisenhauer, Christiane Becker, Jorge Andres Guerra, et al. "Cs x FA1–x Pb (I1–y Br y) 3 Perovskite Compositions: the Appearance of Wrinkled Morphology and its Impact on Solar Cell Performance". In: *The Journal of Physical Chemistry C* 122.30 (2018), pp. 17123–17135.

[56] Vikrant A Chaudhari and Chetan S Solanki. "A novel two step metallization of Ni/Cu for low concentrator c-Si solar cells". In: *Solar Energy Materials and Solar Cells* 94.12 (2010), pp. 2094–2101.

[57] Loic Tous, Jean-Francois Lerat, Thierry Emeraud, R Negru, K Huet, A Uruena, Monica Aleman, Richard Russell, Joachim John, Jef Poortmans, et al. "Nickel silicide formation using excimer laser annealing". In: *Energy Procedia* 27.503-509 (2012), p. 154.

[58] Loic Tous, Richard Russell, Jo Das, Riet Labie, Michel Ngamo, Jörg Horzel, Harold Philipsen, Jeroen Sniekers, K Vandermissen, Lukas van den Brekel, et al. "Large area copper plated silicon solar cell exceeding 19.5% efficiency". In: *Energy Procedia* 21 (2012), pp. 58–65.

[59] Sven Kluska, Jonas Bartsch, Andreas Büchler, Gisela Cimiotti, Andreas A Brand, Sybille Hopman, and Markus Glatthaar. "Electrical and mechanical properties of plated Ni/Cu contacts for Si solar cells". In: *Energy Procedia* 77 (2015), pp. 733–743.

[60] Jonas Bartsch, Mathias Kamp, Dominik Hartleb, Carolin Wittich, Andrew Mondon, Bernd Steinhauser, Frank Feldmann, Armin Richter, Jan Benick, Markus Glatthaar, et al. "21.8% efficient n-type solar cells with industrially feasible plated metallization". In: *Energy Procedia* 55 (2014), pp. 400–409.

[61] DS Kim, EJ Lee, J Kim, and SH Lee. "Low-cost contact formation of high-efficiency crystalline silicon solar cells by plating". In: *Journal of the Korean Physical Society* 46.5 (2005), pp. 1208–1212.

[62] Michael Rauer, Andrew Mondon, Christian Schmiga, Jonas Bartsch, Markus Glatthaar, and Stefan W Glunz. "Nickel-plated front contacts for front and rear emitter silicon solar cells". In: *Energy Procedia* 38 (2013), pp. 449–458.

[63] Tao Li, Wenjing Wang, Chunlan Zhou, Zhengang Liu, Lei Zhao, Hailing Li, and Hongwei Diao. "Influence of nickel silicide thin film on series resistance of silicon solar cells". In: *Current Nanoscience* 8.4 (2012), pp. 628–631.

[64] Alexander Marshall, Karine Florent, Astha Tapriya, Benjamin G Lee, Santosh K Kurinec, and David L Young. "Nickel silicide metallization for passivated tunneling contacts for silicon solar cells". In: *2016 IEEE 43rd Photovoltaic Specialists Conference (PVSC)*. IEEE. 2016, pp. 2479–2482.

[65] JO Olowolafe, M-A Nicolet, and JW Mayer. "Influence of the nature of the Si substrate on nickel silicide formed from thin Ni films". In: *Thin Solid Films* 38.2 (1976), pp. 143–150.

[66] Jeanette Lindroos, David P Fenning, Daniel J Backlund, Erik Verlage, Angelika Gorgulla, Stefan K Estreicher, Hele Savin, and Tonio Buonassisi. "Nickel: A very fast diffuser in silicon". In: *Journal of Applied Physics* 113.20 (2013), p. 204906.

[67] A Yu Kuznetsov and BG Svensson. "Nickel atomic diffusion in amorphous silicon". In: *Applied physics letters* 66.17 (1995), pp. 2229–2231.

[68] Adolf Fick. "Ueber diffusion". In: *Annalen der Physik* 170.1 (1855), pp. 59–86.

[69] MK Bakhadyrkhanov, S Zainabidinov, and A Khamidov. "Some characteristics of diffusion and electrotransport of nickel in silicon". In: *Soviet Physics Semiconductors* 14 (1980), p. 243.

[70] Yohan Yoon, Bijaya Paudyal, Jinwoo Kim, Young-Woo Ok, Prashant Kulshreshtha, Steve Johnston, and George Rozgonyi. "Effect of nickel contamination on high carrier lifetime n-type crystalline silicon". In: *Journal of Applied Physics* 111.3 (2012), p. 033702.

[71] Hele Savin, Marko Yli-Koski, Antti Haarahiltunen, Heli Talvitie, and Juha Sinkkonen. "Contactless diagnostic tools and metallic contamination in the semiconductor industry". In: *ECS Transactions* 11.3 (2007), p. 319.

[72] Arash Mahmoudzadeh. "Dual Ion Engine Design & Development". In: (Oct. 2015).

[73] Alberto Mazzi. "Modeling and production of metal nanoparticles through laser ablation and applications to photocatalytic water oxidation". PhD thesis. Mar. 2017.

[74] Aritra Ghosh, Senthilarasu Sundaram, and Tapas K Mallick. "Investigation of thermal and electrical performances of a combined semi-transparent PV-vacuum glazing". In: *Applied energy* 228 (2018), pp. 1591–1600.

[75] Brian D Viezbicke, Shane Patel, Benjamin E Davis, and Dunbar P Birnie III. "Evaluation of the Tauc method for optical absorption edge determination: ZnO thin films as a model system". In: *physica status solidi b* 252.8 (2015), pp. 1700–1710.

[76] Tim Kodalle, Dieter Greiner, Varvara Brackmann, Karsten Prietzel, Anja Scheu, Tobias Bertram, Pablo Reyes-Figueroa, Thomas Unold, Daniel Abou-Ras, Rutger Schlatmann, et al. "Glow discharge optical emission spectrometry for quantitative depth profiling of CIGS thin-films". In: *Journal of Analytical Atomic Spectrometry* 34.6 (2019), pp. 1233–1241.

[77] T Trupke, B Mitchell, JW Weber, W McMillan, RA Bardos, and R Kroeze. "Photoluminescence imaging for photovoltaic applications". In: *Energy Procedia* 15 (2012), pp. 135–146.

[78] John F Watts and John Wolstenholme. *An introduction to surface analysis by XPS and AES*. Wiley Online Library, 2003.

[79] Marcus Frederick Charles Ladd, Rex Alfred Palmer, and Rex Alfred Palmer. *Structure determination by X-ray crystallography*. Springer, 1985.

[80] Masaki Morita. "Scanning Electron Microscope Energy Dispersive X-Ray Spectrometry". In: *Compendium of Surface and Interface Analysis*. Springer, 2018, pp. 557–561.

[81] Kristijan Kuhlmann. "Development and Commissioning of a Prototype Neutron Backscattering Spectrometer with an Energy Resolution Enhanced by an Order of Magnitude using GaAs Single Crystals". PhD thesis. Jan. 2018.

[82] Anwar Ul-Hamid, Abdul Quddus, Huseyin Saricimen, and Hatim Dafalla. "Corrosion Behavior of Coarse-and Fine-Grain Ni Coatings Incorporating NaH2PO4. H2O Inhibitor Treated Substrates". In: *Materials Research* 18.1 (2015), pp. 20–26.

[83] Ronald A Sinton and Andres Cuevas. "Contactless determination of current–voltage characteristics and minority-carrier lifetimes in semiconductors from quasi-steady-state photoconductance data". In: *Applied Physics Letters* 69.17 (1996), pp. 2510–2512.

[84] R. Einhaus, J. Kraiem, J. Degoulange, O. Nichiporuk, M. Forster, P. Papet, Y. Andrault, D. Grosset-Bourbange, and F. Cocco. "19% efficiency heterojunction solar cells on Cz wafers from non-blended Upgraded Metallurgical Silicon". In: *2012 38th IEEE Photovoltaic Specialists Conference*. 2012, pp. 003234–003237.

[85] Damian Pysch, Ansgar Mette, and Stefan W Glunz. "A review and comparison of different methods to determine the series resistance of solar cells". In: *Solar Energy Materials and Solar Cells* 91.18 (2007), pp. 1698–1706.

[86] Marko Marinkovic. "Contact resistance effects in thin film solar cells and thin film transistors". PhD thesis. Jacobs University Bremen, 2013.

[87] Edward Ramsden. *Hall-effect sensors: theory and application*. Elsevier, 2011.

[88] Deepa S. Narang. "Thermoelectric power of tungsten diselenide grown by a direct vapour transport technique". In: *'Prajna' - Journal of Pure & Applied Sciences* (Jan. 2008).

[89] L. J. van der Pauw. "A method of measuring specific resistivity and Hall effect of discs of arbitrary shape". In: *Philips Research Reports* 13.1 (1958), pp. 1–9.

[90] Gerald Abowitz and Emil Arnold. "Simple Mercury Drop Electrode for MOS Measurements". In: *Review of Scientific Instruments* 38.4 (1967), pp. 564–565.

[91] AB Morales-Vilches, L Mazzarella, M Hendrichs, L Korte, R Schlatmann, and B Stannowski. "Nanocrystalline vs. amorphous n-type silicon front surface field layers in silicon heterojunction solar cells: Role of thickness and oxygen content". In: *33rd European Photovoltaic Solar Energy Conference and Exhibition*. 2017, pp. 715–719.

[92] A. N. Mansour. "Characterization of NiO by XPS". In: *Surface Science Spectra* 3.3 (1994), pp. 231–238.

[93] Klaus Ellmer. "Magnetron sputtering of transparent conductive zinc oxide: relation between the sputtering parameters and the electronic properties". In: *Journal of Physics D: Applied Physics* 33.4 (2000).

[94] Klaus Ellmer and Rainald Mientus. "Carrier transport in polycrystalline ITO and ZnO: Al II: The influence of grain barriers and boundaries". In: *Thin Solid Films* 516.17 (2008), pp. 5829–5835.

[95] John YW Seto. "The electrical properties of polycrystalline silicon films". In: *Journal of Applied Physics* 46.12 (1975), pp. 5247–5254.

[96] G Burns. *Solid State Physics Sections 18-5 and 18-6*. 1985.

[97] Shengwen Luan and Gerold W Neudeck. "An experimental study of the source/drain parasitic resistance effects in amorphous silicon thin film transistors". In: *Journal of Applied Physics* 72.2 (1992), pp. 766–772.

[98] Er-Chien Wang, Anna B. Morales-Vilches, Sebastian Neubert, Alexandros Cruz, Rutger Schlatmann, and Bernd Stannowski. "A simple method with analytical model to extract heterojunction solar cell series resistance components and to extract the A-Si:H(i/p) to transparent conductive oxide contact resistivity". In: *SiliconPV 2019, the 9th International Conference on Crystalline Silicon Photovoltaics*. Vol. 2147. American Institute of Physics Conference Series. Aug. 2019, p. 040022.

[99] Qirong Liu, Qianqian Chen, Qianqian Zhang, Guobo Dong, Xiaolan Zhong, Yu Xiao, Marie-Paule Delplancke-Ogletree, François Reniers, and Xungang Diao. "Dynamic behaviors of inorganic all-solid-state electrochromic device: Role of potential". In: *Electrochimica Acta* 269 (2018), pp. 617–623.

[100] Michael D Irwin, D Bruce Buchholz, Alexander W Hains, Robert PH Chang, and Tobin J Marks. "p-Type semiconducting nickel oxide as an efficiency-enhancing anode

interfacial layer in polymer bulk-heterojunction solar cells". In: *Proceedings of the National Academy of Sciences* 105.8 (2008), pp. 2783–2787.

[101] I Hotový, J Huran, J Janik, and AP Kobzev. "Deposition and properties of nickel oxide films produced by DC reactive magnetron sputtering". In: *Vacuum* 51.2 (1998), pp. 157–160.

[102] Yong Hwan Lee, Hee-eun Song, Ka-Hyun Kim, and Jihun Oh. "Investigation of surface reactions in metal oxide on Si for efficient heterojunction Si solar cells". In: *APL Materials* 7.7 (2019), p. 071106.

[103] I Porqueras and E Bertran. "Electrochromic behaviour of nickel oxide thin films deposited by thermal evaporation". In: *Thin Solid Films* 398 (2001), pp. 41–44.

[104] B Sasi, KG Gopchandran, PK Manoj, P Koshy, P Prabhakara Rao, and VK Vaidyan. "Preparation of transparent and semiconducting NiO films". In: *Vacuum* 68.2 (2002), pp. 149–154.

[105] PJ Grunthaner, FJ Grunthaner, and JW Mayer. "XPS study of the chemical structure of the nickel/silicon interface". In: *Journal of Vacuum Science and Technology* 17.5 (1980), pp. 924–929.

[106] P.L. Tam and Lars Nyborg. "Sputter deposition and XPS analysis of nickel silicide thin films". In: *Surface and Coatings Technology* 203.19 (2009), pp. 2886–2890.

[107] Anna Belen Morales, Alexandros Cruz, Sebastian Pingel, Sebastian Neubert, Luana Mazzarella, Daniel Meza, Lars Korte, Rutger Schlatmann, and Bernd Stannowski. "ITO-Free Silicon Heterojunction Solar Cells With ZnO:Al/SiO2 Front Electrodes Reaching a Conversion Efficiency of 23%". In: *IEEE Journal of Photovoltaics* (Oct. 2018), pp. 1–6.

## List of Publications

[4] Daniel Meza, Alexandros Cruz, Anna Belen Morales, Lars Korte, and Bernd Stannowski. "Aluminum-Doped Zinc Oxide as Front Electrode for Rear Emitter Silicon Heterojunction Solar Cells with High Efficiency". In: *Applied Sciences* 9 (2019), p. 862.

[19] Alexandros Cruz, Er-Chien Wang, Anna B Morales-Vilches, Daniel Meza, Sebastian Neubert, Bernd Szyszka, Rutger Schlatmann, and Bernd Stannowski. "Effect of front TCO on the performance of rear-junction silicon heterojunction solar cells: Insights

from simulations and experiments". In: *Solar Energy Materials and Solar Cells* 195 (2019), pp. 339–345.

[107] Anna Belen Morales, Alexandros Cruz, Sebastian Pingel, Sebastian Neubert, Luana Mazzarella, Daniel Meza, Lars Korte, Rutger Schlatmann, and Bernd Stannowski. "ITO-Free Silicon Heterojunction Solar Cells With ZnO:Al/SiO2 Front Electrodes Reaching a Conversion Efficiency of 23%". In: *IEEE Journal of Photovoltaics* (Oct. 2018), pp. 1–6.

# Acknowledgements

I would like to thank Prof. Dr. Bernd Rech for his support during this years, guiding my scientific work and being my Doktorvater. I learned from your advice, not only scientifically but also in my personal development.

Also thanks to my main advisors Prof. Dr. Bernd Stannowski and Dr. Lars Korte for the supervision during all this years, the experiment planning, the analysis of the results and the fruitful discussions that helped me completing this thesis. I guess it was not easy to work with me, but hey, a challenge once in a while makes life interesting.

Thanks to Prof. Dr. Arno Smets for accepting to evaluate this thesis and being a part of the PhD committee.

Thanks to Dr. Kirner, Dr. Mazzarella, Dr. Vilches-Morales, Dr. Hendrichs and Holger Rhein for the HF dips, AKT depositions and screen printing for the first part of this work and also for being a great team during my time in PVcomB. Also thanks to Dr. Neubert for the help with the AZO experiment planning, to Karolina Mack and Tobias Hänel for the help with analytics at PVcomB, and to Sophie Kolb for the help with the EQE measurements.

I am thankful to Katja Mayer-Stillrich and Manuel Hartig for the help with the depositions in the LOS1 and for valuable advice about sputtering, I learned a lot from our talks, and enjoyed every day working with you. Also thanks to Dr. Cruz for the teamwork on the LOS1.

Special thanks to Beatrice Bujok and Dr. Matthias Zellmeier for introducing me to the world of e-beam deposition and teaching me the analog magic of the UNIVEX450, Thomas Lußky for helping me bring it back to life and installing the oxygen source for my depositions. UNIVEX450, thanks for being an awesome machine and joining me in this journey, it was your last adventure but you will continue to live in my memory.

Many thanks to Carola Klimm for helping me with SEM micrographs and EDX images but also for sharing your knowledge about these techniques with me. To Kerstin Jacob and Mona Wittig for providing me with silicon wafers and to Philipp Wagner for PECVD depositions.

Thanks to Katherine Mazzio, Carolin Rehermann and Marcel Roß for XRD measurements and Tim Kodalle for GDOES measurements, your help was greatly appreciated.

Thanks to Dr. Engin Özkol for the depositions in the EMIL cluster, the support in the last phase of my PhD and, together with Dr. Cruz, Dr. Erfurt, Dr. Chistiakova and Frau Menzel for reading my thesis and giving me helpful feedback about it. To Kati Hirselandt and Jakob Bombsch for help with the corrections i received, thanks!

Dr. Bjorn Rau and Matthias Zelt, for the nice introduction to PVcomB when i firstly arrived, and to Annett Gerch for helping me with all the administrative stuff always with a smile on her face. Also thanks to Andreas von Kozierowski for taking his time to explain me how HZB works.

Thanks to Dr. Thomas Dittrich, for being a mentor since 2011 when I first attended his lecture at the TU Berlin, for giving me the opportunity of being the lab tutor in the following years and for giving me moral support through the years. You are a great person.

I'm also thankful to Prof. Dr. Rolf Hanitsch, for the advice he has given me through the years, the trust to let me help with his PV course, and for reading the thesis and giving me feedback about it many times.

Many thanks to Dr. Gabi Lampert for helping me with problems of many kinds, your support was one of the most important things for finishing my PhD. I will always be thankful to you, and will remember the work we did together for the PhD community as one of the greatest things that ever happened to me.

I'm thankful to Antonia Rötger for the many interesting discussions about science and for helping me understand the importance of science communication to present our work to society. Your advice motivated me to keep communicating science and becoming better at it.

Thanks to Marion Krusche for all the support during my PhD, for taking care of me and for the help with all the administrative stuff. To know that you were only a couple meters away gave me always a sense of safety. The EE-IS is lucky to have you.

Thanks to Dr. Julia Wienold for helping me with the process of registering a patent, it was nice to have someone that believed in this idea and motivated me to bring it to the end.

HZB BMX Crew, you were the highlight of my time as a PhD, getting to know all of you was a great experience. Some people say I gave a lot to the PhD community but I think it was the other way around, to see you happy, having fun and building friendships was the fuel that kept me going. I hope we can be friends for life. Thanks!

Special thanks to the other PhD representatives and the PhD retreats organizers, to Stefan Körner for being the retreat logistics master and to Dr. Tim Frijnts for proposing me as a representative in 2016, it was a hell of a ride!

Thanks to the HeJus and to the colleagues of the $N^2$ association, with whom I shared some great moments during these years, you are all great people and we achieved great things together. I hope to see you again many times during my life.

Many thanks to the science slam community, specially to Dr. Julia Offe, Simon Hauser, Dr. Andrè Lampe, Sveda Gettys and the WISTA and Policult people for giving me the opportunity of presenting my research work to society, and also to all the slammers I had the chance to share a stage with. I'm also thankful to all the people that go to a science slam to listen to us, your interest in science is invaluable and a big motivation for us.

To my dear friends Zarte, Nur, Meli, Mare, Lydi, Marianita, Basti, Ivona, Majvor and los Mostros thanks for being there during these years.

Infinite thanks to Frau Menzel and Abdiel Ramírez Torres for your help during the final phase of this thesis, but even more for your friendship during all these years. You are two of the best friends anyone could have and I am very happy to know I can count on you.

My dear Meike Kühnel, thanks for all the fun and joy but also for the support during the hardest times. You are awesome and it is nice to have someone with whom I can be as foolish as i want, all day long, day after day after day.

Thanks to my family in México that have supported me all these years, it has been hard to be far away for so long but you are always in my heart.

Special thanks to my brother Raúl that has always taken care of me since i was a little kid and to my loving parents Verónica and Raúl, who always supported me in any project I undertook and let me grow in every dimension of life. Your love taught me to always work to make this world a better place and the trust you gave me every day, gave wings to my dreams.

# Eidesstattliche Erklärung

Hiermit erkläre ich, Daniel Meza Arredondo, dass ich die vorliegende Arbeit mit dem Titel: “Development of indium-free thin films as contacts for silicon heterojunction solar cells” selbstständig und ohne fremde Hilfe verfasst und dabei keine anderen als die angegebene Quellen und Hilfsmittel benutzt habe. Alle wörtlich oder inhaltlich übernommenen Textstellen anderer Werke sowie die Beiträge Dritter habe ich als solche kenntlich gemacht.

Des Weiteren erkläre ich weder bereits vergebliche Promotionsversuche unternommen zu haben, noch die vorliegende oder eine andere Arbeit als Dissertation bei einer anderen Fakultät eingereicht zu haben.

Ich bin weder vorbestraft, noch wurde ein Ermittlungsverfahren gegen mich eingeleitet.

Berlin, den 10.4.2021 _____